THE UNIVERSITY OF TEXAS AT ARLINGTON

THE COMMISSIONING OF THE LOW FREQUENCY ALL SKY MONITOR, THE FIRST DISTRIBUTED PHASED ARRAY TELESCOPE SPECIFICALLY DESIGNED TO SEARCH FOR RADIO TRANSIENTS AT LONG WAVELENGTHS

A DISSERTATION SUBMITTED TO
THE FACULTY OF THE GRADUATE SCHOOL OF
THE UNIVERSITY OF TEXAS AT ARLINGTON
IN PARTIAL FULFILLMENT OF
THE REQUIREMENTS FOR THE DEGREE OF

DOCTOR OF PHILOSOPHY

BY
LOUIS PERCY DARTEZ

MAY 2021

In memory of my father

Louis Dartez, Jr.

and to my parents

Luz & Aureliano

and to my fiancée

Mayra

TABLE OF CONTENTS

LIST OF FIGURES

LIST OF TABLES

ACKNOWLEDGMENTS

Special thanks to the following people: Mayra Delgado for your patience and unwavering support; Dr. Teviet Creighton for advising, encouraging, and challenging me over the years; Dr. Fredrick A. Jenet for the design of and initial encouragement to work on LoFASM, which has led to me falling in love with technology development as a whole, and for the creation of several research and educational programs that I've had the fortune to participate in; Dr. Volker Quetschke for the invaluable advice and our many water cooler chats; My committee members at UT Arlington, Dr. Ramon Lopez, Dr. Manfred Cuntz, and Dr. Zdzislaw Musielak, for the opportunities afforded to me by the cooperative PhD program; Alma Miller for all the support, encouragement, and guidance; Maria Degwitz for keeping CARA running and always being there when I needed help; Brent Cole for all your work to maintain and improve LoFASM and pushing through our many challenging endeavors together; Dr. Jing Luo for the much needed discussions about life and the pursuit of pulsars, you're an inspiration; Paulina Varela for your help in implementing portions of the LoFASM data analysis; Dr. Murat Torlak and Dr. Tim Dolch for insightful discussions about using LoFASM as an instrument and how to improve it; the staff at Green Bank Observatory, namely Marty Bloss & Jason Ray, for being a pleasure to work with and always being willing to help with a LoFASM-related task; The staff at Goldstone, Jeffrey Lagrange & Paul Dendrenos, for all of your help with LoFASM IV and always happy to go an extra mile to lend a helping hand; Dr. Joe Lazio, Dr. Namir Kassim, & Dr. Greg Taylor for the large scope conversations about the field of radio astronomy and its future; the rest of the LoFASM team over the years, none of this work could have happened without your help.

Work on LoFASM was initially supported by DoD contract #W911NF-12-1-0062 and has subsequently been supported by NSF grants AST 0545837, AST 0750913, & AST 1547452.

ABSTRACT

The Commissioning of the Low Frequency All Sky Monitor, the First Distributed Phased Array Telescope Specifically Designed to Search for Radio Transients at Long Wavelengths

Louis P. Dartez

The University of Texas at Arlington, 2021

Supervising Professor: Dr. Teviet Creighton

The last two decades have seen a proliferation in the development of technology for low frequency radio astronomy based upon phased elements grouped into one or more large stations. Instruments fielding multiple large stations containing anywhere from dozens to hundreds of long wavelength dipole antenna elements include the Long Wavelength Array, the Low Frequency Array, and the Murchison Widefield Array. All of these instruments include the detection of radio transients within their broad scientific portfolios. I cover the early commissioning of the Low Frequency All Monitor (LoFASM), a phased array instrument, conceived and designed by Dr. Fredrick A. Jenet, similarly comprised of multiple stations but focused more narrowly on the all-sky detection of bright radio transients at low frequencies. LoFASM stations are considerably smaller, operated independently, and currently distributed across the continental United States. While there are many theoretical predictions for low frequency extra-solar coherent sources, with the exceptions of radio pulsars, this frequency range remains a relatively unexplored frontier. LoFASM stations search the skies for radio transients in the 15-88 MHz frequency range, favoring the detection of coherent emission processes. This thesis describes the design of the LoFASM system together with results from early tests to demonstrate its operational capabilities, including a review of data taken of solar transients, potential ionospheric activity, the Galactic background, as well as Galactic and extra-galactic point sources.

CHAPTER 1

INTRODUCTION

1.1 Background

Radio astronomy is a field within astronomy and astrophysics that focuses on studying celestial phenomena throughout the universe by analyzing extraterrestrial emissions detected in the radio spectrum (30 Hz - 300 GHz). Energy in the form of radio waves of extraterrestrial origins were first detected by Karl G. Jansky near the 20 MHz band in the 1930's while working at Bell Telephone Laboratories. (Jansky [1933]) Karl Jansky was tasked with tracking down and identifying various forms of radio interference that were plaguing telephone communications at the time. The radio interference was negatively impacting the quality of calls made using the AT&T Bell Telephone System and as a result there was interest in investigating the spectral nature of any nearby sources of radio noise that might be contributing to the degradation of the company's communication signals and identifying a frequency free of interfering signals. Using a linear, directional antenna array that he built, Jansky was able to determine the origins of almost all of the sources of interference, most of which were found to be either local in origin from passing automobiles, airplanes and nearby thunderstorms, or transmissions from radio stations in England and South America.

There was one source of static, however, that Jansky was unable to immediately track down. He noticed that the strength of the static would be strongest in different directions throughout the day: towards the east in the morning, south around noon, and to the west in the evening. Naturally, this lead Jansky to conclude that the noise had something to do with the Sun. Over months of study, Jansky noticed that the noise would arrive a few minutes earlier every day, and eventually noted that the source must be well removed from the Sun.

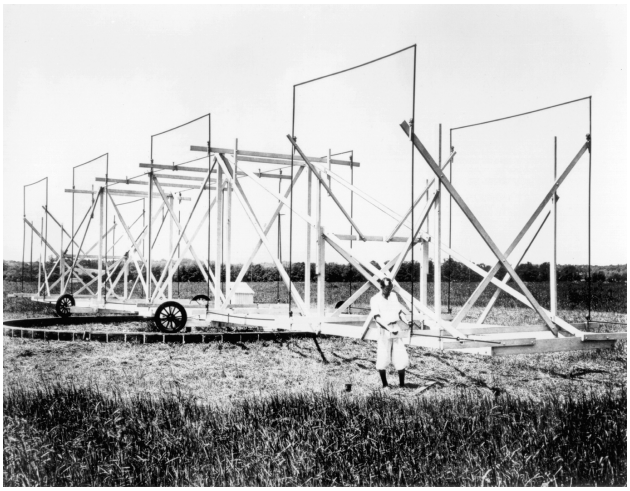

Figure 1.1: Karl Jansky with his rotating Bruce Array, aptly named the "merry-go-round", which he built for his work at Bell Telephone Labs and used to detect radio emissions from the Milky Way Galaxy. Credit: NRAO/AUI/NSF

Upon realizing that the unidentified radio interference would appear at the same sidereal time each day, he concluded that the signal he was seeing was extraterrestrial in origin and, with the help of Harlow Shapley, Director of the Harvard College Observatory, found that the source appeared to be in or near the center of mass of the Milky Way Galaxy. (Kellermann et al. [2020]) Without even knowing it Karl Jansky, known colloquially among radio astronomers as the father of radio astronomy, had used his aptly named "merry-go-round" array to serendipitously open a new window into the universe.

A few years later Grote Reber, a radio engineer inspired by Karl Jansky's work, built a single dish radio telescope in his back yard in 1937 to follow up on the discovery of radio waves from the Milky Way. For several years Reber's telescope was the only one in operation in the world until after World War II. After multiple failed attempts at higher frequencies, Reber successfully detected radio emissions from the Milky Way at 160 MHz in 1938. Reber conducted the first surveys of radio waves from the sky, in which he confirmed that the brightest part is toward the center of the Milky Way galaxy and mapped out other bright sources, such as those in Cygnus and Cassiopeia, for the first time. (Reber [1944])

Figure 1.2: Grote Reber's telescope, built in Reber's backyard in Wheaton, IL. Reber donated his telescope to the National Radio Astronomy Observatory in Green Bank, West Virginia, where he personally supervised its assembly in the early 1960's. The telescope remains there as a historical monument. Credit: Green Bank Observatory

In the years leading up to World War II, various countries began to use what little was known about radio technology to develop active radar systems capable of detecting aircraft at large distances. Sir Robert Watson-Watt, credited with the invention of radar, oversaw the development of the "Chain Home" (CH) radar-based early warning detection system in Britain. Implemented as a curtain array of dipoles and operational just in time for the Battle of Britain in 1940, the CH radar could detect enemy aircraft at from several hundred miles away. (Hanbury Brown [1991]) In the United States, the development of the first electronically steerable phased arrays was underway, primarily for transatlantic

communication purposes. (Friis and Feldman [1937])

After World War II and in the roughly 90 years since, scientists from all over the world have taken the early work of Jansky and Reber and rapidly expanded upon it. But instead of continuing to study the cosmos at very low frequencies via large arrays of dipole antennas operating at 2 MHz, as Reber certainly would have liked (Kraus [1988], Garrett [2012]), researchers shifted to shorter wavelengths in order to avoid issues due to the ionosphere, increase angular resolution, and exploit the fact that sky background noise due to the Galaxy is reduced at higher frequencies.

Despite playing a major role in the early stages of radio astronomy, aperture arrays effectively disappeared as a popular radio telescope type. The majority of radio telescopes built since the 1960's sported large single (usually filled aperture) parabolic dish systems. Single dish systems were easier to operate, cheaper to maintain, and more reliable than aperture arrays consisting of hundreds of dipole antennas interconnected by several miles of wiring. With just a single receiver mounted on a parabolic reflector, single dish telescopes offered the option of a higher duty cycle and a lower cost. Additionally, recording voltage signals from each of hundreds of individual antenna elements was not feasible with the technology available at the time; many telescopes used paper chart plotters to record intensity over time (see Figure 1.3).

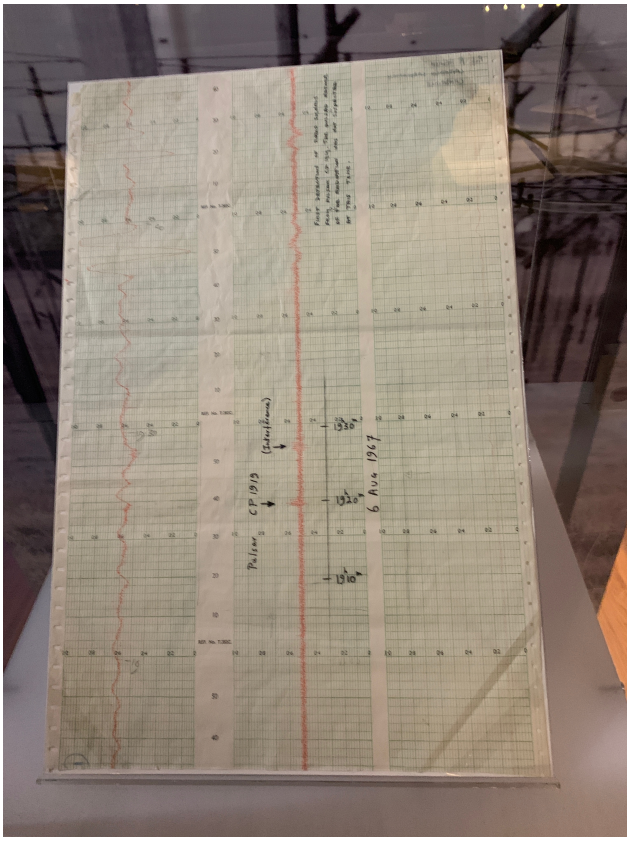

Figure 1.3: The chart examined by Jocelyn Bell Burnell in August 1967 with data from the 4 Acre Array radio telescope, showing the trace of the first identified radio pulsar, subsequently designated PSR B1919+21. Credit: Wikipedia contributors [2021]

Figure 1.4: At the time of this writing the largest filled-aperture single dish radio telescope in the world is the Five-hundred-meter Aperture Spherical radio Telescope (FAST) in China. Credit: AbsoluteCosmos [2020]

For many years researchers sought primarily to build and use single dish telescopes with as large a collecting area as possible combined with receivers operating at shorter wavelengths in the race for higher angular resolution. Recent technological advancements in digital electronics, general purpose and high performance computing, large capacity data storage systems, and signal processing lowered the barrier to entry for the resurgence of radio telescopes consisting of many antenna elements. Whether using an aperture array comprised of several antenna elements or a single dish telescope, the chase for higher angular resolution is paramount if studying discrete sources on the sky. The relationship determining the angular resolution of an interferometric array is analogous to that of its single dish counterpart such that

$$\theta \propto \frac{\lambda}{D} \propto \frac{\lambda}{B}, \tag{1.1}$$

where θ is the angular resolution in radians, λ is the operating wavelength, D is the effective

diameter of the single dish aperture, and the interferometer baseline, B, is the distance separating the elements. As such, instead of building a bigger dish researchers needed to build arrays with longer baselines to achieve superior angular resolutions. Furthermore, making use of more antenna elements within the area spanning the farthest antennas, effectively *filling* the aperture, resulted in better sky coverage and, in cases in which the additional elements were placed along various baselines of different directions, finer source resolution.

1.2 Motivation

Interest in radio astronomy at low frequencies returned as it became feasible to actively mitigate limitations imposed by the ionosphere using self-calibration methods with modern computers and sustain higher levels of background noise with radio frequency (RF) electronics capable of supporting high dynamic range signals. This helped stimulate a resurgence of efforts in high angular resolution imaging at both the Very Large Array (VLA) and Giant Metrewave Radio Telescope (GMRT). Momentum grew even further with the prediction that the detection of redshifted hydrogen beyond $z = 6$ (or $\leq 160\,\mathrm{MHz}$) could address key questions in cosmology from the Epoch of Reionization and the Dark Ages (Zaroubi [2012]). This energized the development of larger aperture array systems consisting of hundreds to thousands of active dipole antenna elements. The largest of these is the LOw Frequency ARray (LOFAR), a European telescope built in the Netherlands with two observational bands: a low band and a high band operating in the frequency ranges of $30 - 85\,\mathrm{MHz}$ and $115 - 230\,\mathrm{MHz}$, respectively. Other large aperture arrays include the Murchison Widefield Array (MWA) in Australia, and the Long Wavelength Array (LWA) in the United States, which currently has two stations located outside of Socorro, New Mexico (LWA-1) and at the Owens Valley Radio Observatory in Owens Valley (OVRO). All of these radio instruments have pursued two distinct scientific themes. One can be broadly categorized within traditional astrophysics, including the study of all discrete sources of emission benefiting

from high angular resolution imaging. The second is the search for the redshifted hydrogen line at 21 cm (HI) usually pursued in the spectral domain, though discrete source imaging can be brought to bear for foreground removal. The Precision Array for Probing the Epoch of Reionization (PAPER), which is being folded into the Hydrogen Epoch of Reionization Array (HERA) program, is an example of a low frequency, non-imaging aperture array whose entire focus was on the detection of redshifted HI (Parsons et al. [2010]).

A last distinct goal being pursued by almost all modern low frequency arrays are time domain studies, which include radio pulsars and radio transients. Since these targets can be pursued without imaging, they circumvent many of the most severe challenges at low frequencies associated with wide-field imaging and the demand for short-lived and angle-variant ionospheric calibration. Moreover, since the domain of radio transients is relatively under-explored at all radio wavelengths, it means there is fertile discovery space for smaller instruments, albeit at limited sensitivity. If one further imposes a constraint on expense, low frequencies are an attractive niche since the bandwidths are naturally smaller and expensive cryogenic receivers are inconsequential in a front-end noise dominated regime. Therein lies the motivation for the Low Frequency All Sky Monitor (LoFASM): a widely distributed aperture array telescope, initially conceived and designed by Dr. Fredrick A. Jenet, whose individual stations consist of only a handful of inexpensive active dipole antennas (Jenet et al. [2013]). Each station observes the entire sky continuously with anti-coincidence comparisons across stations mitigating the immense challenge of false positives from terrestrial radio frequency interference (RFI). A final driver for LoFASM is that small stations of reconfigurable elements offer an ideal testbed for training students, both in the field and in the laboratory. I should know; I am one of them.

1.3 Objective

Throughout my tenure working on the LoFASM, I have been instrumental to its design, installation, deployment, testing, troubleshooting, testing again, and operation. I've also been fortunate to help lead a variety of students through the endeavor of commissioning and calibrating the various LoFASM stations. While the individual LoFASM stations are scattered throughout the North American continent, they are all remotely operated by me typing furiously away on my laptop in Brownsville, Texas. By designing, deploying, and commissioning the LoFASM stations I and everyone who has comprised the LoFASM team at the University of Texas Rio Grande Valley, Hillsdale College, and the University of Texas at Dallas have learned much about radio astronomy, radio RF technology development, signal analysis, radio imaging, and electronics design.

There are only a handful of low frequency ($<$100 MHz) phased array systems out there. None of them are dedicated to monitoring as much of the sky as possible for a significant portion of their duty cycle. Instead, most comparable instruments were designed amidst the great quest for angular resolution in order to be able to finely resolve discrete points on the sky to be studied either spectrally or temporally. As a result, efforts to detect radio transients at low frequencies have been met with nothing but fraught silence. Large low frequency arrays with hundreds of elements spanning massive baselines are great for obtaining high angular resolution, but they do so at great cost. Performing interferometry using many ($>$200) elements necessitates the explicit use of real time beamforming algorithms due to the vast amounts of data being generated. This allows telescopes to record high fidelity data for specific points on the sky, *while throwing the rest away.* The data produced by hundreds of *dual polarization* cross-dipole antenna elements operating in wide bandwidths is simply too much to store, even by today's standards.

Pressure from the renewed focus on observations of transient phenomena such as Fast Radio Bursts(FRBs), where the origins and underlying physical mechanisms continue to

be an active area of research, underscores the importance of an instrument dedicated to scanning the full sky for as long as possible *and recording* the resulting data. While radio transients have been detected by single dish telescopes such as Parkes and Arecibo (R.I.P.), they have all been events that were recorded serendipitously and found after exhausted searches of archival data (Spitler et al. [2014], Lorimer et al. [2007]). A telescope with a wide field of view that is able to search for transient events in real time for followup observations could prove instrumental to the chase for an understanding of the physical mechanisms responsible for these phenomena by expeditiously providing higher resolution instruments with roughly localized alerts to trigger followup observations. One example showcasing the potential success of a wide-field all sky monitor at low frequencies is the Canadian Hydrogen Intensity Mapping Experiment (CHIME), a Canadian radio telescope operating across the 400-800 MHz band (Amiri et al. [2018]). CHIME has turned out to be a superior instrument for observing FRBs, due to their real time FRB search and detection capabilities and wide field of view (>200 square degrees) (Fonseca et al. [2020]).

LoFASM represents an effort to fill a gap in this all too unexplored regime of low frequency radio astronomy: the existence of an instrument with a wide bandwidth and large field of view that is capable of real-time transient detection and continuous recording of long term data storage to facilitate offline analyses of data at large timescales. Similar observing modes have been tested with larger arrays such as the LWA. However, they have been conducted only in very narrow bands ($\sim 100\,\mathrm{kHz}$) and at fairly long timescales ($\sim 50\,\mathrm{ms}$), thus a large portion ($\sim 99.8\%$) of the $15 - 88\,\mathrm{MHz}$ band is left unexplored and events on timescales $< 50\,\mathrm{ms}$ are obscured (Kent et al. [2019]). Fully realized, LoFASM aims to be capable of monitoring the majority of the $15 - 88\,\mathrm{MHz}$ band for short time scale transient activity, with an emphasis on the ever RFI polluted 20 MHz region. The LoFASM station architecture, designed with simplicity and cost effectiveness in mind, consists of 12 active LWA style antennas packed into a double ring configuration that, when combined in software, provides

a large synthesized beam on the sky that points straight up towards zenith. Recorded data rates are kept manageable by the relatively small number of antenna elements in each station and by combining element RF signals in phase in analog (see Section 2.1).

1.4 Chapter Overview

This thesis introduces LoFASM, still in its infancy, as a promising instrument soon to join the quest for the detection of transient activity in the sub-100 MHz regime. Throughout the execution of this work, the LoFASM stations, having just been physically installed, have undergone various rounds of testing, hardware and software upgrades, system overhauls, the addition of additional antenna elements for interferometry, and early commissioning data runs.

My work within the LoFASM team has been primarily to design the inaugural digital backend recording system and lead the collection of initial commissioning data using the same system. The original LoFASM data recording system, a full Stokes 100 MHz spectrometer, was the subject of my Master's thesis. Since then, we have designed and deployed upgrades to the backend, evolved the way in which we store archival data, designed a baseband recorder to allow for real time phase coherent data processing, and developed software from the ground up to facilitate the processing of initial data products. Additionally, since LoFASM, which is operated remotely, is an instrument that is primarily run by students (under the close supervision of faculty) and has dedicated engineers on staff, I have taken a leading role in the execution of many tasks that most radio astronomers, as users of well established observatories more resources, are able to avoid; this includes troubleshooting electronics, exploring calibration methods, and redesigning and implementing analog system overhauls, to name a few.

The design and deployment of the LoFASM arrays is presented in Chapter 2. This discussion includes a significant amount of work, most of which represents a Herculean effort by

the entire LoFASM team, which comprises students and faculty at the University of Texas Rio Grade Valley, the University of Texas at Dallas, and Hillsdale College. Results from these early data taking runs are described in Chapter 3. Chapter 4 discusses telescope operations and provides configuration parameters pertaining to the individual LoFASM stations. Potential avenues of future investigation are presented in Chapter 5, followed by a summary and some conclusive remarks in Chapter 6.

CHAPTER 2

THE LOW FREQUENCY ALL SKY MONITOR

The Low Frequency All Sky Monitor (LoFASM) is a distributed network of low frequency phased arrays comprising five stations installed across the continental United States. Each LoFASM station is a phased array of dipole antennas that are sensitive to incident energy in the 10-88 MHz radio frequency range. The restriction preventing observations of extraterrestrial radio waves below 10 MHz is imposed by ionosphere, which becomes opaque to radio frequencies somewhere between 10-20 MHz. This cutoff has had great consequences to the field of radio astronomy, namely for Epoch of Reionization studies, and is in large part responsible for the lack of exploration of the radio sky in the sub-100 MHz regime. The effects of the ionospheric opaqueness are so great that it has served as a key driver for the development of instruments to be deployed in areas where there is no ionosphere: namely in orbit around Earth or on the lunar surface (Carilli et al. [2007], de Gasperin et al. [2018], Cecconi [2019]). On the other hand, the upper limit imposed on LoFASM's spectral range is not natural in origin. The presence of terrestrial RFI generated by radio stations broadcasting in the FM frequency band (88-108 MHz) essentially renders that part of the spectrum unusable for the purposes of ground-based radio telescopes.

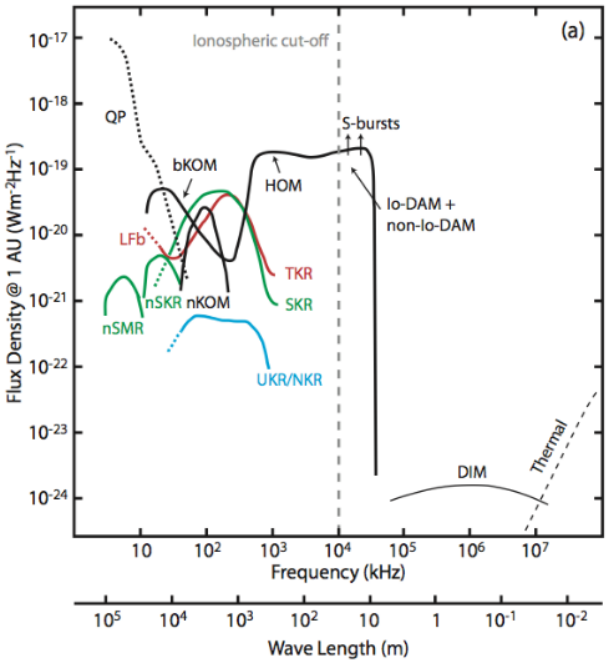

Figure 2.1: A comparison of planetary radio emission spectral flux densities showing the location of the ionospheric cutoff on the spectrum. Credit: Cecconi [2019], originally adapted from Zarka [2007]

RFI bleeding into spectral regions of interest present a significant hindrance to the study of naturally occurring radio transient events. It is well known that that terrestrial RFI can manifest in many forms, often mimicking radio signals of natural origin closely enough to make the task of excision infeasible. Unfortunately, unwanted anthropogenic RFI signals, are not always generated locally or within a direct line-of-sight (LoS) to the telescope. Low frequency telescopes often receive long-wavelength transmissions from around the world that have been bounced off of the ionosphere. These signals commonly result in heavily polluted data that radio astronomers are forced to invest great efforts to address in either pre-processing, post-processing, or both. The design of LoFASM, with 5 stations looking at the same region of sky but separated by huge distances, allows for the immediate discrimination of unwelcome RFI signals via anti-coincident data analysis. Signals that show up at one or even two of the stations alone but are not present in data recorded by the remaining stations can easily be characterized as terrestrial in nature. Figure 2.2 shows a map of the

continental US depicting the locations of each of the five LoFASM stations.

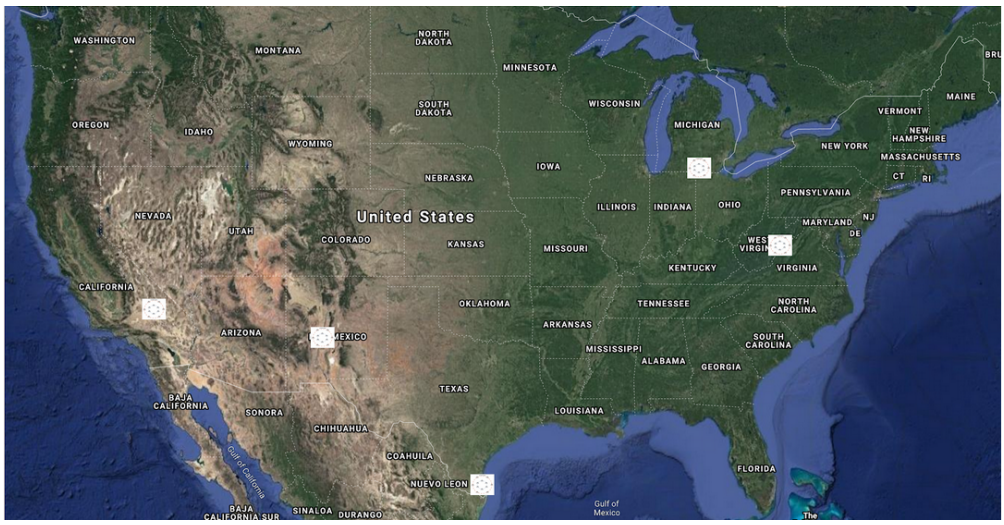

Figure 2.2: A map showing the locations of all five LoFASM stations across the continental United States

Moreover, in addition to the rings in the main array, each active LoFASM station contains an additional antenna, called the "outrigger", located ENE from the main grouping. LoFASM III, which is located at the Green Bank Observatory in Green Bank, West Virginia, has two outrigger antennas, the farthest of which is $\sim 351\,\mathrm{m}$ away from the main array (see Figure 2.3). The placement of these outriggers allows sources to be localized in the East-West direction through time delay interferometry. Since RFI from fixed sources will have constant delays between the outrigger and main antenna grouping, whereas astrophysical sources will have time varying delays as they pass overhead, the interferometric capabilities of the LoFASM stations provide an additional avenue through which to identify and mitigate RFI.

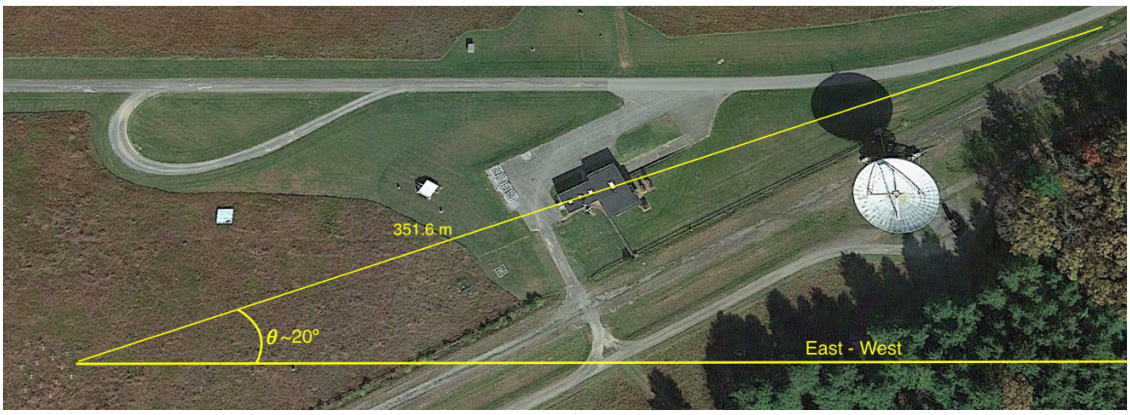

Figure 2.3: LoFASM III antenna array located at Green Bank, West Virginia. At just over 350 m, the outrigger antenna located in the top right of the image forms the longest baseline in the LoFASM network.

The design philosophy of LoFASM is simplicity. Built almost entirely out of off-the-shelf equipment designed for the LWA project, LoFASM leverages years of Office of Naval Research (ONR) and Department of Defense (DoD) investment in long wavelength antenna engineering and experience. This approach enabled a fast and successful facility deployment. The LoFASM design consists of five separate stations each made up of 12 main array crossed dipole antenna stands and an outrigger. The stations are located several thousand kilometers apart but have overlapping views of the sky, allowing us to distinguish local RFI from coincident signals of interest. The current roster of stations is LoFASM I (located in Port Mansfield, Texas), LoFASM II (located at the north arm of the Jansky Very Large Array in New Mexico), LoFASM III (located at the Green Bank Observatory, West Virginia), LoFASM IV (located at the Venus station of the Goldstone Deep Space Communication Complex, California), and LoFASM V (a sister station located in Hillsdale, Michigan which is maintained by Dr. Tim Dolch and his local students). Table 2.1 contains the locations of each of the LoFASM stations, along with their operational status (as of this writing) and bearing. The array bearings represent the rotation of the main LoFASM arrays with respect to North. The bearing angle θ_b, is measured as depicted in Figure B.1. The outrigger antenna coordinates, baseline displacement distances, and headings, as measured Eastward

from North, are contained in Table 2.2. As the only station to not have a dedicated outrigger antenna, LoFASM II is omitted from this table.

In this chapter I break down the various components that make up a LoFASM station, including the use of the LWA style antenna elements, the architectural design of the array itself, the implementation of an analog signal chain that reduces the number RF signals that need to be digitized and recorded, and the backend recording system.

Station	Array Lat.	Array Lon.	Bearing	Status
LoFASM I	26°33'19.57"N	-97°26'31.14"E	-15.28°	Active
LoFASM II	34°14'47.83"N	-107°38'24.27"E	14.66°	Inactive
LoFASM III	38°25'44.56"N	-79°50'46.45"E	-18.43°	Active
LoFASM IV	35°14'50.01"N	-116°47'35.77"E	-9.45°	Active
LoFASM V	41°56'15.56"N	-84°36'50.33"E	-15°	Active

Table 2.1: Locations of each of the LoFASM stations and their current status.

Station	Outrigger Lat.	Outrigger Lon.	Baseline	Heading
LoFASM I	26°33'21.69"N	97°26'25.76"W	162.83 m	66.04°
LoFASM III	38°25'48.50"N	-79°50'32.83"E	351.6 m	69.73°
LoFASM IV	35°14'51.42"N	-116°47'27.90"E	203 m	77.4°
LoFASM V	41°56'15.20"N	-84°36'57.12"E	156.4 m	85.86°

Table 2.2: Locations of each station's outrigger antenna and accompanying baseline information.

2.1 Station Architecture Design

2.1.1 Antenna Elements

The antennas that are used in the LoFASM system were originally developed for use in the LWA by the U.S. Naval Research Laboratory, the University of New Mexico, and the Jet Propulsion Laboratory. This antenna design encompasses the active front end electronics (FEEs) at the core of the antenna, the antennas themselves, as well as the structure on

which they are installed. Due to electrical considerations, the antenna elements were chosen to be broad in shape in order to improve the inherent bandwidth characteristics over those of a thin-wire dipole, such as those used in LOFAR (see Figure 2.5 below). Furthermore, by the time LoFASM was conceptualized the LWA antennas had been demonstrated to work well in the 20-88 MHz spectral region. Moreover, the active electronics in each antenna element were successfully implemented to be sky noise dominated in the spectral region of interest, with an inherent noise temperature better than 6 dB below the Galactic background noise temperature (Hicks et al. [2012]). This is great from a low frequency instrumentation perspective because it removes the need to use expensive and difficult to maintain cryogenics to cool the receivers below the noise temperature of the Galactic background. Clearly, the LWA style antennas were the ideal candidate for use in a new low frequency radio instrument for transient studies.

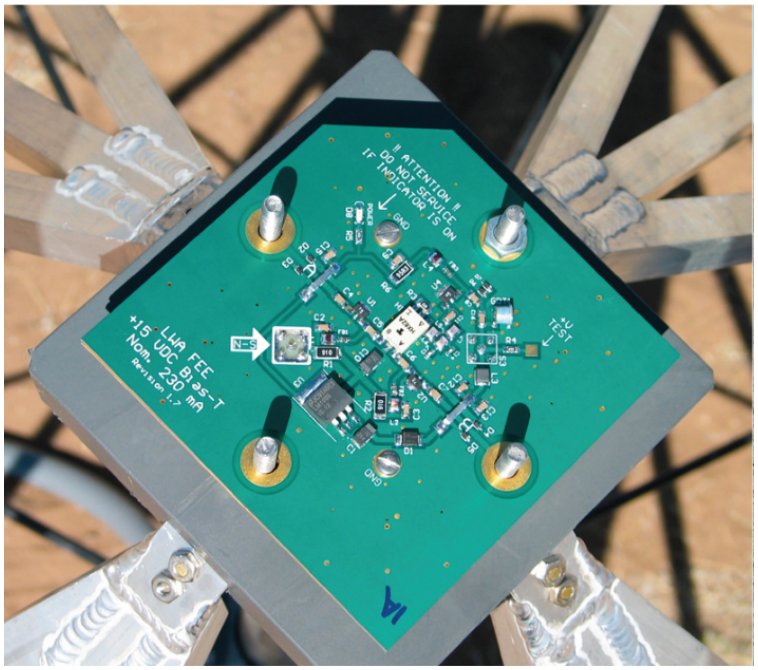

Figure 2.4: An image of an FEE circuit board. Each LWA style antenna, including those used in the LoFASM arrays, house a similar board. Credit: Hicks et al. [2012]

Figure 2.5: An image of an LWA style antenna used in the LoFASM III installation at Green Bank, West Virginia.

Another consideration was the beam pattern of the antennas. For use in an all sky monitor, the selected antennas needed to have as large a field of view as possible throughout the entire 10-88 MHz band, with a particular emphasis placed on the 20 MHz region. This is another area in which the careful design of the LWA antennas delivered. An extensive study and characterization of the antenna elements and their operational capabilities is provided in Hicks et al. [2012].

For our purposes I want to highlight the beam pattern of the antennas at 20 MHz (see Figure 2.6 below) to establish what is meant by "wide field of view". Within LoFASM, parametric measurements of the LWA antenna designs were taken from Dowell [2011] and used to simulate the E plan power patterns at various frequencies. This was done in part to supplement our own understanding of the antenna capabilities as well as to inform future calibration efforts. Figures 2.7 and 2.8 show the results of these simulations for 10-88 MHz. While these simulations match those of the LWA in the low frequency regions, they do seem deviate from what is expected at the higher frequencies. An investigation as to the cause for this discrepancy remains on the to-do list for the LoFASM team. Since the LoFASM array

configuration was primarily designed to maximize use at frequencies closer to 20 MHz (see 2.1.2), the aforementioned disagreements in the simulated power pattern of the antennas have not yet been prioritized.

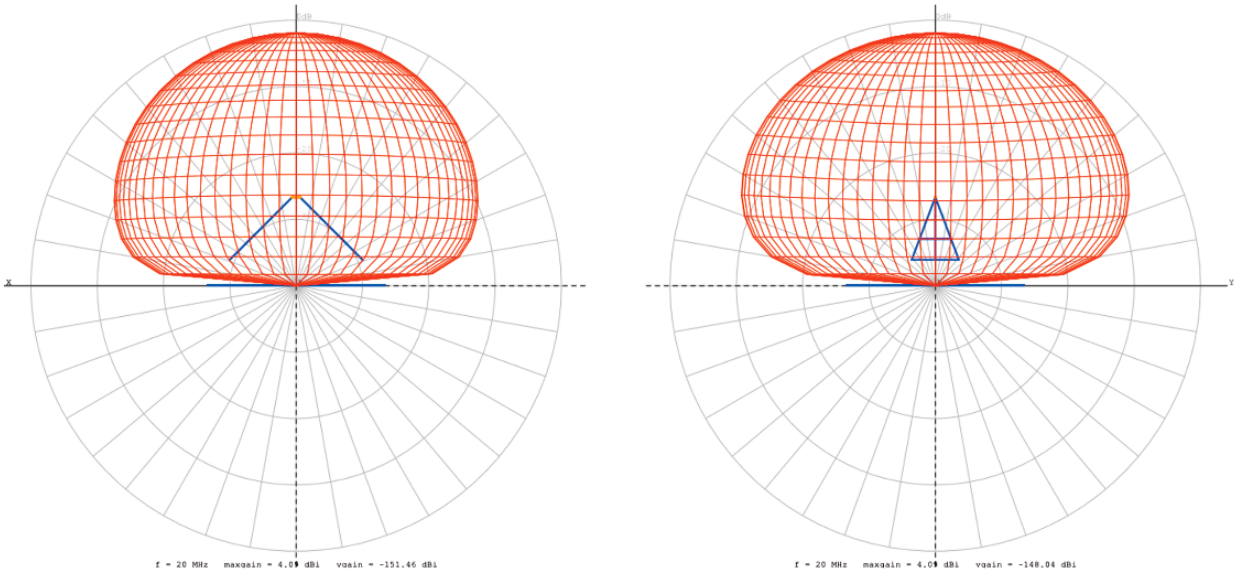

Figure 2.6: Simulated E and H plane power patterns at 20 MHz for the LWA antenna design. The scale is logarithmic total power with a normalization of unity at the zenith and -10 dB per radial division below that. E-plane patterns are on the left and H-plane patterns are on the right. The blue vertex in the left hand figures and the blue crossed/barred triangles in the right hand figures represent the antenna viewed edge on and front on, respectively. The blue line along the horizontal axis in all figures represents the ground screen viewed edge on. Credit: Hicks et al. [2012]

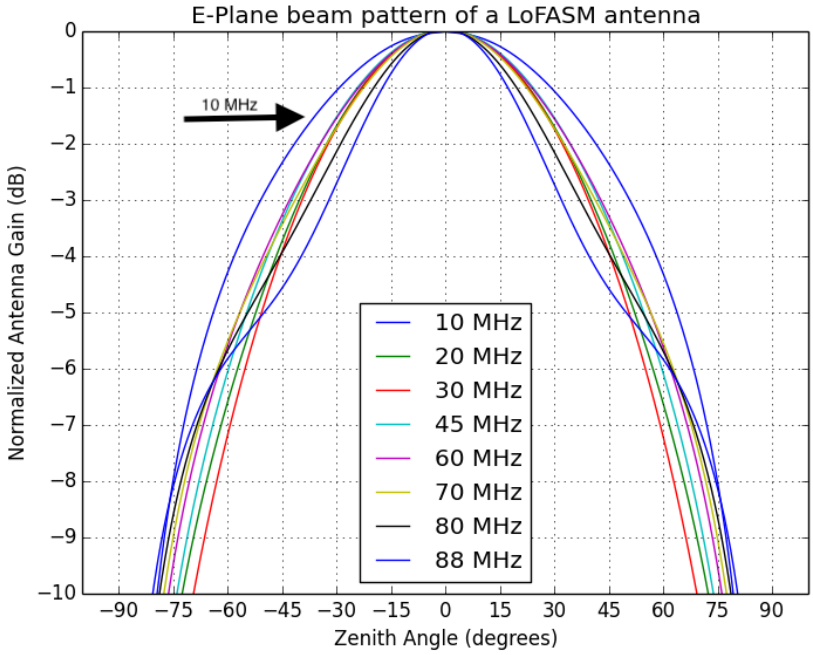

Figure 2.7: A simulation depicting the expected E-plane beam pattern of a LoFASM antenna at various frequencies from 10-88 MHz based on a frequency dependent parametric model of the antenna elements. Since two traces (10 MHz & 88 MHz) are marked with the same color in the figure, a black arrow is used to identify the 10 MHz line. Murray [2017], Dowell [2011]

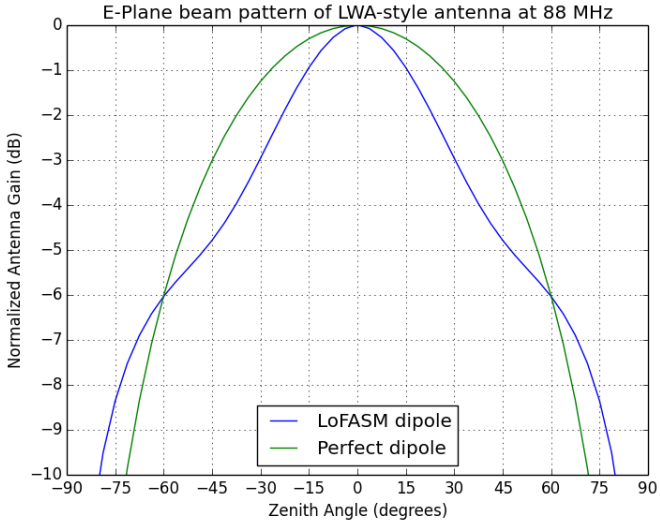

Figure 2.8: A simulation comparing the expected E-plane beam pattern of a LoFASM antenna element at 88 MHz to the beam Pattern of a perfect dipole. Murray [2017], Dowell [2011]

Figure 2.9: The very first LoFASM antenna shortly after being constructed by undergraduate students at the University of Texas at Brownsville's (UTB) Arecibo Remote Command Center (ARCC). UTB has since dissolved and is now the Brownsville campus of the University of Texas Rio Grande Valley

2.1.2 Antenna Placement

This section analyzes the properties of LoFASM's Double Ring Close-Packed element configuration (see 2.10) and shows that it appears to be an optimal configuration to reject (significantly attenuate) unwanted RFI coming from the horizon.

For a LoFASM station, system noise temperature is dominated by two main sources: the Galactic background and terrestrial RFI due to widespread terrestrial use of the HF and VHF bands. The design of the LoFASM array antenna configuration was driven by two overarching goals: to optimize sky coverage given a fixed number of antennas and remain as insensitive to terrestrial (e.g. low altitude) sources. In essence this was to facilitate the development of an antenna configuration containing 12 antennas that, when their signals are combined properly, form a beam that is very good at looking *up* but decidedly (and purposefully) poor for looking horizontally. Since the sub-100 MHz spectrum has been heavily polluted by RFI since the dawn of commercial RF use (this the reason that Karl Jansky got his original assignment at Bell Laboratories that lead him to discover the first extraterrestrial RF "star

noise") and most RFI is generated by ground-based instruments, RFI sources can effectively be considered low altitude radio sources. This combined with the fact that for any type of astronomy one needs to point up towards the sky, it made sense during the conceptualization of LoFASM to seek to develop an instrument capable of attenuating RF signals originating from the horizon.

The size of the radius of the inner ring effectively sets the optimal observing frequency for a station. The distance between the center of the configuration and the elements in the inner ring determines the range of frequencies that will be most attenuated at the horizon, as well as the viewable region of the sky. In practice, the inner radius has been set to 441 cm, thus reducing 20 MHz radiation by almost 40 dB at the horizon. Following the same close-packing of identical hexagons (i.e. the double ring configuration), the radius of the outer ring is fixed at $\sqrt{3}$ times the radius of the inner ring. This double ring configuration maximizes the instantaneous sky coverage at each individual station while minimizing the effects of RFI originating from the horizon.

The double ring configuration allows for two distinct combinations of signals from the inner and outer rings, making the telescope sensitive to different areas of the sky. When the signals added together in phase, the region of maximum sensitivity is directly overhead (i.e. the beam points up). On the other hand, when added out of phase the array will attenuate signals from overhead and be most sensitive to signals originating from the horizon.

For LoFASM's purposes with respect to the passive attenuation of RF signals originating from the horizon (horizon rejection), an altitude cutoff of 10° above the horizon was chosen. The determination of an antenna configuration that results in the highest horizon rejection for a set of 12 elements can be reduced to a minimization problem. By adding together all of the signals from the 12 antennas in the main array coherently, one can numerically calculate the normalized power patter, $B(\theta, \phi)$, for a station.

Modeling a LoFASM station as a set of N antennas, each located at a point in space

denoted by the displacement vector $\boldsymbol{x_j}$, where the antenna index, j, is allowed to run from 1 to N, the electric field incident on the jth antenna due to a plane wave is given by

$$\boldsymbol{E} = E_0 \hat{\boldsymbol{p}} e^{i(\boldsymbol{k}\cdot\boldsymbol{x_j} - \omega t)}, \tag{2.1}$$

where $\boldsymbol{k}$ is the wave vector and points in the direction of the wave's propagation, ω is the angular frequency of the wave, E_o is the amplitude of the electric field, and $\hat{\boldsymbol{p}}$ is a unit vector that points in the direction of the electric field's polarization. Additionally, the time-dependent voltage induced across each antenna's terminals or blades by the incident plane wave is

$$V_j(t) = G_n(\boldsymbol{k}, \boldsymbol{p}) E_o e^{i(\boldsymbol{k}\cdot\boldsymbol{x_j} - \omega t)}, \tag{2.2}$$

where $V_j(t)$ is the voltage across the jth antenna's terminals, $G_n(\boldsymbol{k}, \boldsymbol{p})$ is the antenna's gain, and the subscript n denotes the polarization of the antenna element. On each antenna stand are actually two orthogonal dipole element pairs, each forming an independent antenna. Thus the antenna stand and the two pairs of dipole elements are collectively called a cross-dipole antenna even though they are electrically completely independent of each other. All antennas installed as part of a LoFASM installation are oriented such that one polarization is aligned North-South and the other is aligned East-West, so the subscript n in Equation 2.2 can only take one of these two values.

The power pattern, $P \sim |V|^2$, in a coherently summed signal from all antennas of the same polarization in a ring is given by

$$P = \sum_{j,l} |G_n|^2 |E_0|^2 e^{i\boldsymbol{k}\cdot(\boldsymbol{x}_j - \boldsymbol{x}_l)} \tag{2.3}$$

where l and j are both antenna indices. The total power from both rings in both polarizations

(four total contributions) gives us

$$P_T = \sum_{j,l} A_T |E_o|^2 e^{i\boldsymbol{k}\cdot(\boldsymbol{x}_j - \boldsymbol{x}_l)}, \tag{2.4}$$

where

$$A_T(\theta) = A_0 \frac{1 + \cos(\theta)^2}{2} \tag{2.5}$$

contains all the information relating to the antenna gains and polarizations, the constant A_0 depends on the geometry of the antenna, and the angle θ is measured off of zenith. Rewriting Equation 2.4 and normalizing by its maximum value one arrives at the normalized beam pattern

$$B(\theta, \phi) = \left(\frac{1 + cos(\theta)^2}{2} \right) \frac{1}{N^2} \sum_{j,l} e^{i\boldsymbol{k}(\theta,\phi)\cdot(\boldsymbol{x}_j - \boldsymbol{x}_l)}. \tag{2.6}$$

Figure 2.11 shows the normalized beam pattern at 20 MHz as a function of θ and ϕ, where θ and ϕ are the azimuth and zenith angles, respectively. A more thorough derivation of Equation 2.6 is given in Miller [2012]. For the purposes of rejecting local RFI, an antenna configuration with the lowest possible H/Ω_0 was selected, where Ω_0 is the antenna beam solid angle given by

$$\Omega_0 = \int B d\Omega \tag{2.7}$$

and H is defined by

$$H = \int_{\pi/2 - \delta < \theta < \pi/2} B(\theta, \phi) d\Omega \tag{2.8}$$

where δ represents the adjusted altitude of the horizon. A Monte-Carlo simulation analysis by Miller [2012] arrived at the values in Table 2.3 corresponding to the smallest value of H/Ω_0 and their corresponding inner radii for frequencies ranging from 5-30 MHz (Miller [2012]).

Frequency (MHz)	5	10	15	20	25	30
Radius (m)	17.4	8.79	6.04	4.53	3.51	3.01
H/Ω_0 (dB)	84.4	91.1	91.8	91.5	93.1	93.9

Table 2.3: Table of H/Ω_0 values and their corresponding inner radii at various frequencies from Miller [2012]

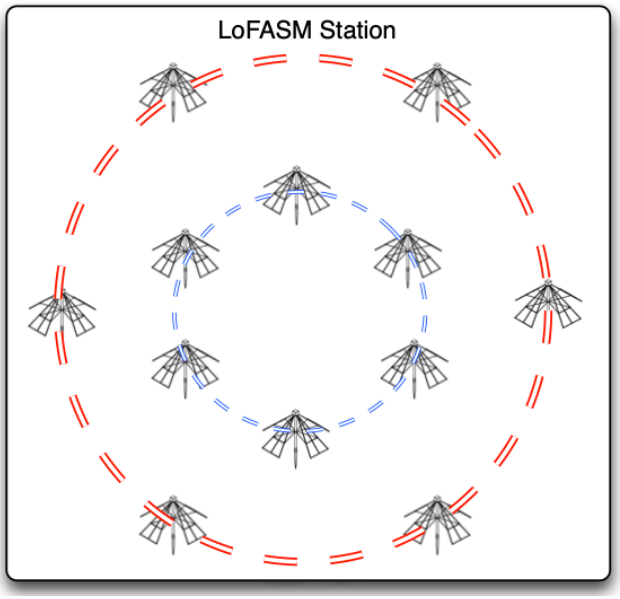

Figure 2.10: The antenna configuration of a LoFASM station consisting of 12 LWA style active cross-dipole antennas arranged as a pair of concentric rings, each containing 6 elements. The radius of the inner ring, marked in blue, is set at $R_{inner} = 441\,\text{cm}$ and the radius of the outer ring, marked in red, is $R_{outer} = \sqrt{3}R_{inner} = 763.83\,\text{cm}$ to maximize horizon rejection in the synthesized beam at 20 MHz. (Miller [2012]) Image Credit: Dartez [2014]

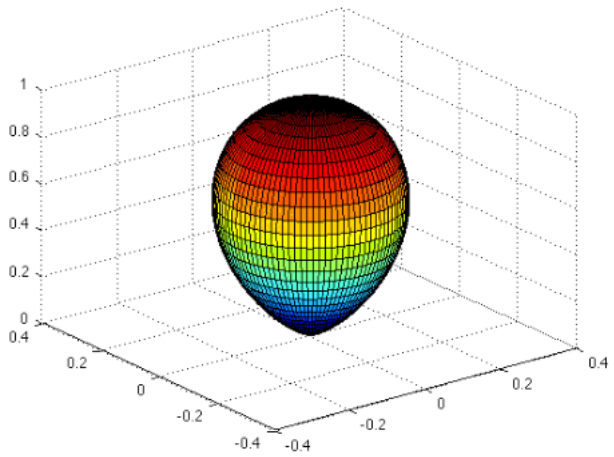

Figure 2.11: A simulation of the normalized LoFASM beam pattern at $\nu = 20\,\text{MHz}$ for an array configuration optimized for horizon rejection at 20 MHz (i.e. an inner radius of 4.42 m.) The color pattern represents the sensitivity, with red indicating the highest sensitivity and blue the lowest. Credit: Miller [2012]

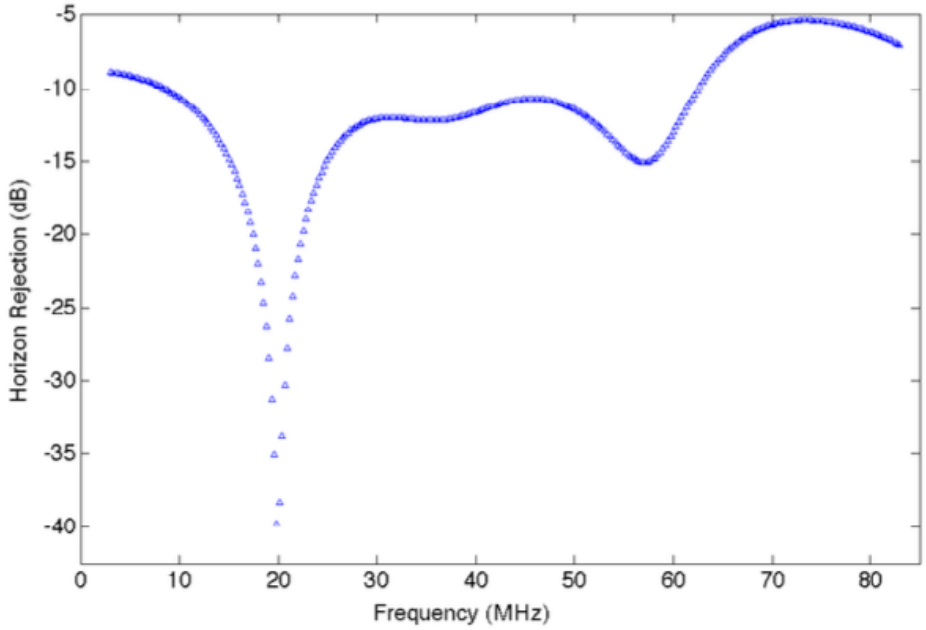

Figure 2.12: A simulation of the attenuation applied to RF incident from the horizon (horizon rejection). Plotted is H/Ω_0 for LoFASM's double ring configuration optimized for 20 MHz. The station is specifically tuned to attenuate low altitude signals, assumed to be of terrestrial origin, by nearly 40 dB. Credit: Miller [2012]

The LoFASM system can be modeled as a two component system where the temperature due to RF from the horizon is $T_{sky} + \Delta T_h$ and the temperature from everywhere else in the

field of view is simply T_{sky}. The received noise power in a single polarization becomes

$$P_n = \frac{A_m k_b T_{sky} \Omega_0}{\lambda^2} + \int_{\pi/2-\delta<\theta<\pi/2} \frac{A_m k_b \Delta T_h}{\lambda^2} B(\theta, \phi) d\Omega \tag{2.9}$$

where A_m is the effective area of the telescope and k_b is the Boltzmann's constant. With the help of Equation 2.8, Equation 2.9 becomes

$$P_n = \frac{A_m k_b T_{sky} \Omega_0}{\lambda^2} \left(1 + \frac{\Delta T_h}{T_{sky}} \frac{H}{\Omega_0}\right), \tag{2.10}$$

which can be further reduced to define an equivalent system temperature:

$$T_{sys} = T_{sky} \left(1 + \frac{\Delta T_h}{T_{sky}} \frac{H}{\Omega_0}\right). \tag{2.11}$$

This suggests that horizon rejection will have implications on total system noise temperature. In a high local RFI environment T_{sys} will be dominated by the RFI coming in from the horizon. Therefore, minimizing H/Ω_0 and rejecting horizon RFI to as much as possible will effectively reduce the total system temperature.

2.1.3 The Analog Signal Chain

Every LoFASM station has the same analog signal chain running into the control room. The signals from each ring of antennas are summed in phase using a 6-to-1 analog combiner physically placed at the center of the station for each polarization (see Figures 2.13 and 2.14). This results in four signals from each station's "main array", one for each of the two polarizations corresponding to each of the two rings. These four signals are then transmitted along direct burial LMR-400 cables and brought to a building or electronics shelter located at least 300 m away from the antenna rings. This distance between the antennas and the electronics helps prevent any RFI generated by the digital backend electronics from being

picked up by the active receivers housed in the antennas.

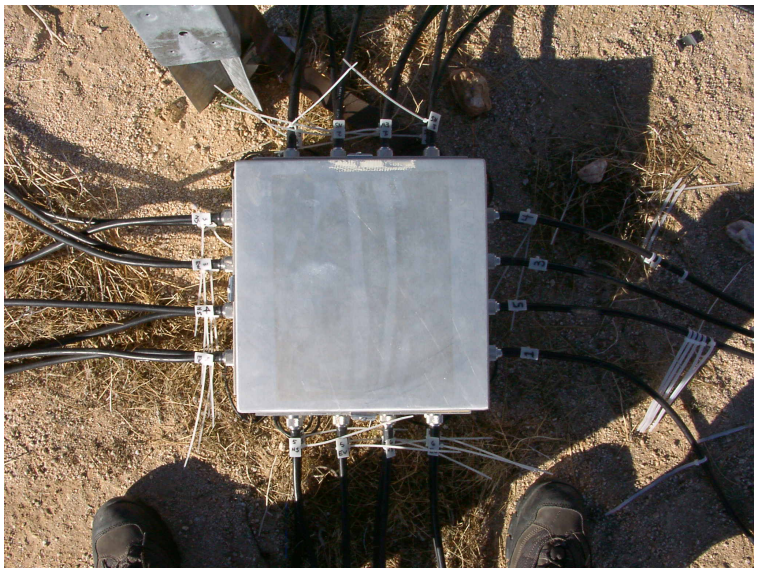

Figure 2.13: A top down view of the combiner box installed at LoFASM IV at the Goldstone Deep Space Communications Complex in California.

Figure 2.14: The combiner box installed at LoFASM I in Port Mansfield, Texas that was opened up to be serviced by the LoFASM field repair technicians (a.k.a. students). The various small cables connected the bulkhead connectors on the enclosure walls vary in electrical length so as to maximize ensure that all of the signals in each ring of each polarization are phase matched so that they interfere constructively when they are summed in the 6-to-1 combiners.

Once in the electronics shelter, the signals are passed through an active analog receiver (ARX) module. The ARX serves to overcome the power losses due to the span of cabling

running from the electronics shelter to the antennas. Additionally, the ARX provides additional gain using low noise amplifiers while also using RF filters to attenuate RFI in the commercial AM and FM radio bands. Furthermore, in some LoFASM stations, the ARX also houses a bias-T (sometimes spelled "bias-Tee") module. The bias-T couples a DC current onto the signal lines which allows us to power the active components in each antenna using the same line that is used to receive data, cutting costs and reducing the wiring complexity of the instrument.

Early designs for the LoFASM ARX were based off of modified LWA prototype receivers. (Rivera [2012]) Those designs, while likely great for prototyping with a large instrument such as the LWA, which contains hundreds of individually sampled elements, were found to be overly complex and cumbersome to use for a smaller instrument such as a LoFASM station. As a result, the LoFASM ARX has evolved over time to meet the needs of a single LoFASM station. One early design consisted of a modular system in which each component in the ARX was placed on a separate breakout board and connected, as needed, to other components in the signal chain via simple RF SMA connectors that were soldered onto the printed circuit boards (PCBs). The eight connectors located on the ends of the board in Figure 2.16 are examples of surface mount industry standard RF SMA connectors. This modular revision of the ARX was aptly named the "mARX". The separation of each major signal chain component onto its own PCB was great for quick prototyping in the early LoFASM stages. Unfortunately, we later learned that these units would not be very good in production settings. Over time, the RF SMA connectors would suffer from fatigue from either being used too often during testing or from the fact that they were used in long chains without proper support. As a result, once the noise characteristics for a particular site, and thus the level of RFI cleaning that would be needed to be performed in analog, was known, we reverted to a single module or PCB ARX design that incorporated the right amount of filtering, attenuation, or amplification stages that were necessary. This third revision, single

module ARX design was dubbed the uni-modular or Uni-mARX design (Murray [2015]). More recently, we've used a robust iteration of the ARX with enhancements to improve the RF filtering and stability of the LoFASM signal chain. The full circuit diagram and parts list for the latest ARX design revision, which is currently designed and maintained by Brent Cole at UTRGV, are provided in Appendix A.

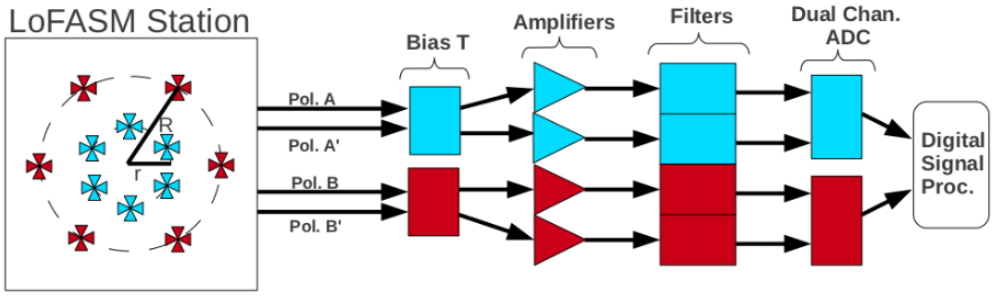

Figure 2.15: A schematic of the LoFASM signal path from the active antenna elements on the left to the digital signal processing (DSP) unit on the right. Since each element consists of a cross dipole antenna two linearly polarized signals are provided by each element, each with its own cabling. The signals from each polarization in each ring are combined in phase via a set of analog combiners located at the center of the array. The polarization pairs (A, A'), and (B, B') depicted in the figure represent the two resultant polarized signals from each ring (i.e. channels A and A' contain the orthogonal linearly polarized signals from the antennas in one ring, and B and B' contain the other). Once inside the electronics shelter the signals go through the "bias-T" and a few stages of filtering and amplification before being sent off to the digital processing backend to be digitized and Fourier transformed. Credit: Rivera [2012]

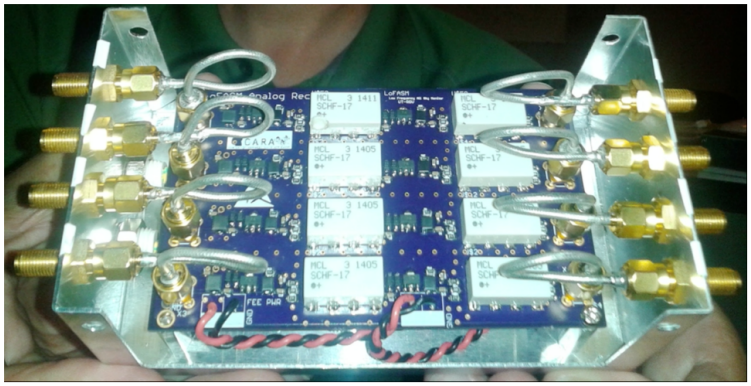

Figure 2.16: An early version the ARX board used in LoFASM stations. Murray [2017]

2.2 The 100 MHz Full Stokes Spectrometer

In each LoFASM Station, RF signals from the individual LoFASM dipole antennas are combined in phase in analog, sent through an analog receiver chain and finally passed over to the digital backend where they are digitally sampled and processed using a 4-input full Stokes 100 MHz correlating spectrometer, known as the LoFASM Correlator, that I designed and implemented using, among other technologies, a reconfigurable field programmable gate array (FPGA) based system. The FPGA is hosted on a board called the Reconfigurable Open Architecture Computing Hardware 1 (ROACH-1), which was designed through a collaborative effort called The Collaboration for Astronomy Signal Processing and Electronics Research (CASPER), whose primary goal is to streamline and simplify the design flow of radio astronomy instrumentation by promoting design reuse through the development of platform-independent, open-source hardware and software.

The LoFASM beam must be synthesized, that is produced in software, using the four inputs coming from the antennas in the main array, the outrigger, or some combination of the two. The first component of the digital backend processing pipeline is the digitization of the analog signals. This is the process of converting the continuous RF signals into a digital format. Figure 2.17 shows a pictorial representation of the digitization effects imposed on a single during analog to digital conversion.

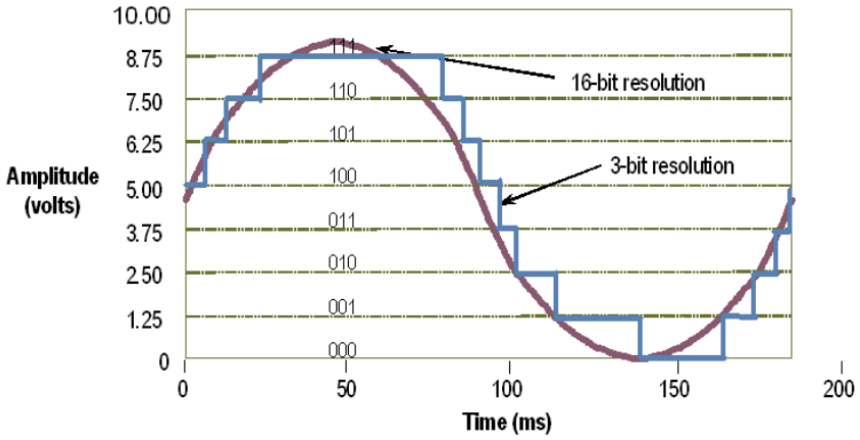

Figure 2.17: A representation of the quantization effects imposed on a continuous signal due to the discrete sampling of an ADC. The resolution of the digitized signal is determined by the effective number of bits used during the conversion a signal's information from the continuous to the discrete regime.

After analog-to-digital conversion comes the LoFASM spectrometer. Spectrometers are a popular tool built into many receiver backends designed to measure the power spectral density (PSD). Historically, spectrometers were implemented by highly specialized hardware, but thanks to the multitude of technological advancements of the past few decades more and more instruments are being brought online using reconfigurable backends using technologies such as FPGA's, graphics processing units (GPUs), general purpose computers, and more recently even small credit card sized single board computers such as Raspberry Pis (Hickish et al. [2016], Denman et al. [2015], Jones [2010], Fa-bao et al. [2020]). In designing spectrometers, emphasis is typically placed on the spectral information contained in the radiation field. To accomplish this, receivers must be single sideband and the frequency reslution, $\Delta\nu$, must be as small as possible, often in the kHz range.

If a spectral resolution of $\Delta\nu$ is to be achieved and maintained over time for a spectrometer based system, the temporal stability of all components in the system that enter critically into the frequency response have to maintained to better than $0.1\Delta\nu$. This is particularly important for the local oscillators in the system. Therefore, where possible, it is preferable to obtain a local oscillator signal from an extremely stable source, such as a rubidium clock

or a hydrogen maser. To this end, clock synthesizers at most LoFASM stations pull 10 MHz reference signals from rubidium clocks in the electronics shelters.

The LoFASM spectrometer samples a 100 MHz bandwidth across 1024 discrete frequency channels, resulting in a bandwidth of $\Delta\nu \approx 97.6\,\text{kHz}$. This bandwidth is due to limitations imposed by the amount of logic that can fit on a Xilinx Virtex-5 FPGA and the fact that the LoFASM ADC's sample the RF on the four input signals at a whopping 14-bit resolution, whereas most other successful radio telescope backends traditionally use 8-bit quantization. Some even get by with 1-bit sampling! The reason that the LoFASM backend was designed with such a high sampling resolution can be traced back to dynamic range. Unlike most other radio instruments, most LoFASM stations did not have the luxury of being installed in remote radio quiet zones. LoFASM II at the North Arm of the Karl G. Jansky Very Large Array and LoFASM III at the Green Bank Observatory in Green Bank, West Virginia did, however. Unfortunately, LoFASM II is not currently active. But LoFASM III produces some of the cleanest data out of all stations in the LoFASM network, thanks to the Zone 1 Radio Quiet Zone classification, which one of the many perks of having a radio instrument co-located with a major world-class radio observatory. Interestingly, however, there are times when signals at LoFASM III contain a lot of RFI. It has been noted that LoFASM IV, which is located at the Venus site of the Goldstone Deep Communications Complex in California and right next to Fort Irwin, a US Army base where portions of the military regularly train for combat oversees, can sometimes produce data products with less RFI pollution than those recorded at LoFASM III.

The limiting sensitivity of a spectrometer is given by

$$\frac{\Delta T}{T_{sys}} = \frac{K}{\sqrt{\Delta\nu\tau}} \tag{2.12}$$

where $K = \sqrt{2}$ is the noise performance factor of a correlation receiver, ΔT is the receiver noise instability caused by variations in the output power due to gain variations in the

receiver, T_{sys} is the total system temperature, and τ is the total integration time of the spectrometer. For sensitive measurements, it is preferable to keep the left hand side of Equation 2.12 as small as possible. That is to say that it is best to ensure that variations in system response due to noise are on orders much smaller than the total system temperature of the instrument. As a result, the integration time, τ, required to reach small values of $\Delta T/T_{sys}$, can be quite large since $\Delta\nu$ is often very small. This is why spectrometer backend receivers rely so heavily on highly stable clocks, since any system errors in the backend can easily lead to fluctuations larger than the left hand side of Equation 2.12. (Wilson et al. [2004])

Spectrometers and correlators often used as methods to employ the Wiener-Khinchin theorem in practice. The Wiener-Khinchin theorem states that the autocorrelation function at some time delay τ, $R(\tau)$, and the power spectral density (PSD), $S(\nu)$, of an ergodic random process are Fourier Transform (FT) pairs.

That is to say that the PSD defined by

$$S(\nu) = \int_{-\infty}^{\infty} R(\tau) e^{-2\pi i \nu \tau} d\tau \tag{2.13}$$

where ν is a frequency, τ is a time delay, and R is a autocorrelation function, which in turn is given by

$$R(\tau) = \int_{-\infty}^{\infty} S(\nu) e^{2\pi i \nu \tau} d\nu, \tag{2.14}$$

are FT pairs. The LoFASM backend uses this relationship in the background by taking discrete real-valued samples of a continuous signal, $V(t)$, imposing a finite impulse response (effectively a windowing function), taking the Fourier Transform of the time series to end up with complex-valued voltages as a function of frequency, $V(\nu)$. Then the PSD is calculated by calculating the auto and cross correlations of all unique pairs of signals. (see Figure 2.18)

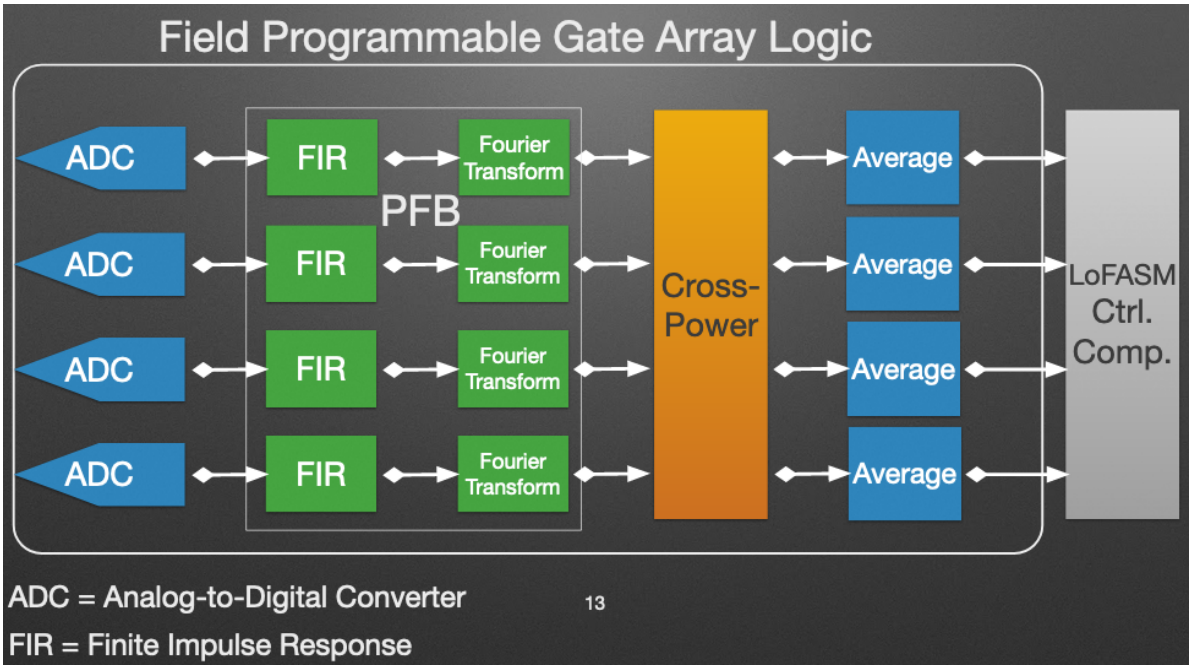

Figure 2.18: A flowchart representing the flow of operations that the LoFASM correlator firmware applies to incoming RF signals. First the signal is digitized then it is through a polyphase filterbank, which can be modeled as a finite impulse response followed by a complex Fourier transform (Price [2018]). The resultant PSD is used to calculate all possible auto and cross correlation pairs before being averaged for $\sim 83.4\,\text{ms}$. Finally the data sent over a network cable to a control computer for archival storage and post processing.

Ten data streams are produced by this process. First there are the four auto correlations corresponding to each of the four input signals from the analog system. Each of these simply takes the real-valued form of

$$|X(\nu)|^2 = X^*(\nu)X(\nu). \tag{2.15}$$

And then there are the $N(N-1)/2$ cross-correlations or cross-powers generated by calculating the values for each unique pair of inputs. These take the complex-valued form of $X^*(\nu)Y(\nu)$.

All ten data streams are then averaged for $\sim 83.4\,\text{ms}$ by the FPGA fabric before being sent over a network cable to one of the LoFASM control computers. Having the auto-correlations and cross-correlations pairs produced by backend in one place allows us to synthesize the LoFASM beam once certain parameters are known. The power detected in a single polarization

of the array is

$$P_{sum} = |V_{inner} + V_{outer}|^2, \tag{2.16}$$

where V_{inner} and V_{outer}, both functions of frequency, are the signals from the inner and outer ring, respectively, of a given polarization. Let us define $A_i(\nu)$ and $A_q(\nu)$ to be frequency-dependent gain factors that characterize each of the two distinct at the end of the RF signal path for a single polarization. Then we have

$$V_i = A_i V_{inner}, \tag{2.17}$$

$$V_q = A_q V_{outer}, \tag{2.18}$$

$$P_i = |V_i|^2, \tag{2.19}$$

and

$$P_q = |V_q|^2, \tag{2.20}$$

where V_i and V_q are the digitized LoFASM voltage signals in the frequency domain, with P_i and P_q representing the power detected in each stream. Throwing all of these terms back into our relationship for P_{sum}, we get

$$P_{sum} = \frac{P_i}{A_i^2} + \frac{P_q}{A_q^2} + \frac{2Re(V_i^* V_q)}{A_i A_q}. \tag{2.21}$$

Finally, combining the above relationship for both polarizations of the main LoFASM array gives us the full LoFASM beam optimized for 20 MHz. The trick lies with calibrating the backend such that the values for A_i and A_q can be determined. As of yet, the simulations predicting the horizon rejection properties of the LoFASM beam have not been confirmed experimentally.

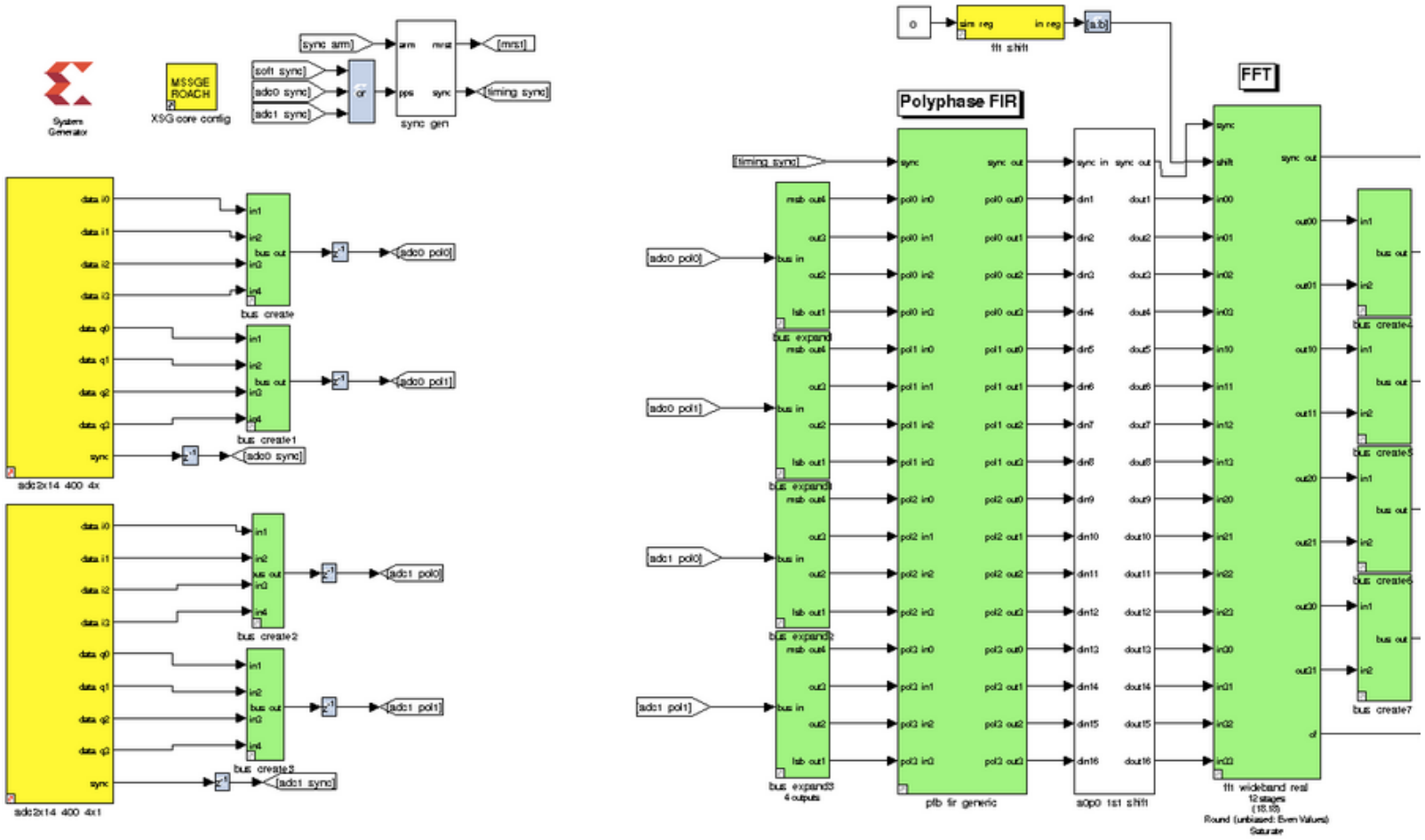

Figure 2.19: A MATLAB Simulink screenshot with a view of the flow diagram environment in which the LoFASM Correlator firmware logic was designed. Behind the scenes is a toolflow provided by the CASPER collaboration and Xilinx that allows for the rapid development and testing of novel instrument designs on reconfigurable architectures. A more intuitive understanding of the firmware logic can be found in Figure 2.18

Figure 2.20: Drone image of LoFASM V array in Hillsdale, Michigan during its installation. Credit: Andrews et al. [2019]

Figure 2.21: Drone image of researchers servicing the LoFASM V outrigger antenna in Hillsdale, Michigan shortly after installation. Credit: Rammete et al. [2019]

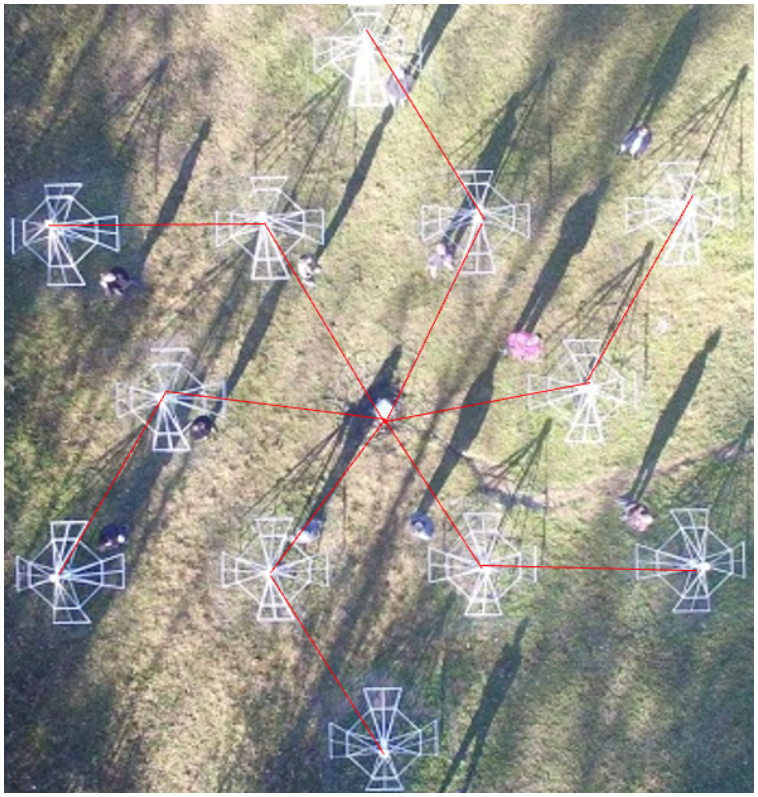

Figure 2.22: Drone image depicting the wire routing installed at LoFASM V in Hillsdale, Michigan. Credit: Niedbalski et al. [2019]

CHAPTER 3

COMMISSIONING OF THE LOFASM TELESCOPE SYSTEMS & EARLY RESULTS

This section reports on notable events recorded by LoFASM that, collectively, mark the beginning of a promising potentially significant scientific monitoring program sub-100 MHz regime. Also discussed are some data handling and preparation methods that were used to analyze the first LoFASM data products. Finally, the section is concluded with an overview of some early results from analyses that were performed on LoFASM data produced in various observing modes.

The bulk of my work has consisted of facilitating LoFASM data-taking runs, working on the development of a software data processing pipeline, and laying the groundwork for data analysis and the continuation of future data runs. Among the many targets for the commissioning of LoFASM in this inaugural chapter of its tenure is the observation of various transient events. These include terrestrial activity, such as anthropogenic signatures from passive or active radar (RFI), or naturally occurring transients such those caused by nearby lightning storms or disturbances in the ionosphere. Extraterrestrial signals originating from anywhere in the solar system are also of interest, including solar activity. Recently, there has been increasing interest with the LoFASM team to investigate whether archival data from any of the stations contains evidence of Jovian activity caused by one of its moons, Io, as it orbits and interacts with Jupiter's magnetic field. Other targets of interest comprise those of extra-solar origins, like the potential capture of an FRB during one of the data-taking runs, either from an extra-Galactic source or from within the Milky Way. Though no simultaneous detections across multiple stations have been confirmed as of yet, early data-taking runs with LoFASM have turned up several interesting artifacts in the sub-100 MHz spectrum, from potential solar activity (Figure 3.1) to possible traveling ionospheric disturbances to radar "chirps".

All LoFASM data discussed and analyzed in this work was recorded using the LoFASM spectrometer. Details of the spectrometer output are provided in Table 3.1. Additionally, it is worth noting here that a shorthand notation is used for convenience when referring to the various LoFASM data channels, each of which corresponds to data collected from a particular set of LoFASM antennas in a given polarization. An overview of these conventions is given in Table 3.2.

Parameter Name	Parameter Value
Frequency Range	0-100 MHz
Frequency Step	97.6 kHz
No. Frequency Points	1024
Sample Time	0.83 s

Table 3.1: LoFASM Spectrometer parameters. All data taken as part of this work was recorded using the LoFASM spectrometer using the above characteristics. The sample time is sometimes also called the integration time.

Channel ID	Array Channel & Polarization
INS	Inner Ring North-South
IEW	Inner Ring East-West
ONS	Outer Ring North-South
OEW	Outer Ring East-West
ORNS	Outrigger North-South
OREW	Outrigger East-West
AxB	A & B cross power

Table 3.2: Polarization naming notation conventions used for convenience. In short, the suffix "NS" or "EW" is used to denote the polarization being used. The prefix indicates the array component. "I" for signals from the inner ring, "O" for the outer ring, and "OR" for the outrigger. Additionally, all of the cross power pairs use the same notation. To indicate a cross power channel, the letter "x" is placed in between the two parent channel IDs. For example, the cross power channel between INS and ONS is denoted by INSxONS.

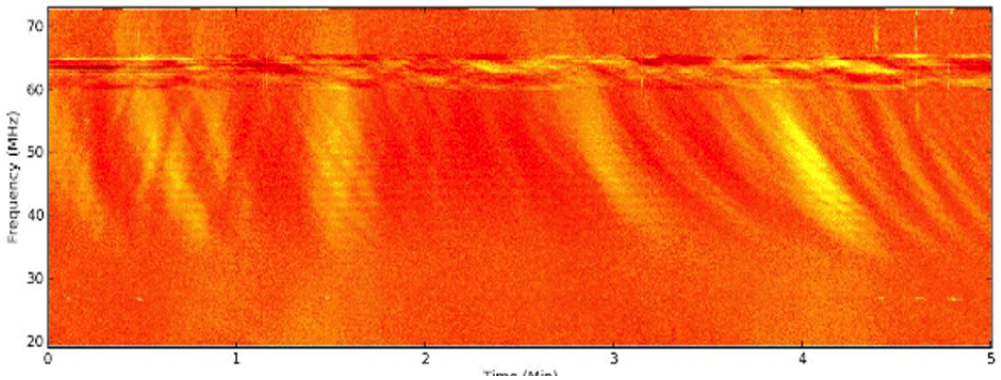

Figure 3.1: Spectral data taken at LoFASM I showing possible solar activity. Credit: Danford, A. 2016

While active, each LoFASM station accumulates roughly 100 GB of spectrogram data per day that is compressed in real time via a lossless compression algorithm to maximize hard drive space. The backlog of LoFASM data that remains to be analyzed is in the tens of terabytes and continues to grow. It is not unlikely some low frequency transient events have already been recorded by one or more of the arrays and is currently waiting to be stumbled upon by an eager researcher. The archival data bank that continues to accumulate at each station represents one of LoFASM's strengths in the field of radio telescopes. LoFASM aims to keep all of its data, endlessly scanning and recording while waiting for the implementation of a burst search pipeline that can be implemented in real time and tested on archival data. Since other telescopes are forced to throw away the majority if their data products in real time, LoFASM could very well be one of the only instruments that is truly collecting a continuous record of the low frequency radio environment that spans the North American continent.

3.1 The Data Processing Pipeline

The raw LoFASM spectrogram data product comprises the auto-correlations corresponding to each of the four RF inputs along with all of the associated cross-correlation pairs. The result is ten synchronized data streams, all of which are simultaneously generated in real

time by the digital backend (refer to Figure 2.18).

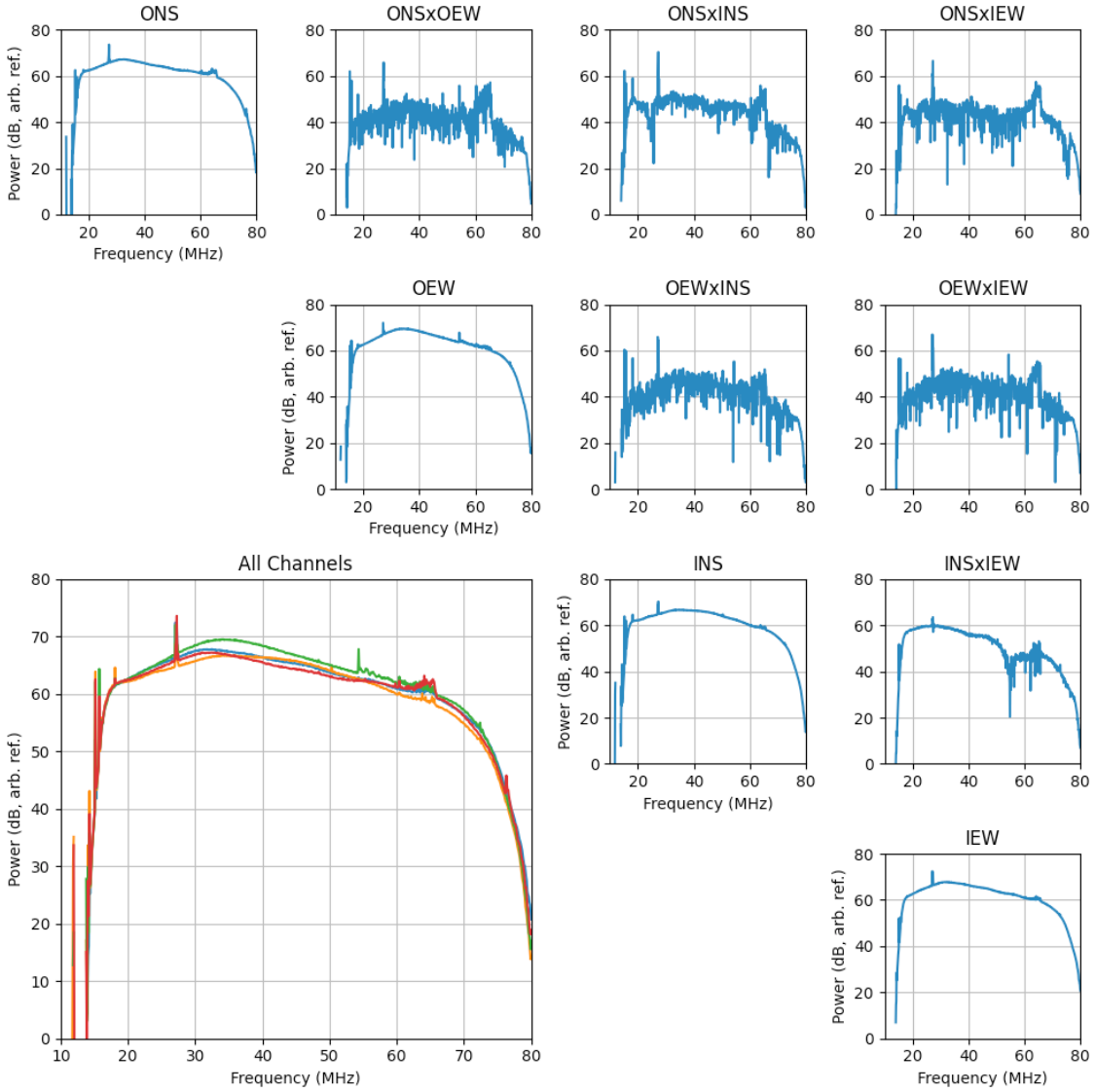

Figure 3.2: A single time sample of each of the ten data streams produced by the LoFASM correlating spectrometer. The four plots along the diagonal show the autocorrelated signals corresponding to each of the four RF inputs. These four signals are shown enlarged and overlaid in the bottom left. The remaining six figures in the top right corner show each of the cross-correlation pairs.

These data streams are interleaved and sent over a network channel to a control computer that stores them to disk in 5 minute segments. Therefore, the data streams are bundled together in the resultant data files and must be unwoven into independent data channels before they can be processed. Figure 3.2 shows all ten LoFASM channels after they've been

broken out from the raw data stream.

A pipeline for pre-processing LoFASM data files that implements mean subtraction techniques as well as methods developed to mitigate the effects of narrow band RFI has been developed to facilitate wide band spectral analyses. Figure 3.3 shows a high-level flow chart of the steps taken as part of this pipeline during the instrument's commissioning.

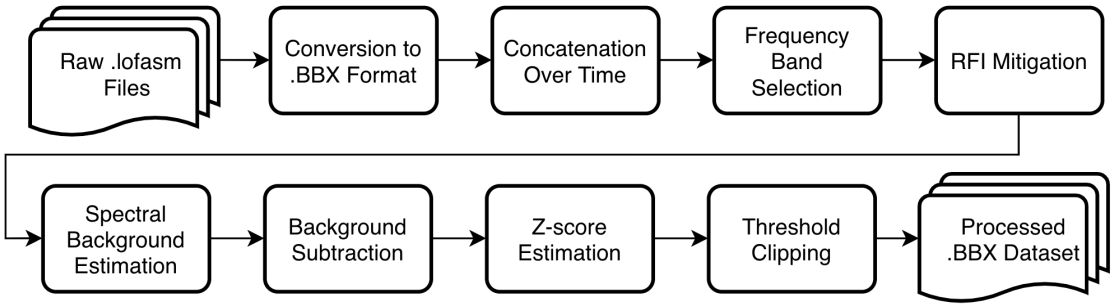

Figure 3.3: Data Processing Pipeline Flowchart

3.1.1 File Format Conversion

To facilitate a flexible data processing ecosystem, the first processing step taken with all LoFASM datasets is to break out the individual channels into data files of a manageable and reconfigurable format. This simple, yet malleable data format, which uses the extension tag *BBX*, is documented thoroughly at `https://github.com/teviet/lofasmio`.

3.1.2 File Concatenation

After file conversion to *BBX* the files are down-sampled and concatenated over time to form a single data segment that can be easily processed. Datasets chosen for observations lasting longer than the 5 minute integration time will comprise several contiguous data files. For example, a 24 hour stretch of data will consist of 24hr/5min $\approx$ 288 individual files. Care must be taken when concatenating data sets spanning a large range of time. The raw LoFASM files produced by the digital backend, which have the *.lofasm* file extension, and *BBX* files both include timestamp information in their respective header sections. Additionally, both

file formats specify the total file time span. Using this information, large data sets can be formed by properly sorting by timestamp and keeping track of any gaps present in the data (e.g. missing files) and padding them with zeros.

3.1.3 Frequency Band Selection

While the LoFASM backend implements a 100 MHz spectrometer, it is usually the case that only select regions in the spectral span can be used for analysis. To begin with, bandpass filters in the analog RF chain attenuate any signals outside of the 15-75 MHz frequency range. The analog corner frequencies can be observed in the spectral stop bands shown in Figure 3.2. As a result, a smaller subset of frequency bands within this range are usually selected for analysis. Moreover, depending on the goals of the analysis taking place, it is common for problematic frequency bands, such as those polluted by high levels of RFI, to be excised from the data set. For example, the 60-65 MHz frequency range is often dominated by RFI (refer to Figure 3.5). Alternatively, frequency band selection can also be informed by the astrophysical phenomena being studied. This is the case when searching for pulsar signals at long wavelengths. Frequency dependent characteristics and propagation effects, such as pulse dispersion, can influence the frequency range used (see Section 3.4 for a discussion on the effects of pulse dispersion).

3.1.4 Narrow Band RFI Mitigation

In many cases it is preferable to mitigate the effects of RFI instead of completely removing the affected frequency channels. RFI can present itself in various forms. Persistent RFI, whether narrow- or broad-band, typically results in bands that are not useful for the study of astrophysical phenomena. However, transient narrow-band RFI can often be mitigated easily, especially if it is not periodic. Figure 3.4 shows a time series taken at 48 MHz that stretches for 24 hours with the occasional spike present in the data. The power recorded

in the power spikes is often orders of magnitude greater than that of the neighboring data points. This is usually attributed to local RFI incident on the antennas from an unknown source. These spikes can be removed or dampened with the use of a median filter that runs over time via a sliding window. The length of the window is chosen to be as short as possible such that the effects of RFI are mitigated but changes in the underlying structure of the noise are not obscured.

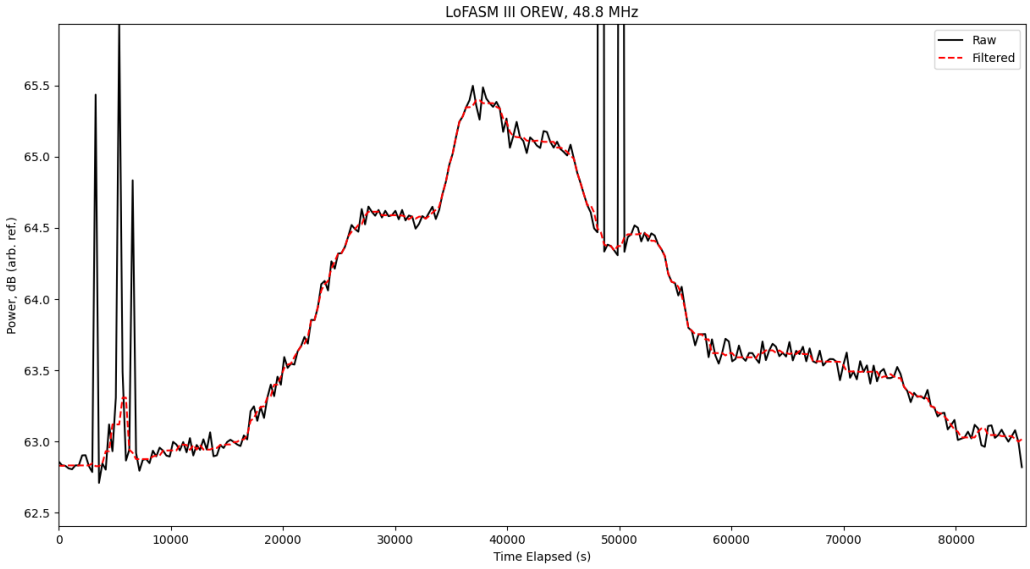

Figure 3.4: Narrow band time series over 24 hours. The black line is raw data taken at 48.8 MHz with LoFASM III showing transient narrow band spikes possibly due to local RFI. The red line shows the result of applying a median filter with a short kernel. The RFI spikes are removed and the overall level of the noise is preserved.

3.1.5 Mean Subtraction

To facilitate the detection of time variable signals it is useful to estimate the background noise level, which is frequency dependent, for a given dataset and remove it. The result will be a spectrum with zero mean consisting of noise and, potentially, an astrophysically meaningful signal that is represented as offset from the baseline. This process allows for the removal of the relatively stagnant background and the isolation of the transient. However,

estimating the background level is not straight forward. In practice, methods for background estimation are often dataset-dependent. In the case of LoFASM data, the steps taken for estimating the background are:

1. Running median filter over time for each frequency
2. Running average over time for each frequency
3. and, Median filter over frequency.

The average in step 2 above is calculated as

$$\mu(\nu, t_j) = \frac{1}{n} \sum_{i=j-r}^{j+r} x(\nu, t_i), \tag{3.1}$$

where $\mu(\nu, t_j)$ is the sampled mean of the PSD at frequency ν, $n = 2r + 1$ is the sample size encapsulated by the running window, "radius" r is the window size over which the running mean is computed in either direction, and $x(\nu, t_i)$ is the PSD value at frequency ν and time t_i. The sliding median filter is represented as

$$y_{\text{Med}}(\theta_j) = \text{Med}_{i=j-r}^{j+r} x(\theta_i), \tag{3.2}$$

where $y_{\text{Med}}(\theta_j)$ is the result of the median filter centered on the jth value of θ, the window radius r is the number of samples included in the window on either side of θ_j, and *Med* is the median filter than runs from $i = j - r$ to $i = j + r$, which includes the value at $i = j$. The background level is then estimated to be

$$\mu(\nu_l, t_k) = \text{Med}_{m=l-r_3}^{l+r_3} \left(\frac{1}{2r_2 + 1} \sum_{i=k-r_2}^{k+r_2} \text{Med}_{j=i-r_1}^{i+r_1} x(\nu_m, t_j) \right), \tag{3.3}$$

where "*Med*" is the median filter and r_1, r_2, and r_3 are window radii for the operations in steps 1, 2, and 3, respectively. The running average over time is implemented as a method of

smoothing over short time variabilities. Typical values for the size of the averaging window, r_2, range from 2 to 10 min. In contrast, the median filters, while often also used for smoothing purposes, are used here in attempt to remove narrow band and transient outliers. Therefore, for r_1 and r_3 we choose the shortest possible window sizes. The goal is to remove or suppress outliers while retaining the integrity of the background. For this analysis a window value of 3 was used for both running median filters. Figure 3.5 shows a comparison between a spectrum that has been averaged over time and the corresponding background that has been estimated according to Equation 3.3. Most of the narrow band features are either completely gone or significantly dampened in the estimated background.

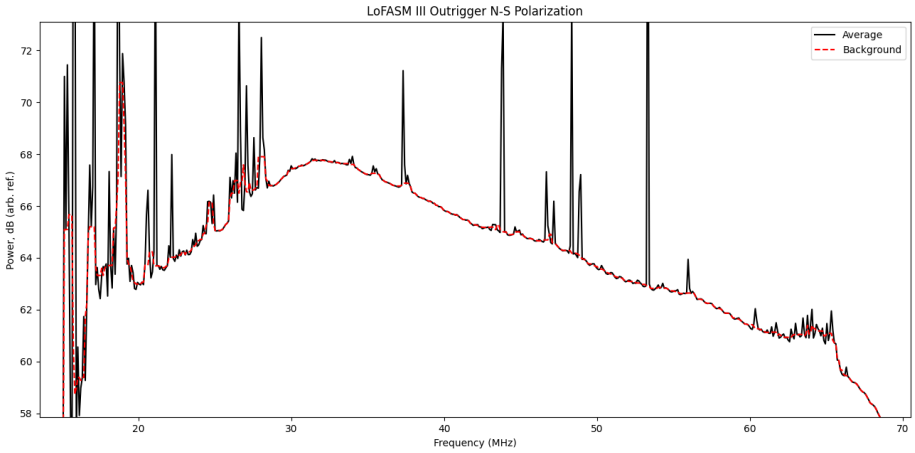

Figure 3.5: Time-averaged LoFASM spectrum and estimation of background, as per Equation 3.3.

Variations from the mean for each frequency band can be obtained by subtracting or removing the mean (e.g. the background level) from each sample in the spectrum:

$$y(\nu, t) = x(\nu, t) - \mu, \tag{3.4}$$

where μ is the estimated background from Equation 3.3 computed over the entire data set, $x(\nu, t)$ is the raw PSD value at frequency ν and time t, and $y(\nu, t)$ is the zero mean value for the same. Figure 3.6 shows an example of this principle being applied to LoFASM data.

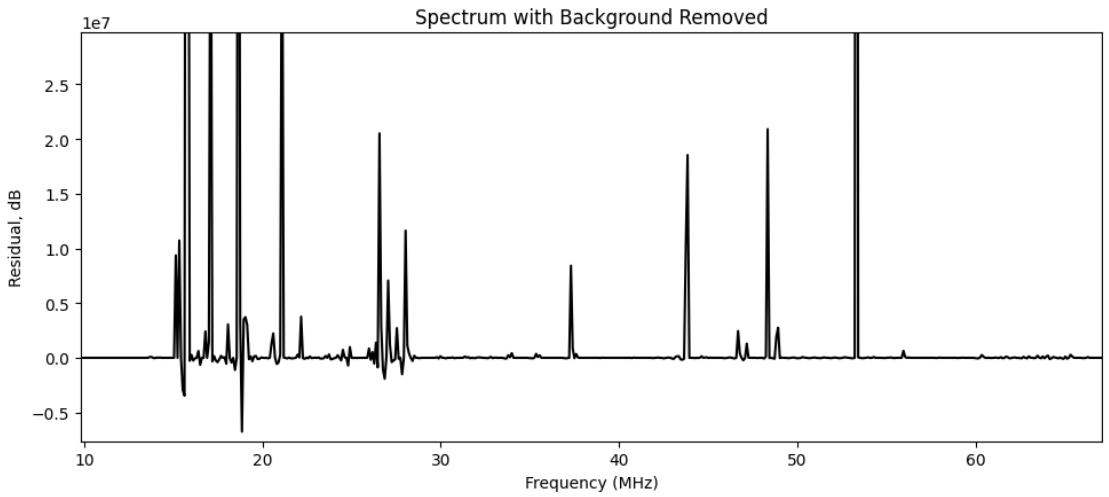

Figure 3.6: LoFASM spectrum sample with the background removed as per Equation 3.4. All remaining fluctuations are due to noise or transient signals present in the data.

It is helpful to represent deviations from the mean in terms of multiples of the standard deviation. The standard score, or z-score, is used for this purpose. The z-score is given by

$$z(\nu_i, t_j) = \frac{x(\nu_i, t_j) - \mu}{\sigma}, \tag{3.5}$$

where $z(\nu_i, t_j)$ and $x(\nu_i, t_j)$ are the z-score and PSD value at frequency ν_i and time t_j, respectively, μ is the sample mean, and σ is the standard deviation.

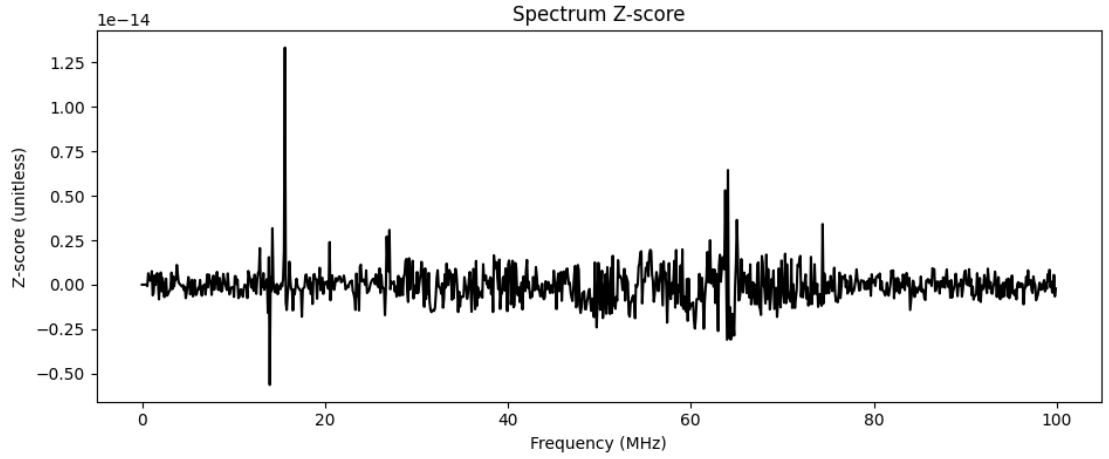

Figure 3.7: Z-score of a single spectrum of LoFASM Data, generated as per Equation 3.5.

All subsequent analyses are performed using this z-score. Any signal that is present in the data, namely $z(\nu_i, t_j)$, that is not zero mean is considered to be an artifact. Figure 3.8 shows a data sample in which the presence of such artifacts is clear.

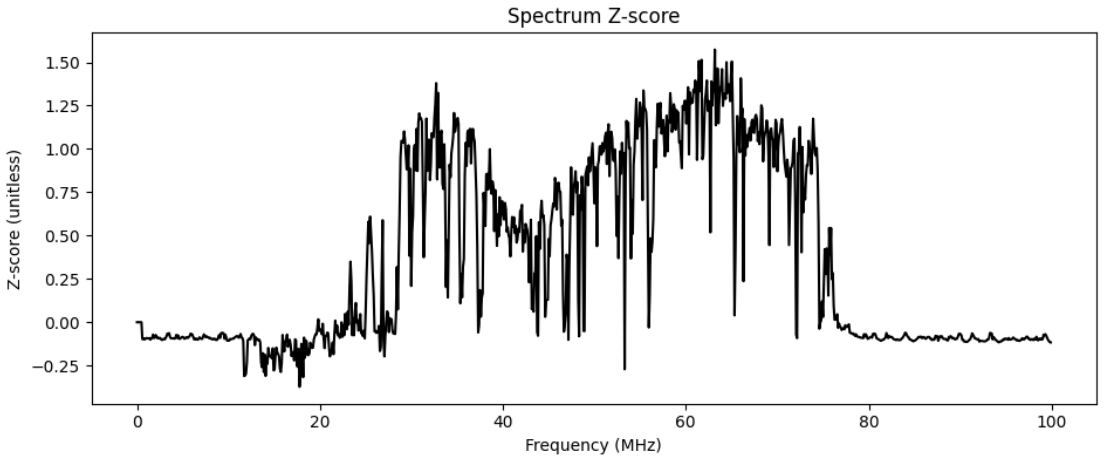

Figure 3.8: Z-score of a single spectral sample of LoFASM Data, generated as per Equation 3.5. The artifacts from ∼20-75 MHz are from the Galaxy. This data is a horizontal slice taken from the spectrogram shown in Figure 3.9.

When applying Equation 3.5 to all time samples, t_i, a spectrogram can be produced to show the evolution of the signal artifacts over time. Figure 3.9 shows such a spectrogram, in which the Galaxy can be seen as it passes over LoFASM III. The conic narrowing in the response at higher frequencies is due to the fact that the LoFASM beam width is narrower at higher frequencies and broader at lower frequencies.

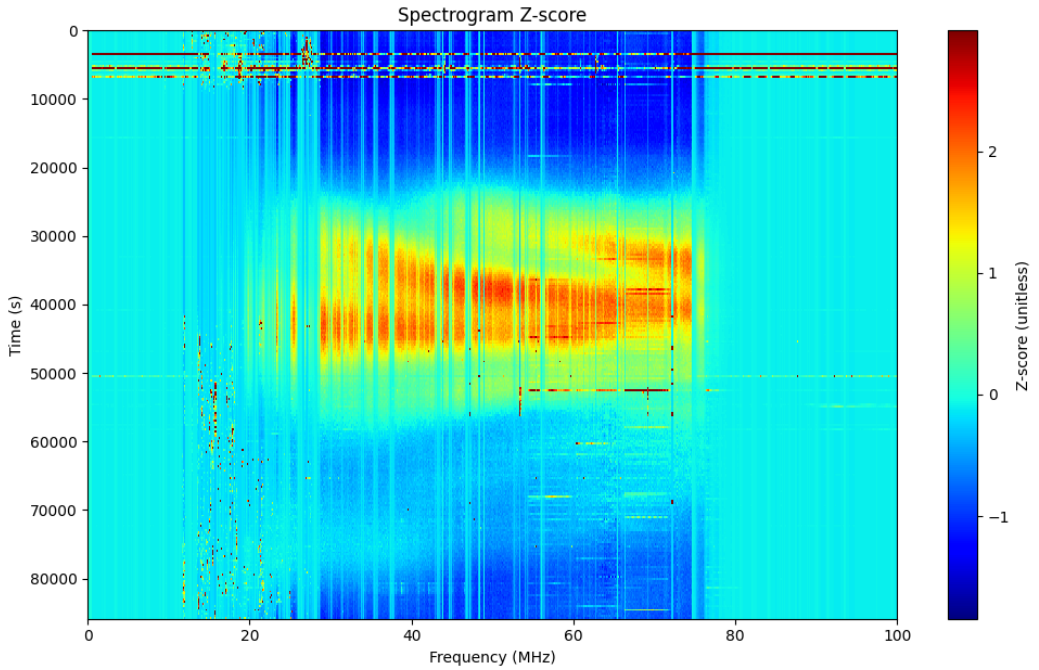

Figure 3.9: Z-score spectrogram of a 24 hr LoFASM dataset. The bright red artifact at the center is due to the Galaxy passing overhead. The data was recorded using a single linearly polarized channel at LoFASM III. The regions outside of 15-75 MHz are filtered out by the analog signal chain and therefore exhibit very little activity.

The methods employed in this analysis were deemed sufficient to generate clean spectrograms and extract features from the Galaxy and other sources. However, they do not necessarily represent the optimal approach to cleaning the LoFASM data products. The development of analysis routines for LoFASM data is an ongoing endeavor. The use of more rigorous filters, RFI mitigation techniques, spectral whitening methods, and pattern matching may very well prove to be more effective at extracting elusive signatures in future studies.

3.2 Interferometry Using the Main LoFASM Array and an Outrigger Antenna

Interferometry is a technique that allows for multiple independent antennas separated by some distance to be used together as a single instrument by electronically (either in analog

or digitally) steering a synthesized aperture. This is done by correcting for the temporal delays associated with the fact that any wave incident on the antennas in the telescope will exhibit a different time of arrival that is unique to each element and depends on the direction of the source of emission (see Figure 3.10). The only time that the time of arrival of a signal will be the same for all elements in a group of antennas forming two-dimensional baselines is when the source is directly overhead (or somehow directly below, a situation that is mathematically possible but practically unlikely.) In the case of an interferometer that consists only of two antennas separated by some fixed distance, and thus forming a single one dimensional baseline between them, the directions with equivalent delay form a cone with a specified opening angle and the baseline as its axis.

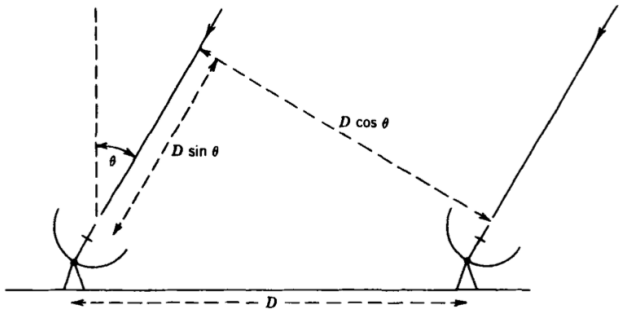

Figure 3.10: Geometry of an elementary interferometer. $\mathbb{B}$ is the interferometer baseline and θ is the angle between zenith and a point source. Credit: Thompson et al. [2017]

The advantages that an interferometric system has over a single dish system are abound. Interferometers provide much longer baselines, and thus higher angular resolutions than possible with a single dish receiver. A telescope's baseline, whether characterized by the diameter of a collecting dish or the distance between a pair or group of antennas from one another, is the single biggest contributing factor when it comes to determining the achievable angular resolution. Single dish systems can only be feasibly built to be so large. At the time of this writing, the largest fully steerable single dish radio telescope on the planet is the Green Bank Telescope in Green Bank, West Virginia with a collecting diameter of 100 m (see Figure 3.11). Though not fully steerable, the 500 m diameter FAST radio telescope is

the largest single dish collecting area on the planet (see Figure 1.4). In contrast, the VLA in New Mexico, which is an interferometer consisting of 27 independent 25 m fully steerable dishes, has a maximum baseline of 36 km, which is practically two orders of magnitude larger than that of FAST. Additionally, the Very Long Baseline Interferometer (VLBI) has a baseline that spans entire continents. Since these instruments operate at wavelengths that are miniscule compared to their baselines, they benefit from superior angular resolutions.

Figure 3.11: The Robert C. Byrd Green Bank Telescope (GBT). With a 100 m diameter collecting area, the GBT is the world's largest fully steerable radio telescope. Credit: Green Bank Observatory

At long wavelengths (low frequencies), achieving similarly high angular resolutions comes with a new set of challenges. To begin with, since the wavelengths are much longer (on the order of 10 m) baseline distances have to be much larger to compensate for the ratio in Equation 1.1. Moreover, the ionosphere at these frequencies is much more turbulent, which causes issues when antennas are placed far enough apart that they are no longer looking through the exact same patch of sky. The characterization of and correction for ionospheric disturbances due to propagating plasma density perturbations that cause issues below 100 MHz is an active area of research. (Obenberger et al. [2019])

The placement of an outrigger at each of the LoFASM stations allows for interferometry to be performed by treating the main grouping of antennas as a single element and the lone outrigger antenna as the other in a two element interferometer. Since the array-outrigger systems are oriented (mostly) East-West (see Table 2.2), we are able to easily detect stronger sources and localize them more accurately in Right Ascension than in Declination. As bright point sources rise above the horizon towards the East and move overhead the voltage as a function of time in the interferometer response, which is obtained from the multiplication of the outputs of the main array and the outrigger, will contain a corresponding interference pattern that manifests in the form of ripples in the integrated cross-power data products recorded by the LoFASM Spectrometer (see Figure 3.12). The spacing between the oscillations of the "ripples" in these interference patterns will vary as a function of geometric delay, which drifts as the source passes overhead. The delay is at a maximum when the source is rising and setting and at a minimum when its altitude is at a maximum. The response of the two element interferometer from a single point source, in the case that the signals received from both elements are entirely identical in finite bandwidths and electrical bandpass characteristics and only differ by the geometric time delay, the output from the correlator can be described as the cross correlation of the two signals:

$$r(\tau) = \lim_{T\to\infty} \frac{1}{2T} \int_{-T}^{T} V_1(t) V_2^*(t-\tau) dt, \tag{3.6}$$

where $2T$ is the total integration time and τ is the lag between the two signals. The value of τ will follow $\frac{D}{c} \sin\theta_0$, where we take the phase reference position, denoted by θ_0, to be measured from zenith.

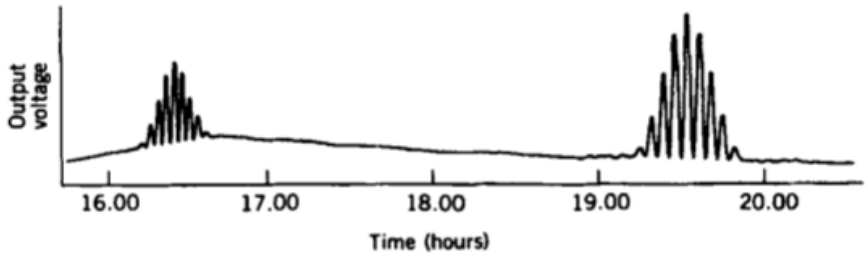

Figure 3.12: Voltage record from an interferometer with East-West antenna spacing. The source at the left is Cygnus A and the one at the right Cassiopeia A. The increase in level near Cygnus A results from the galactic background radiation, which is concentrated toward the plane of our Galaxy but is completely resolved by the interferometer fringes. Credit: Thompson et al. [2017]

When analyzing data taken while a station is operating in interferometer mode, meaning that at least one of the signals from a station's outrigger antenna is being digitized and correlated with those from the main array, these principles can be applied to determine the expected geometric time delay between the elements of a station for any point on the sky.

The pipeline of analysis for spectrometer data products begins with time samples of the PSD over some duration of time, typically long enough for a source of interest to rise and set. Owing to its large wide field view on the sky this will be on the order of 3 hours for a high altitude source for a LoFASM station. Data is first inspected visually on an individual basis to determine whether it will be experimentally useful and of good enough quality for a measurement to be made. Figure 3.13 depicts an example of a relatively clean stretch of data taken at LoFASM III in interferometer mode. Included in that snapshot is evidence of a multitude of different artifacts presenting themselves in the spectrum. The most obvious is probably the presence of the fringe patterns produced by Cygnus A and Cassiopeia A, two of the brightest radio sources in the sky in the LoFASM frequency band. As expected, we observe the spacing between the fringes drift over time as each source transits the viewable region of the sky, changing the resultant geometric delay that gives us our interference patterns. Also present in this image are discrete sets of dim narrow band vertical lines that span the entire data set. These dim lines are the result of subtracting various bright lines

from the image during the cleaning process.

We explored the efficacy of using a combination of running median and minimum filters in conjunction with a running average over time. Extremely bright signals present in certain frequency bands skewed the scaling of those bins so that they appear dimmer than their neighbors. This can be mitigated by limiting the temporal window over which the running filters are applied. The importance of having a robust cleaning methodology can not be overstated. It will either make or break the entire analysis pipeline. Additionally, between frequency bins 400-520 (corresponding roughly to 55-65 MHz) are short lived narrow band signals that are considerably louder than the background. Due to their strict narrow band nature and transient properties, we can conclude that these are most likely caused by terrestrial RFI. My initial guess is that they are likely caused by television transmissions. Another example of these signals is shown in Figure 3.14.

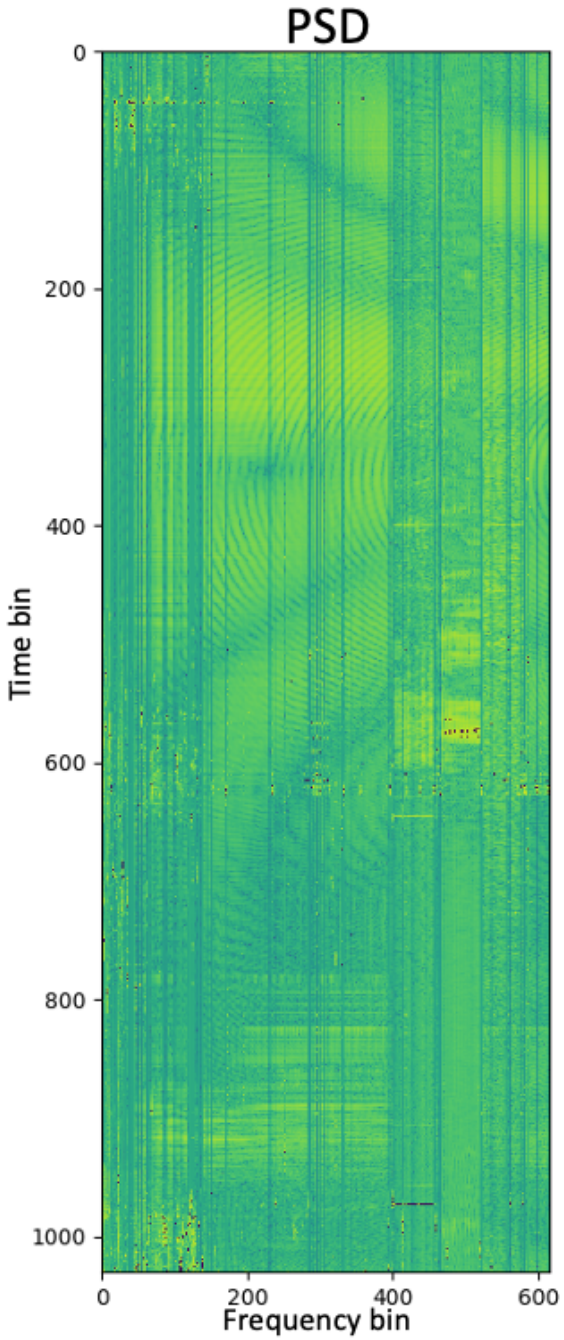

Figure 3.13: Time averaged 24 hour cross-power spectral density between the inner ring of the LoFASM array and the outrigger taken at LoFASM III in the North-South polarization on MJD59039 from 15-75 MHz. The size of each time bin is 83.4 s.

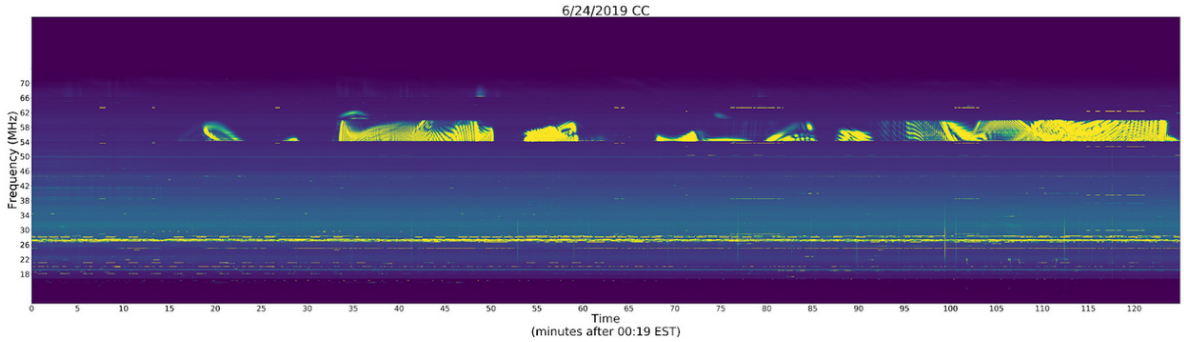

Figure 3.14: Data taken from a single ring at LoFASM III in 2019. The activity occurring in the 55-60 MHz band is estimated to be anthropogenic in origin, likely from television broadcasts.

Due to the high degree of inherent variability in the 10-88 MHz band and fluctuations in the responses in the plethora of active components in the analog signal chain, identifying good stretches of data has proven to be an immense task in and of itself. However, the LoFASM telescope stations are not alone in this category. The development of algorithms based on heuristic statistic measurements, machine learning techniques, as well as knowledge refined over decades in the field of communications is an active area of research. The problem of relying on post-processing methods to clean data and mitigate the effects of RFI after data has been recorded is amplified at lower frequencies. This is partly due to the natural rise in noise temperature from the Galactic background. In addition, the fact that the sub 100 MHz range of radio frequencies hosted the entirety of the evolution of RF based technologies for during their infancy in the late 19th and early 20th centuries does not help the RFI problem. This is another reason that, when fully realized, the synthesized LoFASM beam holds the potential to drastically improve the quality of *wide band* data collected at low frequencies. This is because the prospect of rejecting unwanted RFI signals *in analog* means that their detrimental effects will not need to be cleaned up in the post-processing stages. At 20 MHz, 40 dB of attenuation of the horizon is expected to drastically lower to barrier to conducting scientifically interesting observations in a region of the spectrum that has been otherwise effectively inaccessible to radio astronomers using ground based radio telescopes since shortly after World War II. On the other hand, the 10-15 dB of attenuation

expected between 30 MHz and 60 MHz will play an important role in reducing the negative impacts from local terrestrial sources of RFI at those frequencies. The RFI discussed earlier shown in Figure 3.13 and Figure 3.14 are examples of cases where RFI rendered large swaths of data practically useless for observing astrophysical sources. Figure 3.13 also demonstrates that variabilities in the antenna response can occur over a wide range of timescales, from a few milliseconds to several hours, for a number of reasons either internal (e.g. self-generated system noise) or external (e.g. natural or anthropogenic RF detected by the instrument). In many cases this results in a much more highly polluted PSD (e.g. Figure 3.15, left).

When performing interferometry using a LoFASM station, we again use the Wiener-Khinchin relationship to advantage. We know that the cross power spectral data recorded by the LoFASM Spectrometer can be described in the form of Equation 2.13. That is, by taking the inverse Fourier Transform of $S(\nu)$, we get the correlation as a function of delay, $r(\tau)$, in the form of Equation 3.6. Thus, we are able to measure this delay over time (see Figure 3.15, right).

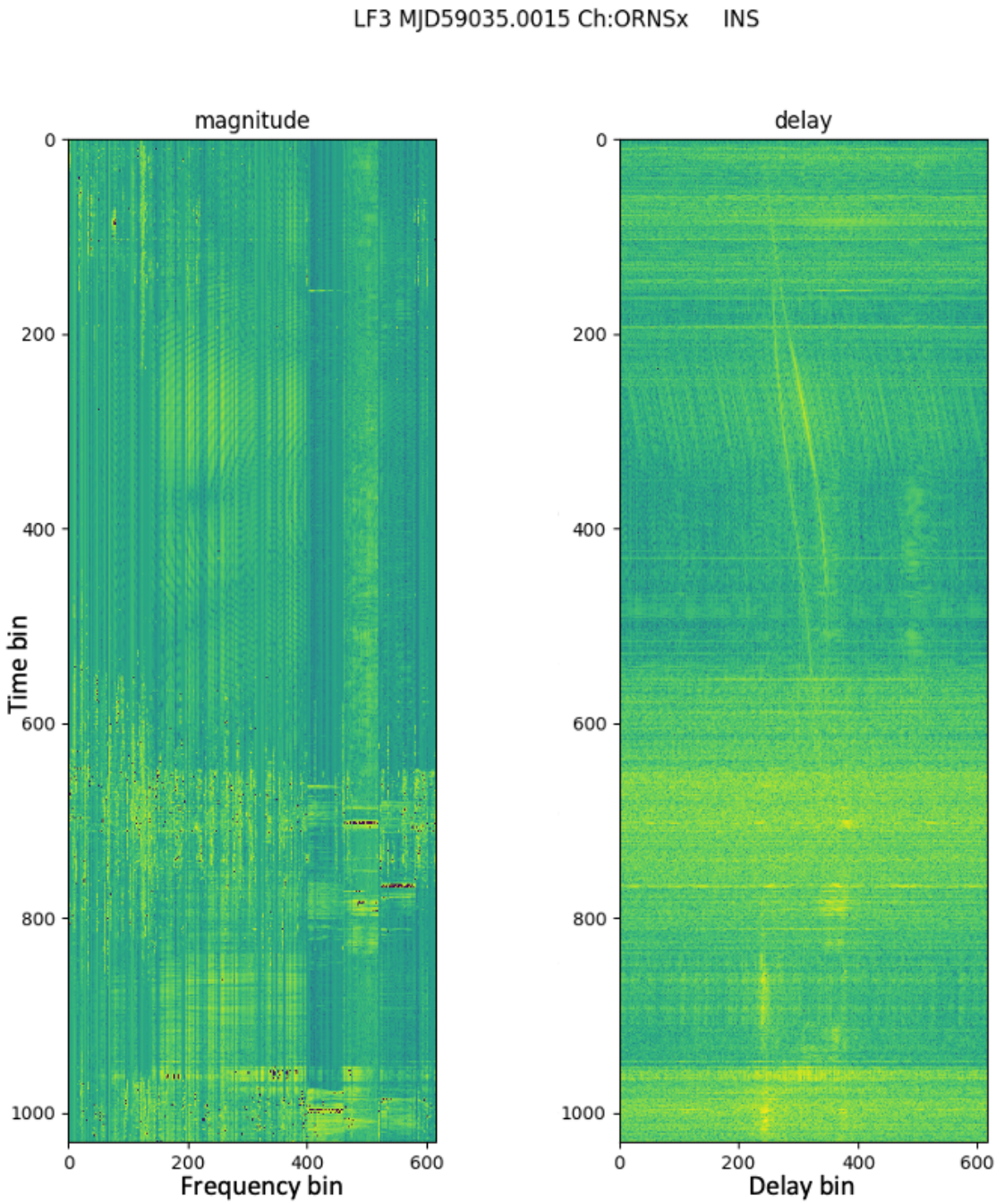

Figure 3.15: Spectrogram (left) and corresponding delay plot (right) from LoFASM III spanning a 24 hr period. The size of each time bin is 83.4 s. The frequency range in the spectrogram spans from 15-75 MHz with a step size of 97.6 kHz. The x-axis on the delay plot represents measured time delay, centered at 0 s of delay at bin 308. The delay bin step size is 16.6 ns. The delay axis spans $\pm 5.1\,\mu$s.

This can be useful for a number of reasons. Of primary interest is the use of interferometry

to observe bright radio sources on the sky that can be used as standard candles to assist in calibrating the power received by the LoFASM array. However, in order to be able to calibrate the instrument, the clean, well-behaved datasets are preferred, if not required. The RFI pollution depicted in Figure 3.15 makes resolving even the brightest sources on the sky difficult. Among the set of software tools developed specifically for analyzing LoFASM data, is a set of data cleaning tools (still under development) that help mitigate these effects. Figure 3.16 shows the result of the same dataset from LoFASM III taken on MJD59035 after the application of cleaning and rescaling routines. The rescaling scheme, which we applied to the data in the PSD before computing the inverse Fourier Transform, was taken from Muhammet et al. [2019]:

$$S(f_i, t_k) = \frac{S(f_i, t_k)}{\sqrt{|S(f_i, t_k)|^2 + \mu}}, \tag{3.7}$$

where $S(f_i, t_k)$ is the complex valued cross-power spectrum and μ is a dataset specific real-valued corrective scaling factor. Using Equation 3.7 to re-scale the PSD greatly improved the quality of $r(\tau)$ in our datasets. (see Figure 3.16).

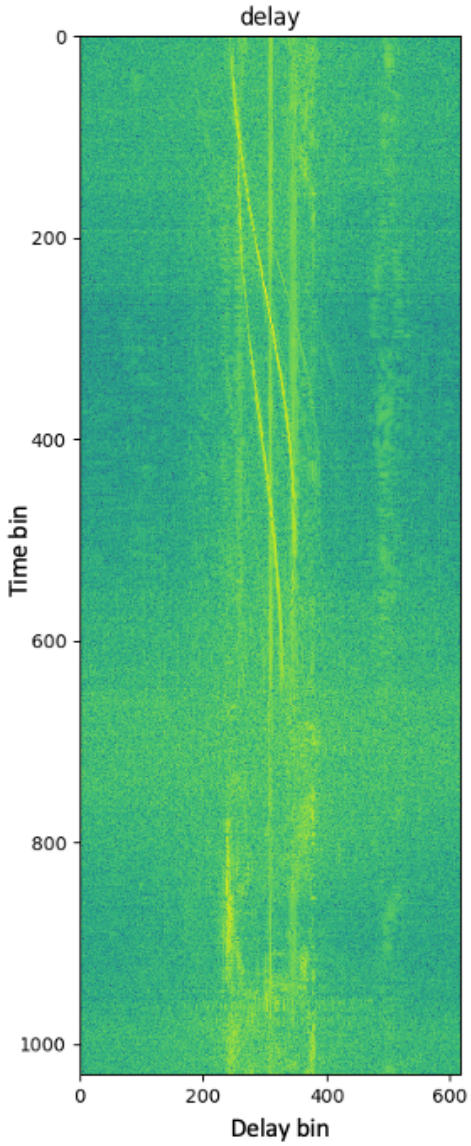

Figure 3.16: LoFASM III PSD data after applying Equation 3.7 to bring out some otherwise obscured features in LoFASM data. The time axis spans 24 hours with a step size of 83.4 s. The x-axis represents time delay with a step size of 16.6 ns. The zero delay bin is located at the center (bin number 308). The delay axis spans $\pm 5.1\,\mu$s.

3.2.1 Solving for the Geometric Delay

The procedure for taking the output of $r(\tau, t)$ as it presents itself in the LoFASM datasets and using it to study the system response to a point source is a multi-step process. The remainder of this section will focus on describing the methods that were used and discussing

their results. Before accurately calculating and accounting for the delays that affect the telescope's response, we first need to determine the local mean sidereal time (LST) and source-dependent local hour angle (HA), both of which depend on time, associated with each time sample, t_i. We will start by defining some of these terms in sufficient detail and then discuss their implementation as part of this analysis.

Calculating the geometric time delay that is expected from any given source on the sky requires knowing where the source is with respect to the telescope at all times during its observation. Specifically, for the case of an interferometer, we need to be able to calculate the projection of the instrument's baseline on the sky in the direction of a unit vector that points towards the source. This quantity must then be tracked over time as the source rises and sets due to the rotation of the Earth. To do this we will use the equatorial coordinate system, the most widely used celestial coordinate system. The equatorial coordinate system is tightly based on the geographic system. They are both Earth-centric, meaning that they are defined by placing Earth's center at the origin. In short, the equatorial coordinate system is the projection of the commonly used geographic coordinates, latitude l, and longitude L, onto the celestial sphere, an imaginary sphere centered on Earth on which all celestial sources can be projected. The coordinates used in the equatorial system are analogous to those used geographically. Lines of latitude simply become *declination*, δ, and the longitudinal coordinates similarly become equivalent lines of *right ascension*, α. However, whereas the declination ranges from $-90^\circ < \delta < 90^\circ$, is measured in degrees, arcminutes, and arcseconds, as the angle subtended from the equator, the right ascension is typically measured in hours, minutes, and seconds as measured from where the celestial intersects the ecliptic (i.e. the vernal equinox) and ranges from $0\text{h} < \alpha < 24\text{h}$. The movement of the celestial sphere is often measured by using a metric known as the sidereal time. The sidereal time corresponding to any place on the earth, its local sidereal time (LST), is equal to the right ascension of local meridian projected onto the celestial sphere. The angle subtended between the local

meridian and the right ascension of a point on the celestial sphere is known as the local hour angle (LHA) of an object located at that point on the sky. That is,

$$\mathrm{LHA} = \mathrm{LST} - \alpha, \tag{3.8}$$

or by extension,

$$\mathrm{LHA} = \mathrm{GST} + \lambda - \alpha, \tag{3.9}$$

where α is the right ascension of the object in question, GST is the sidereal time of Greenwich, and λ is the longitude of the observer.

Calculating τ_g, the geometric time delay due to a emissions from a point source incident on an interferometer requires calculating

$$\tau_g = \frac{\hat{\boldsymbol{s}} \cdot \boldsymbol{B}}{c} \tag{3.10}$$

and thus

$$\tau_g = \frac{B \sin(\theta)}{c}, \tag{3.11}$$

where $\hat{\boldsymbol{s}}$ is a unit vector pointing in the direction of the source, $\boldsymbol{b}$ is the baseline between a pair of antennas, θ is the angle between the direction of the source on the sky and the baseline, and c is the speed of light. As shown, this quantity is independent of wavelength. Due to constraints when installing each of the LoFASM arrays, the LoFASM-outrigger baselines are not exactly East-West aligned (see Table 2.2). To deal with this, we must take into account the angular separation between the baseline of the interferometer and the East-West direction. For a LoFASM station, τ_g then takes the form of

$$\tau_g = \frac{B}{c} \left(\cos(\delta) \sin(\mathrm{LHA}) \cos(\rho) + \sin(\rho)(\sin(\delta) \cos(\mathrm{LAT}) - \cos(\delta) \sin(\mathrm{LAT}) \cos(\mathrm{LHA})) \right), \tag{3.12}$$

where τ_g, measured in seconds, is the geometric delay due to placement of the elements in the two element interferometer, B, measured in meters, in the baseline of separating the main LoFASM array from the outrigger antenna, δ is the source's declination, LHA is the local hour angle subtended between the LST of the observatory and the right ascension of the source, ρ is the angle between the direction of the baseline and the East-West direction, and LAT is the latitude at which the observatory is located. The algorithmic procedure solving for τ_g starting from the PSD recorded by the backend is shown in Algorithm 1.

Data: timestamps for each sample of the power spectral density
Result: geometric time delay between the outrigger antenna and the main array of a LoFASM station
initialization;
for *each MJD timestamp* **do**
    use MJD and latitude of observer to calculate LST;
    calculate LHA = LST - RA;
    calculate τ_g;
    shift delay vector by τ_g to correct for instrumental delay;
end

Algorithm 1: Procedure for calculating geometric time delay from a LoFASM PSD file

Once τ_g is known as a function of time for a particular source we can get the true expected delay by then correcting for instrumental delay. Instrumental delay, τ_i, is any additional delay that introduced into the interferometer system due to cabling effects or individual antenna gains. The total time delay associated with the system's response to a source, τ, is

$$\tau = \tau_g + \tau_i. \tag{3.13}$$

The value of τ_i is specific to each LoFASM station. During the installation phase, significant effort goes into ensuring that all signal-carrying cables are phase matched, meaning that their frequency-dependent electrical length is carefully measured and the cables are cut such that the electrical lengths differ by as little as possible at the highest frequencies of interest. However, due to human error it is not possible to get the cable lengths to align perfectly. In

the cases of LoFASM III and LoFASM IV, I placed upper limits on the value of instrumental delay. These values are listed in Table 3.3.

Station	τ_i
LoFASM III	16.62 ns
LoFASM IV	58 ns

Table 3.3: Upper limits on the instrumental cable delays measured experimentally at LoFASMs III & IV.

As discussed in this section, using $\tau(t)$ to determine the delay track for a source allows us to extract the interferometer's response to source from the data. Figure 3.17 shows the calculated τ overlaid with data taken at LoFASM III in the presence of a number of point sources. Clearly dominating the telescope response are emissions from Cgynus A and Cassiopeia A. Only the values of $\tau(g)$ that correspond to times where each source is above the horizontal are plotted. Due to its high declination, Cassiopeia A is circumpolar, meaning that its altitude, the angle subtended by the source's direction from the horizontal, is always above 0°. However, from inspecting the data it is clear that the source sets and rises periodically. This can partly be attributed to the beam pattern of the LoFASM array + outrigger system. It's also worth recalling here that LoFASM III is located at the Green Bank Observatory in Green Bank, West Virginia, which is nested inside the Allegheny Mountain Range. Due to the surrounding terrain obstructing the view of the horizon from the LoFASM station, it is to be expected that Cassiopeia A sets and rises into and out of view on sidereal timescales. On the other hand, the second brightest source, Cygnus A, is not circumpolar and very clearly sets accordingly. Even so, it is observed to set earlier and rise later than it would if the horizon were visible to the telescope. In addition to Cygnus A and Cassiopeia A, a number of other point sources are clearly visible in the correlation data. The prominent presence of Cygnus A and Cassiopeia A, in addition to that of the various other point sources, demonstrates LoFASM's potential as a scientific instrument for radio astronomy.

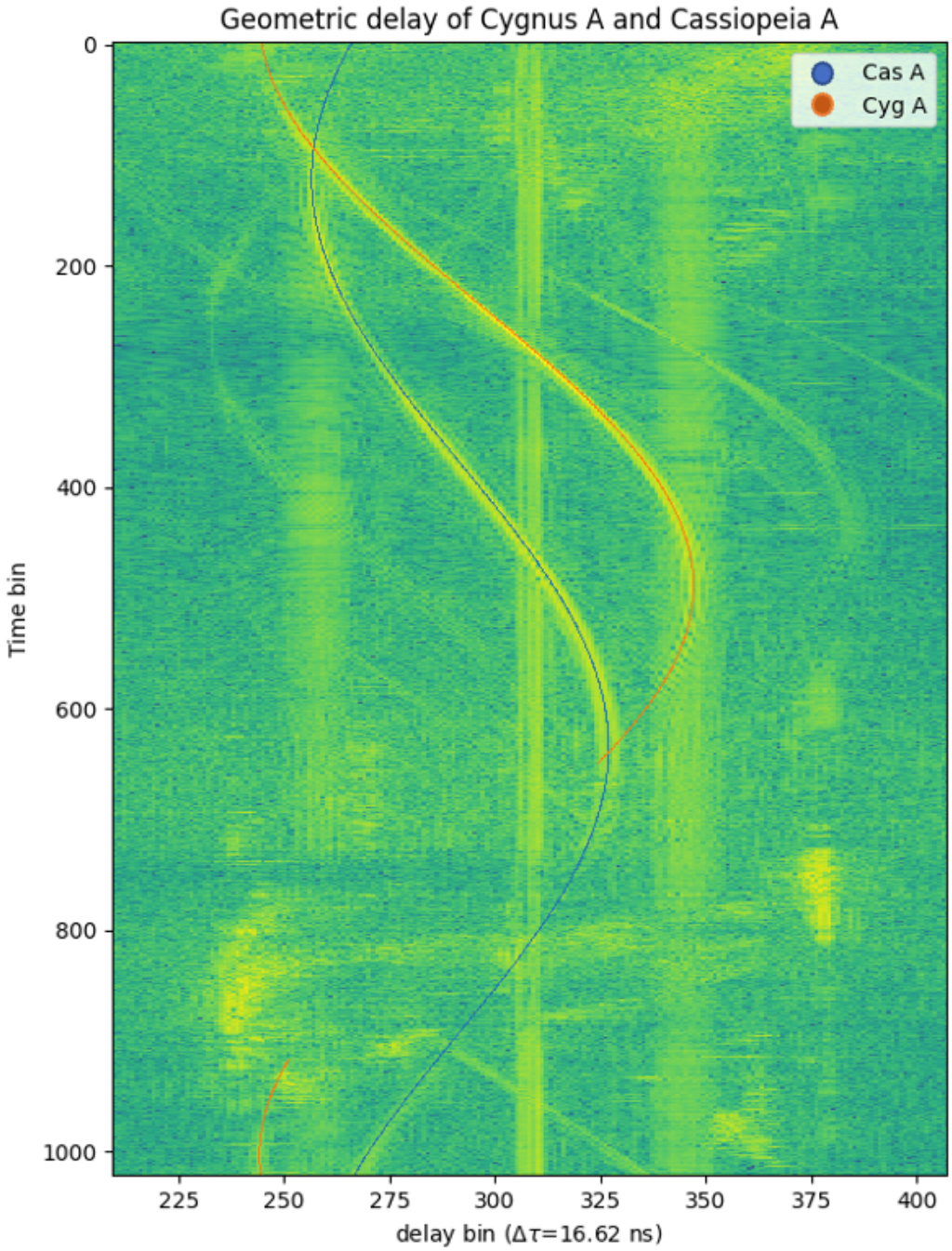

Figure 3.17: Delay plot with predicted delay tracks from the two brightest sources, Cygnus A and Cassiopeia A, overlaid. The time axis spans 24 hours with a step size of 83.4 s. The x-axis represents time delay with a step size of 16.6 ns. The zero delay bin is located at the center (bin number 308).

3.2.2 Producing Maps of the Sky using LoFASM as an Interferometer

The total system response from a source can be calculated by summing along the values $r_i(\tau)$ for each time t_i. Algorithmically, this can be done in two ways. The first is simply to sum the values and along the delay tracks shown in Figure 3.17. The second is to correct for τ by introducing a phase shift to each time sample. Explicitly, this means computing

$$P(\alpha, \delta) = \sum_{n=0}^{N-1} \sum_{m=0}^{M-1} V_{ring}(\nu_n, t_m)^* V_{outrigger}(\nu_n, t_m) e^{i2\pi\nu_n\tau_m(\alpha,\delta)}, \tag{3.14}$$

where $P(\alpha, \delta)$ is the amplitude of the averaged cross power as a function of right ascension and declination, n is the frequency bin index, m is the time sample index, V_{ring} is the PSD from one of the rings in the main array, $V_{outrigger}$ is the same for the outrigger signal, ν_n is n^{th} frequency, t_m is the m^{th} time in seconds, and τ_m is the expected total delay $(\tau_g + \tau_i)$ at time t_m. Since τ_i is a characteristic of the telescope and does not change with time, only τ_g drifts over time as the local hour angle, $\mathrm{LHA} = \mathrm{LST} - \alpha$ changes due to the Earth's rotation.

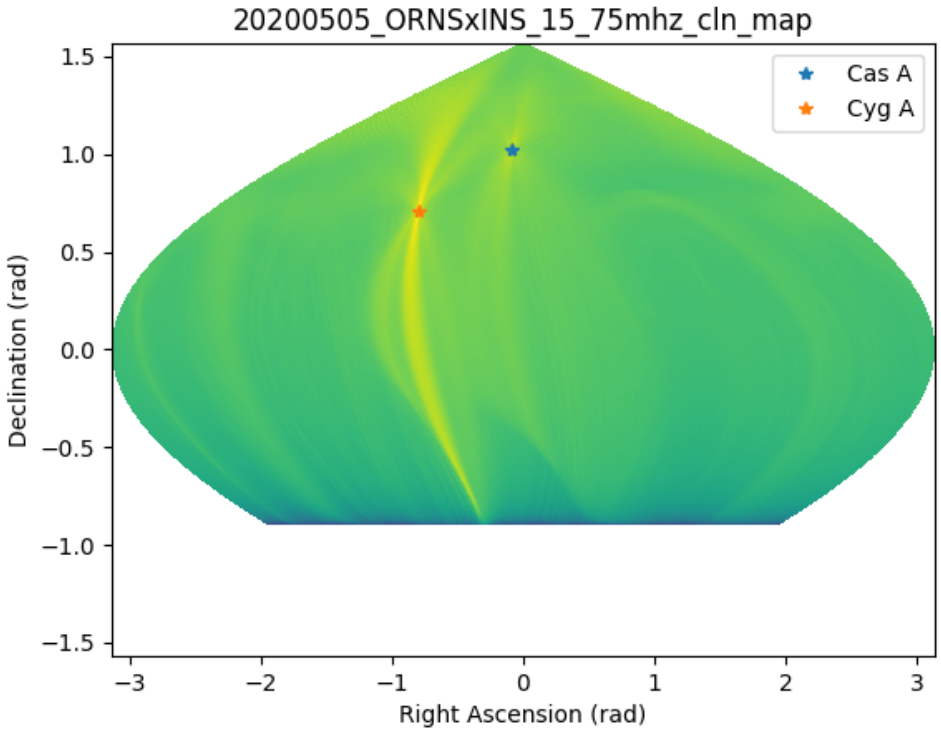

Figure 3.18: Skymap produced from data taken over the course of 24 hours showing the CygA, CasA, and other sources. Such a map could benefit from additional cleaning and imaging analysis, specifically applying a CLEAN algorithm would likely help bring out some of the radio sources in the background.

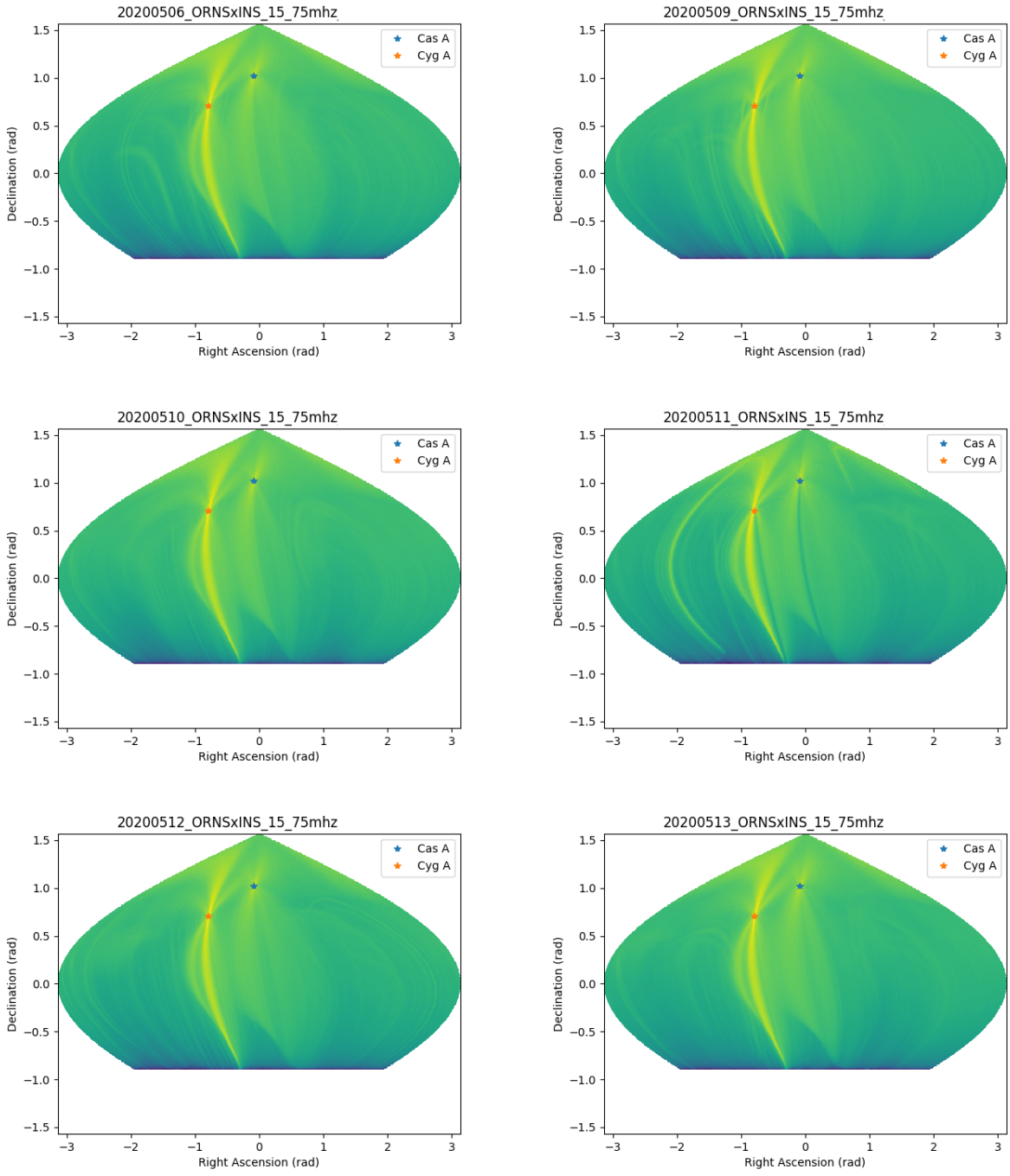

Figure 3.19: Skymaps generated by using LoFASM III in interferometer mode.

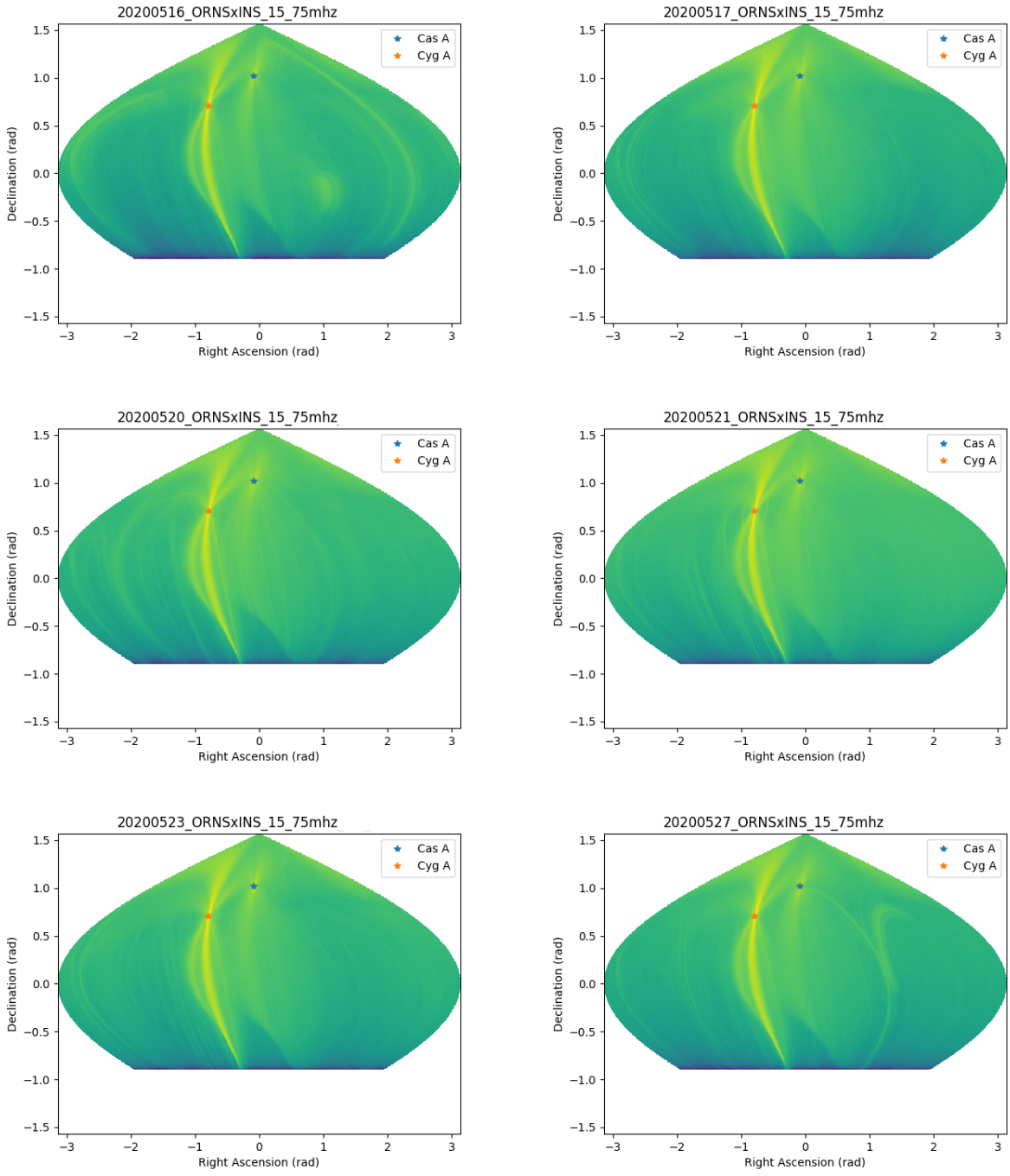

Figure 3.20: Skymaps generated by using LoFASM III in interferometer mode.

We then calculate $P(\alpha, \delta) \sin \varphi$, where φ is the altitude of the direction (α,δ), for all right ascensions and declinations in the range $\text{LAT} - \frac{\pi}{2} < \delta < \text{LAT} + \frac{\pi}{2}$, with the obvious

maximum and minimum of $[\frac{-\pi}{2}, \frac{\pi}{2}]$ imposed on the values of δ, to produce a map of the sky. Figure 3.18 depicts the measured $P \sin\varphi$ for this range plotted onto a sinusoidal projection of the sky. Additional sky maps are provided in Figure 3.19 and Figure 3.20. The two brightest sources identified earlier in the output of the correlation function are clearly visible. The vertical striping spreading from each source can be attributed to the telescope's point spread function, which is a consequence of the instrument's response to discrete signals. Power from nearby sources are being summed over each other. That is, the sum in Equation 3.14 for sources near each other in declination will overlap. This can be corrected by deconvolving the telescope point spread function for the brightest source in the dataset. One popular method of deconvolution that is often used in Radio Astronomy is called the CLEAN algorithm (Högbom [1974]).

3.2.3 The Visibility Function

The delay track associated with a particular source, such as those that appear in Figure 3.17, represents the interferometer response to that source and is called the visibility function. The visibility function for a source located at direction $\hat{\boldsymbol{s}}$ for a two element interferometer, such as LoFASM, is given as

$$R(\boldsymbol{B}) = \int\int_{\Omega} A(\boldsymbol{s}) I_\nu(\boldsymbol{s}) \exp\left[\mathrm{i}2\pi\nu\left(\frac{1}{c}\boldsymbol{B}\cdot\boldsymbol{s} - \tau_i\right)\right] \mathrm{d}\Omega\mathrm{d}\nu, \tag{3.15}$$

where $A(\boldsymbol{s})$ is the element power pattern and $I_\nu(\boldsymbol{s})$ is the frequency dependent source intensity, both in the direction $\hat{\boldsymbol{s}}$. The LoFASM baseline is (very nearly) aligned with the East-West direction, so the visibility function can be reduced to a function of a single angle, θ:

$$R(\theta) = \int\int A(\theta) I_\nu(\theta) \exp\left[\mathrm{i}2\pi\left(\frac{1}{c}\boldsymbol{B}\cdot\theta\right)\right] \mathrm{d}\theta\mathrm{d}\nu. \tag{3.16}$$

As the direction to the source changes over time due to the rotation of the Earth, oscil-

lations will be appear in the output of the visibility function. These oscillations are called *fringes*. Analysis of the fringes from an object inform as to whether or not that object is well resolved by the interferometer. Figure 3.21 shows the fringes measured from Cygnus A at LoFASM III. The relative amplitude of the minima and the maxima of the fringes is used to determine how well an object is resolved. This amplitude, known as the fringe visibility, is a value that can range from 0-1 and is defined as $V = (I_{\max} - I_{\min})/(I_{\max} + I_{\min})$, where $I_{\max}$ and $I_{\min}$ are the intensities of the maxima and minima, respectively. The object under observation is said to be "resolved" when the fringe visibility is measurably less than 1 (Thompson et al. [2017]). With a fringe visibility of ~ 0.45, Cygnus A is partially resolved by LoFASM III.

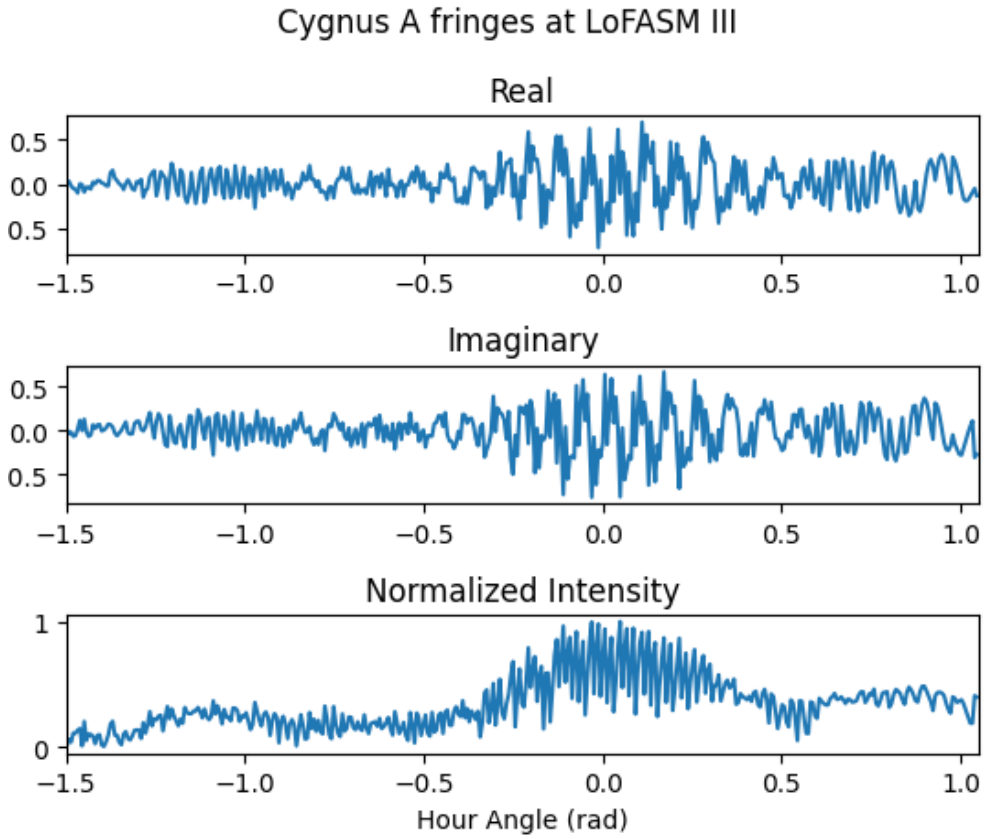

Figure 3.21: Cygnus A fringes as seen by LoFASM III operating in interferometer mode. The presence of the observed fringes indicates that Cygnus A is not fully resolved by the instrument. However, with a fringe visibility of ~ 0.45, Cygnus A is partially resolved.

Additionally, LoFASM does not operate on an infinite bandwidth. The bandwidth in the data analyzed this section has been constrained to 15-75 MHz, giving us a bandwidth, $\Delta\nu \approx 60\,\text{MHz}$. As previously discussed, we know that τ_g is independent of frequency. However, the instrumental delay introduced in Equation 3.13, t_i, is typically frequency dependent. This frequency dependence will be due to the electrical and wave guide properties of the cables being used in the transmission lines connecting the elements of the array to the system. The phase shifts introduced by τ_i will directly affect the visibility function.

The phase shift due to instrumental delay can be described in terms of a relative phase offset:

$$\varphi = \frac{\boldsymbol{B} \cdot \hat{\boldsymbol{s}}}{\lambda} + \varphi_i, \tag{3.17}$$

where we use φ_i to denote the phase shift due to the cabling discrepancies present in the instrument. Furthermore, this phase shift is not constant across the total bandwidth; it will vary as per

$$\Delta\varphi = \frac{\boldsymbol{B} \cdot \hat{\boldsymbol{s}}}{\lambda} \frac{\Delta\nu}{\nu}, \tag{3.18}$$

where $\Delta\nu/\nu$ is the fractional bandwidth. When $\Delta\varphi \approx 1$, fringes introduced by the instrumental delay will disappear, reducing the loss of visibility in the system response. These effects can be further corrected by introducing delays at different frequencies via a technique known as fringe stopping, so as to reduce the delay offsets in each band by $\ll 10^{-8}$s. (Wilson et al. [2004])

In this section, it has been demonstrated that LoFASM is capable of detecting and is sensitive to sources of Galactic as well as extra-Galactic origin. We have shown that LoFASM, together with the use of an outrigger antenna, can be used as a radio interferometer. We've outlined methods for cleaning, inspection, and data preparation techniques. These techniques were used to take raw data collected of the power spectral density as recorded by the instrument, inspect the correlation function, and measure the fringe visibility by

analyzing the visibility function. We demonstrated that correcting for τ_g begins to shed light into how LoFASM, operating in interferometer mode, can be used to make maps of the sky, indicating that the array can certainly be used to produce scientifically meaningful results in short order. We've also discussed additional sources of instrumental delay that contribute to the instrument's ability to resolve point sources. Furthermore, it has been shown that further refinement of the visibility function should be possible by estimating the individual phase shifts introduced by varying lengths in the transmission lines of the main array of antennas, in which all signals are summed (mostly) in phase. The methods introduced here constitute building blocks upon which a rigorous long-term study of visibilities can and likely will be built.

3.3 The Galactic Background

Another avenue for confirming the viability of LoFASM as a scientific instrument that was explored is that of fitting diurnal fluctuations in intensity caused by the Galaxy rising and setting to data collected by the telescope. In this section, we discuss efforts to investigate whether or not LoFASM's response due to the Galaxy is on the order of what is expected. We start with a map of the sky produced at 408 MHz by Haslam et al. [1981]. Then, since the intensity, I_ν, observed at any given point on the sky is dependent on frequency, we use a power law to produce a corresponding intensity map for the LoFASM frequency range of 10-88 MHz. Then, using an approximate form to model the beam pattern of a ring in the LoFASM array, we integrate over the sky, now at 10-88 MHz, and use this result to generate a model of the expected integrated power for the LoFASM antennas. The software code used to generate this model was originally provided by Dr. Fredrick A. Jenet and subsequently modified by me for the purposes of this analysis. LoFASM data taken at various stations was then compared against this model via a least-squares fitting algorithm. First, I will describe the methods that we took to develop the sky model and then I will follow with a discussion

of the results.

3.3.1 Generating a Model of the Sky

For each data point on the sky, the 408 MHz map provides a temperature, T_{sky}, in units of Kelvin. Temperature is commonly used in radio astronomy as a means to identify the amount of power an antenna receives (or produces) in a given environment. In the application of the concept of antenna noise temperature, it is not the temperature of the antenna itself that is being measured. Rather, it is that of a hypothetical and perfectly impedance matched resistor that is connected to an ideal receiving element of such an antenna. It comes from a thought experiment in which an antenna is placed such that its entire beam is occupied by the presence of a black body, a theoretical object which absorbs all incident electromagnetic radiation, maintained at temperature T. If this antenna is connected to a perfectly matched load (such as a resistor) through a lossless transmission line, the second law of thermodynamics dictates that the load will reach the same temperature T at equilibrium. In the case of radio astronomy, this serves as a useful tool for estimating the amount of noise (measured as noise temperature) in a receiver.

To relate temperature T to a flux density, S_ν, measured in units of $\mathrm{W\,m^{-2}\,Hz^{-1}}$, we begin by writing Planck's law in terms of frequency ν:

$$I_\nu = \frac{2h\nu^3}{c^2}\frac{1}{e^{h\nu/k_BT}-1}, \tag{3.19}$$

where I_ν is the source *intensity*, in $\mathrm{W\,m^{-2}\,Hz^{-1}\,sr^{-1}}$, h is Planck's constant and k_B is Boltzmann's constant. At long wavelengths, such as in our case, where $e^{h\nu/k_BT} \approxeq 1$, this reduces to the Rayleigh-Jeans Law,

$$I_\nu = \frac{2\nu^2}{c^2}k_BT, \tag{3.20}$$

which, given a temperature T and frequency ν, is the intensity. The total flux density is found by integrating I_ν, which is defined for only a single (infinitesimal) direction on the sky, over the entire solid angle that is subtended by the source on the sky:

$$S_\nu = \int_{\Omega_s} I_\nu(\theta, \varphi) \cos\theta \mathrm{d}\Omega. \tag{3.21}$$

The received power per unit frequency in each antenna due to noise temperature T becomes

$$P_\nu = \frac{2k_B}{\lambda^2} A_e \int_{\Omega_s} T(\theta, \varphi) B(\theta, \varphi) \mathrm{d}\Omega \tag{3.22}$$

where A_e is the effective antenna area in the direction of the main lobe (i.e. the antenna's maximum effective area) and $B(\theta, \varphi)$ is the antenna's normalized power pattern.

Before estimating the array response, the sky temperature $T_{408}(\theta, \varphi)$ observed at 408 MHz is adjusted by the relationship

$$T_\nu = T_{408} \left(\frac{\nu}{408\,\mathrm{MHz}} \right)^{-\beta}, \tag{3.23}$$

where the power spectral index β is taken to be -2.55, a reasonable value for the LoFASM frequency range (Guzmán et al. [2010]).

To obtain the response of a single a given direction, $P_\nu(\theta, \varphi)$ is summed for all six antennas in a LoFASM ring:

$$P_{\nu,\mathrm{ring}}(\theta, \varphi) = \frac{2k_B}{\lambda^2} A_e \sum_{i=1}^{i=6} \int_{\Omega} T(\theta, \varphi) B_i(\theta, \varphi) \mathrm{d}\Omega, \tag{3.24}$$

Sky noise power $P_{\nu,\mathrm{ring}}(\theta, \varphi)$ is then integrated over the visible sky and summed for a entire sidereal day. A sampling time of 5 minutes was chosen to facilitate comparing the model to LoFASM data with the same integration time.

3.3.2 Comparison of LoFASM Data to the 408 MHz Sky

The LoFASM backend records averaged spectra with an integration time of 83.4 ms and stores the data products in 5 min. files. For this analysis, 24 hour-long data runs were down-sampled by averaging the power spectral density in each 5 min. integration, resulting in ~ 288 for every 24 hour period. A diurnal fluctuation in the measured power of ≈ 3 dB is present in the LoFASM data, indicating that the instrument is able to detect the Galaxy passing overhead and, is sky noise dominated (see Figure 3.22). Ensuring that the noise in a radio instrument is not dominated by self-generated noise produced by the electronics in the system is paramount to conducting observations of and studying astrophysical phenomena. In the remainder of this section we will discuss the method employed to fit the integrated power experimentally recorded with LoFASM stations I & III to that of the model generated from the reference data taken at 408 MHz.

We begin by defining

$$X_i' = G(X_i + M), \tag{3.25}$$

where X_i' is the raw data recorded by LoFASM in a narrow frequency band as a function of time, G is the effective frequency-dependent gain of the instrument, X_i is the calibrated power due to the galaxy, and M is a linear offset.

The least squares sum is then given as

$$V = \sum_{i=0}^{N} (Y_i - IX_i + M)^2, \tag{3.26}$$

where is defined as $I = 1/G$ and Y_i represents the Galaxy model. The local minima for the residual V are found by setting the following pair of partial differential equations to zero,

$$\frac{\partial V}{\partial I} = 0, \tag{3.27}$$

$$\frac{\partial V}{\partial M} = 0, \tag{3.28}$$

which results in the following two fitting parameters.

$$I = \frac{S_y S_{xx} + MN}{S_x} \tag{3.29}$$

$$M = \frac{S_{xx} S_y - S_{xy} S_x}{(S_x)^2 N S_{xx}}, \tag{3.30}$$

where $S_{xy} = \sum_{i=0}^{N} X_i Y_i$, $S_{xx} = \sum_{i=0}^{N} X_i X_i$, $S_x = \sum_{i=0}^{N} X_i$, and $S_y = \sum_{i}^{N} Y_i$.

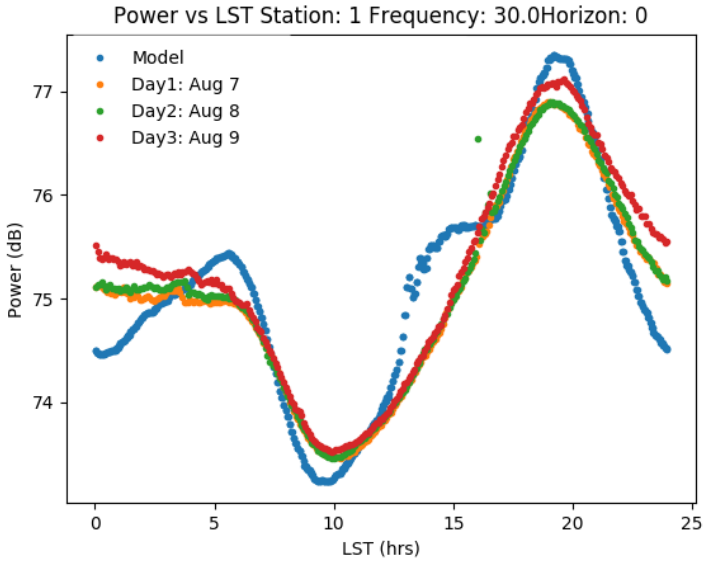

Figure 3.22: Three periods of diurnal fluctuations in the received power as taken using the INS polarization at LoFASM I compared to the expected power levels from the Galaxy. Image Credit: Paulina Varela

Figure 3.22 shows the results of the best fit for three consecutive days of data taken at LoFASM I in 2019. More examples at frequencies ranging from 25-50 MHz are shown in Figure 3.23 and the corresponding best fit parameters are given in Table 3.4. As shown, the diurnal cycle fits fairly well with the generated model. The discrepancies between the model and the LoFASM data can be attributed to several things. First off, while the application of the spectral power law using $\beta = 2.55$ seems to do fairly well in general, there are a few

key features that are present in the model that do not appear in the data, such the slope leading to the first peak from 0-5 hrs. Below 45 MHz the most of recorded LoFASM data did not match the model in the first five hours. Towards the lower end of the frequency range at 25 MHz, the presence of noise was so great that the straight-forward least squares fitting routine was not able to generate a decent fit. Further analysis and rigorous cleaning of the low frequency datasets is needed to properly study these data. The noise at 25 MHz serves as another example highlighting the fact that there is a need for novel RFI mitigation techniques for science at low frequencies.

At 45 & 50 MHz, however, data from August 7, 2019 closely resembles that of the model from 0-5 hrs, though the peak is not well resolved and the power levels differ. The fact that only data from August 7th even comes close to matching the model at these times seems to indicate the presence of high levels of noise during the observations. In fact, the August 7 dataset was the only one to meet the expected power levels near 3 hours LST. Though this agreement was short lived below 45 MHz.

Another noteworthy feature is that of the "hump" near 14 hrs present in the low frequencies that evolves into a double peaked structure above 40 MHz. There is virtually no sign of this feature set in the recorded data below 40 MHz. However, at 40 & 45 MHz some of these features begin to present themselves and at 50 MHz we can begin to see the emergence of the double peaks in data from August 8. In the complete absence of these features it could be assumed that there might be errors associated with the production of the Galactic model. However, since the structures clearly evolve with increasing frequency, it is concluded that the features are real and definitely frequency dependent. Furthermore, the emergence of the double peaked structure at 50 MHz serves as an indicator that while there is likely nothing wrong with the way the Galactic model was produced, it is probably not providing a satisfactory representation of the radio sky at LoFASM frequencies. Since the Galaxy model is based on data taken at 408 MHz, any features that are present at higher frequencies that are

not in reality also accompanied by lower frequency counterparts will contribute to apparent discrepancies in the comparison plots considered in this analysis.

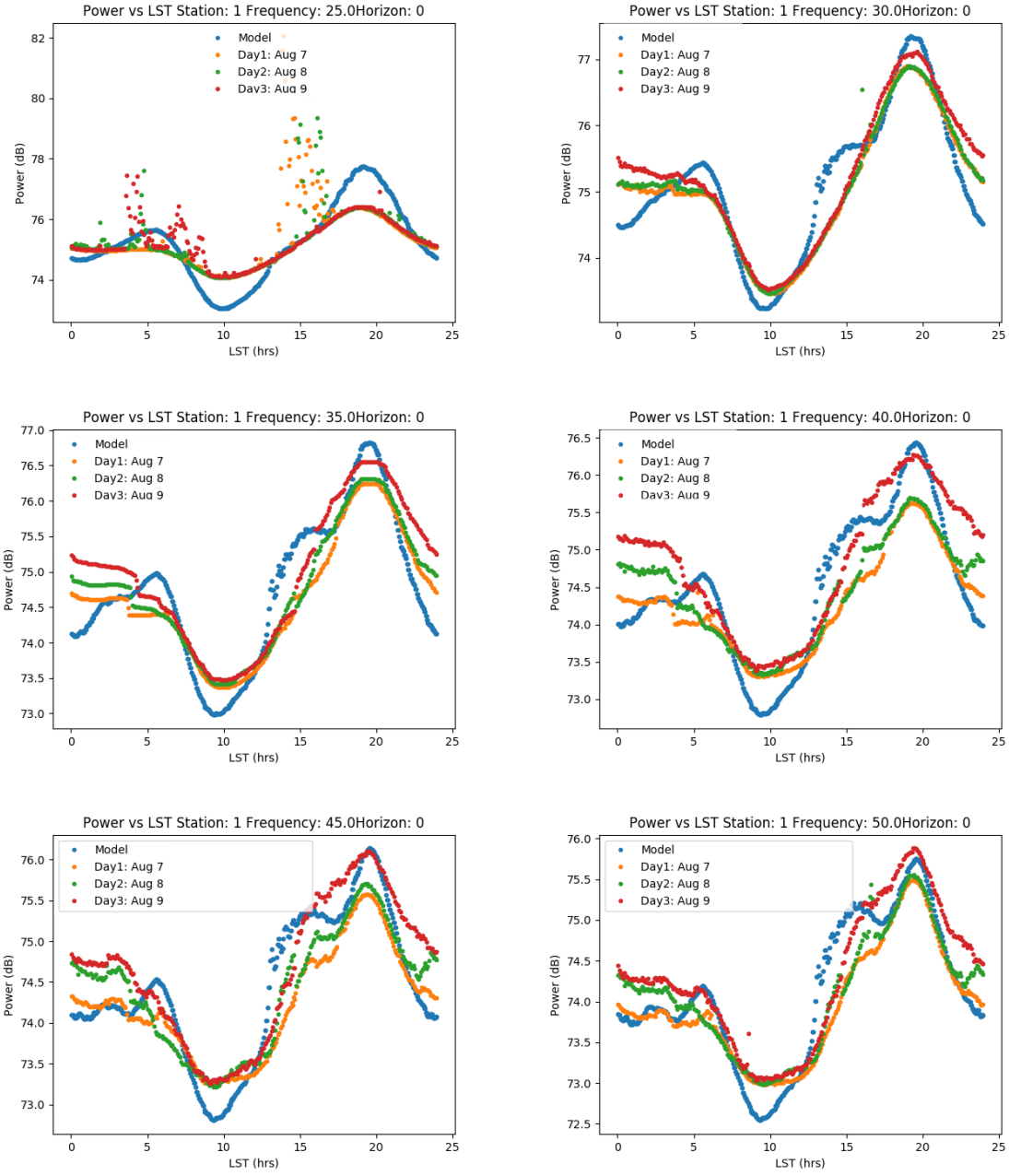

Figure 3.23: Averaged power data from LoFASM I taken using the INS polarization as compared to the expected background taken from Haslam et al. [1981]. Image Credit: Paulina Varela

Another potential concern that should be addressed has to do with the possibility that the

Frequency (MHz)	I	$M \times 10^6$	X_i (dB)	$X_i' I \times 10^6$
25	9.12	13.61	-	-
30	14.33	6.59	-	-
35	12.61	10.56	73.5	11.83
40	12.42	13.01	73.4	8.37
45	24.98	10.45	73.35	11.18
50	44.42	6.18	73.1	14.24

Table 3.4: Measured fitting parameters for LoFASM data as compared to the model generated from 408 MHz. I is a multiplicative linear fitting parameter and N is an offset. X_i is a power level that represents the typical minimum power in the recorded data and $X_i' I$ is measured linear component of the best fit at the minimum. X_i and $X_i' I$ are only given for the trials that exhibit a flat response near 10 hrs LST. The comparable sizes of M and $X_i I$ suggests that the instrument is operation at or near the noise floor at these times.

telescope could be operating near its noise floor. This means that the recorded level of noise, whether generated internally by the telescope instrumentation or externally as RFI, is higher than the signal being studied. In such cases, signals of interest are buried below the noise and therefore can not be observed or analyzed without the employment of targeted mitigation techniques. At around LST=10 hrs the power in the LoFASM data never dips to the levels present in the model. There are multiple possible explanations for this. First off, again, this may due to inherent differences between the 408 MHz sky and the sub 100 MHz sky. However, the flat nature of the recorded data above 40 MHz indicates that the instrument's noise floor of the instrument is being reached. If X_i is the plotted power from the instrument, then X_i' is given by $X_i' = (10^{X_i/10} - M)/I$. A comparison of the measured offset M and linear fitting component $X_i' I$ for the quietest regions of the measured data indicates that LoFASM is operating at or near the instrument noise floor. At 50 MHz, however, the fact that $X_i' I$ is a factor of ~ 2 larger than M, shows that LoFASM is Galaxy noise dominated in that band. This is far from conclusive evidence that the noise floor of the instrument is in effect. The flat structure is less apparent at the lower frequencies, though the recorded power levels are similar. Moreover, that the flat response near 10 hrs LST appears at various power levels at different frequencies may suggest that the noise floor is not being reached

and that LoFASM is accurately reporting the radio emissions from the sky at those times.

The analyses discussed in this section are successful in their goal to demonstrate that LoFASM is Galaxy noise dominated for a majority of the time, has achieved a dynamic range sufficient to pick up minute structure defining fluctuations in power from the Galactic background, and is relatively consistent in its response over time.

3.4 Hunting for B0329+54

Another avenue that was explored in the quest to calibrate the LoFASM array is that of using a radio pulsar as standard (pulsating) candle. Radio pulsars are highly magnetized and rapidly rotating neutron stars that emit beams of electromagnetic radiation out of their magnetic poles. Weighing more than the Sun, yet only 20 km in diameter, these super dense objects produce radio signals consisting of pulsed continuum noise that sweep the sky like the beams of a lighthouse. Since their discovery in 1967 by Jocelyn Bell-Burnell and Antony Hewish (Hewish et al. [1968]), pulsars have provided the scientific community with a wealth of information about neutron star physics (Kaspi and Kramer [2016],Harding and Lai [2006], Lattimer [2004]), general relativity (Hulse and Taylor [1975], Taylor [1994], Hulse [1994]), the Galactic gravitational potential and magnetic field (Lorimer [2001]), the interstellar medium (Stinebring et al. [2001], Barkov et al. [2020]), celestial mechanics, and planetary physics Lorimer and McLaughlin [2010]. Pulsar research has been driven by numerous surveys with large radio telescopes over the years such as the late Arecibo Telescope, the Green Bank Telescope, the Parkes telescope, and the GMRT. Although they were originally discovered at 81.5 MHz by Hewish et al. [1968], and much of their initial followup observations took place at similarly low frequencies, the lion's share of pulsar observations conducted since the 1970's were at 350 MHz or above until promising lower frequency instruments were developed and began detecting pulsars regularly (Stovall et al. [2015]).

The formidable population of known pulsars presents an opportunity for the commis-

sioning and calibration of LoFASM. If a pulsar can be detected by a LoFASM station then it will serve as a testament as to the capabilities of the instrument. With the exception of a few very rare and serendipitous cases, one does not typically stumble upon a pulsar's signal without seeking it. Furthermore, with the detection of a known pulsar, LoFASM's sensitivity can be calibrated, at least at the detection frequency. However, the detection of such an elusive type of source is not expected to be easy even when using larger & more sensitive instruments. Most pulsar detections have been achieved by taking advantage of highly sensitive and tight beams on the sky and integrating over time. As they travel across the interstellar medium (ISM) pulsar signals are affected in a few keys ways. The frequency dependent effects due to dispersion cause the lower frequency portion of a broadband pulse to lag behind its high frequency counterparts, effectively smearing the pulse over time. The size of this effect, called the dispersion measure (DM), is related to the total column density of free electrons along the line of sight to the pulsar and can be used to estimate the distance between Earth and the source of the signal. Pulse scattering due to irregularities in the ISM also manifests in the form of broadened pulses. Pulses that would otherwise appear intrinsically sharp in observations are widened due to scattered rays arriving at the instrument's receivers later than they would had no irregular pockets in the ISM been present.

The dispersion affecting a pulse as it travels through the ISM, which is a effectively a cold, ionized plasma, will manifest as a delay in the time of arrival between the highest and lowest frequency emissions. This is due to the frequency dependence of the group velocity of an electromagnetic wave as it travels through the ISM:

$$v_g = c\sqrt{1 - \frac{{f_p}^2}{f}}, \tag{3.31}$$

where c is the speed of light, and f_p and f are the plasma frequency and observing frequency, respectively. The time delay in the arrival of emissions between two frequencies will depend primarily on the distance to the source and the density of free electrons present along the

line of sight between Earth and the source. The DM, usually expressed in $\mathrm{cm}^{-3}\,\mathrm{pc}$, is related to these quantities by

$$DM = \int_0^d n_e dl, \tag{3.32}$$

where the number n_e is the density of free electrons and d is the distance to the source of emissions. A wave of frequency f will be delayed as compared to a wave of infinite frequency by

$$t = \mathcal{D} \times \frac{\mathrm{DM}}{f^2}, \tag{3.33}$$

where f_1 and f_2 are in MHz and $\mathcal{D}$, known as the dispersion constant, is defined by Lorimer and Kramer [2004] as

$$\mathcal{D} = \frac{e^2}{2\pi m_e c} \simeq 4.15 \times 10^3 \ \mathrm{MHz}^2 \ \mathrm{pc}^{-1} \ \mathrm{cm}^3 \ \mathrm{s}. \tag{3.34}$$

Finally, the time delay observed between two finite observing frequencies is given by

$$\Delta t \simeq \mathcal{D} \times (f_1^{-2} - f_2^{-2}) \times \mathrm{DM}. \tag{3.35}$$

As part of this work, we searched for Pulsar B0329+54 in archival LoFASM III data from 2020. To improve the prospects of detecting a pulsar with LoFASM, a relatively bright, slow, and well characterized pulsar, B0329+54, was selected (Cole and Pilkington [1968], Deller et al. [2019], Hassall et al. [2012]). Additionally, the fact that B0329+54 had previously been detected by Stovall et al. [2015] in LWA data within LoFASM's frequency range amplified its candidacy as reasonable pulsar to look for. With the LoFASM backend's long integration time, which is on the order of 100 ms, searching for a millisecond pulsar would not have been feasible. Furthermore, using the entire usable LoFASM spectrum of 15-88 MHz was also out of the question. Pulse dispersion is a frequency dependent effect that scales with f^{-2} and results in far more temporal smearing at low frequencies than at high frequencies. The pulse

smearing within a single frequency channel produced by the LoFASM Spectrometer must not exceed the rotational period, P_0, of the pulsar. Figure 3.24 shows the expected temporal smearing of B0329+54 in the LoFASM band as a function of frequency.

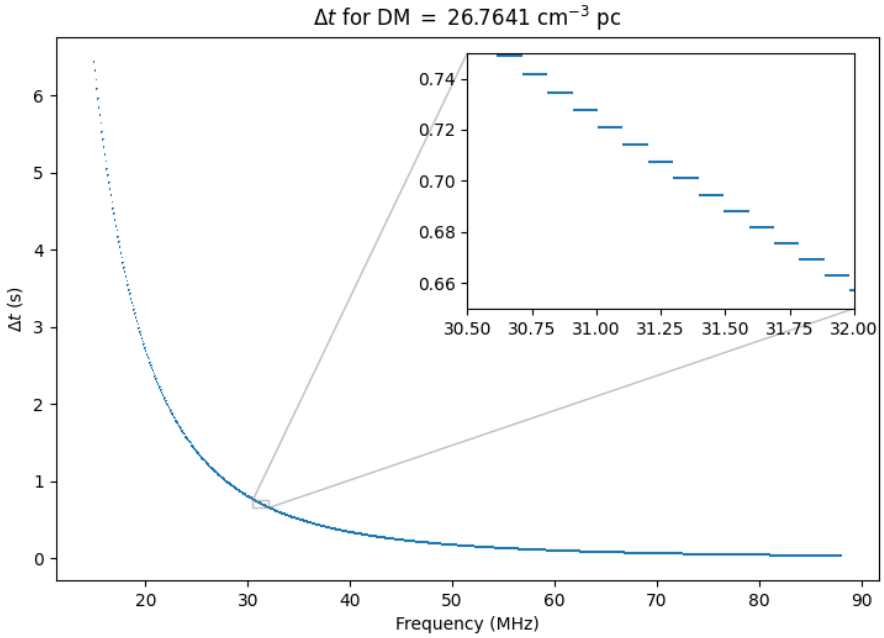

Figure 3.24: Temporal smearing due to B0329+54 across the LoFASM frequency band. Each horizontal lines mark the start and stop frequencies for each discrete frequency bin as provided by the LoFASM Spectrometer. Since the maximum smearing across any given frequency bin must be below the rotational period of the pulsar being observed, $\Delta t \leq P_0$, the 31.15 MHz bin is the lowest usable point on the spectrum that can be used to observe B0329+54. Therefore, in a dataset completely void of RFI the maximum bandwidth that can be used to observe B0329+54 in data recorded with the LoFASM Spectrometer ranges from 31-88 MHz.

If $\Delta t > P_0$, the consecutive pulses from a pulsar signal will smear into each other, rendering them indistinguishable from one another. Therefore, it is simply not possible to observe a pulsar below 31.5 MHz with a frequency resolution $\Delta\nu \geq 97.6$ kHz. To avoid these smearing issues while using as wide a band as possible, the 40-70 MHz window was chosen for this analysis. The upper limit was imposed by the presence of high levels of RFI from 70-75 MHz.

Another important factor to consider when searching for a pulsar is the instrument's time resolution; the duration for which data is averaged or collected before being packaged

as a single time sample, in this case, of the PSD. Due to limited computational capacity, the LoFASM backend averages each PSD sample for 83.4 ms. This is great for from a cost and student training perspective, but falls short of what is needed to fully resolve most transient phenomena. In order to effectively resolve the each pulse in the buried pulsar signal and be able to reconstruct its phase during when attempting to correct for dispersive effects, a process called dedispersion, it is preferable to use an instrument capable of collecting 10 or more time samples across the pulse phase. In the case of B0329+54, the ratio of the rotational period of the pulsar to the spectrometer integration, or averaging, time is

$$\frac{0.714 \text{ s}}{0.0834 \text{ s}} \approx 8.56, \tag{3.36}$$

which is not quite the ideal scenario, but still potentially good enough for a detection. The most important part of the pulsar searching process happens after the data is collected. The raw data must be cleaned, analyzed for RFI, calibrated when possible, dedispersed (coherently or incoherently) and finally folded in order to potentially reveal the pulse profile.

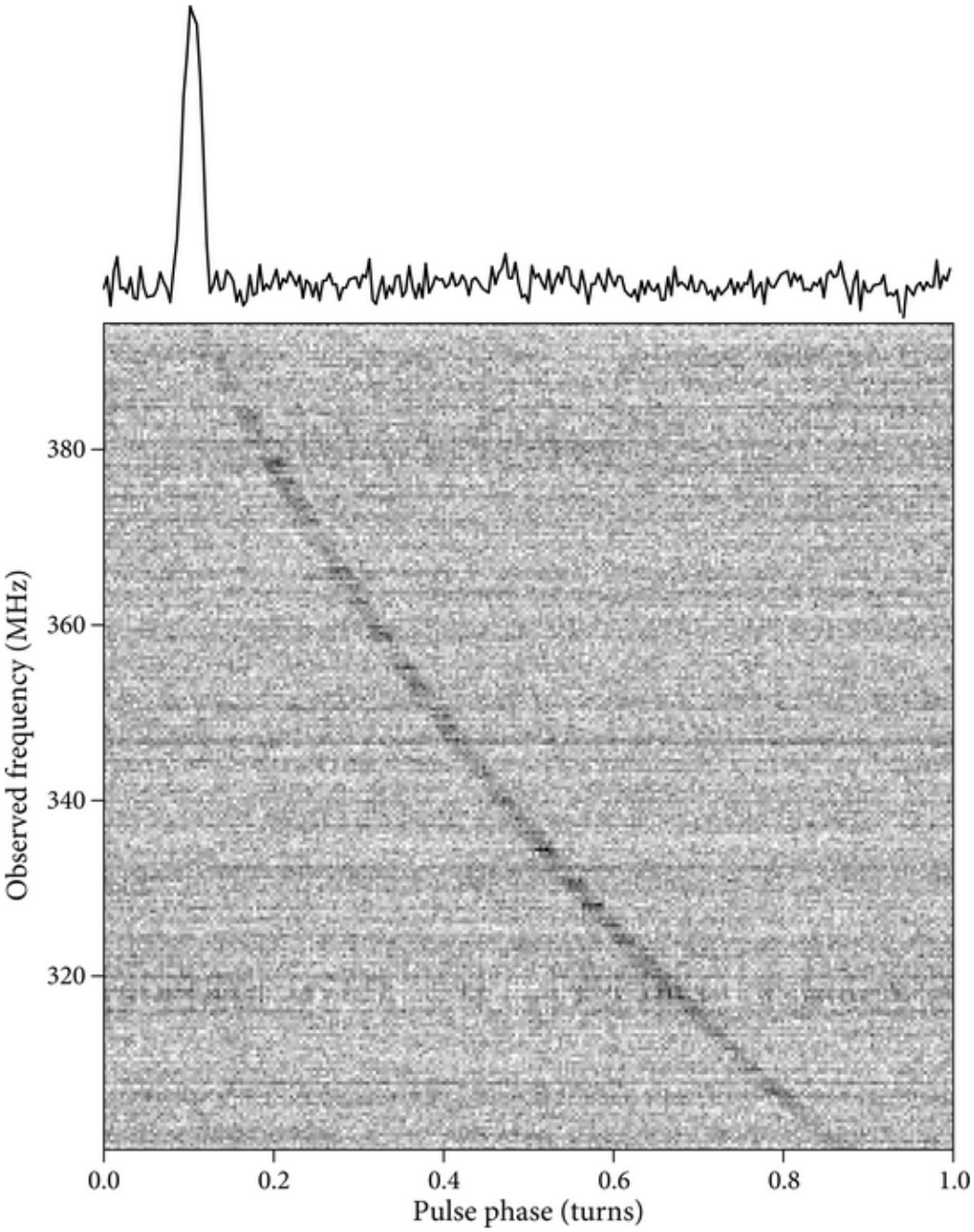

Figure 3.25: An example of a pulsar pulse profile. The spectrogram below shows that the higher frequency emissions arrive at the receiver before that of the lower frequencies. From a data acquisition perspective, the pulse profile must be well sampled throughout the arrival of the wideband pulse front in order to resolve and, eventually, reconstruct the signal. Credit: Condon and Ransom [2016]

Early efforts to detect B0329+54 using one of the LoFASM stations were unsuccessful. However, the methods I employed were far from exhaustive and they should not in and of

themselves be considered a strong indicator that a detection of B0329+54, B1919+21, or another pulsar is not imminent. My own search for B0329+54 served to stimulate the development of a data cleaning and preparation pipeline that is still in its infancy. The pipeline, a set of software tools written to facilitate the analysis and exploration of LoFASM spectrogram data, comprises programs and scripts written in C/C++ and Python, respectively. Capabilities provided by the LoFASM software tools include the excision of prohibitively noisy (deemed "bad") frequency channels, averaging, re-sampling, re-scaling, and filtering of data.

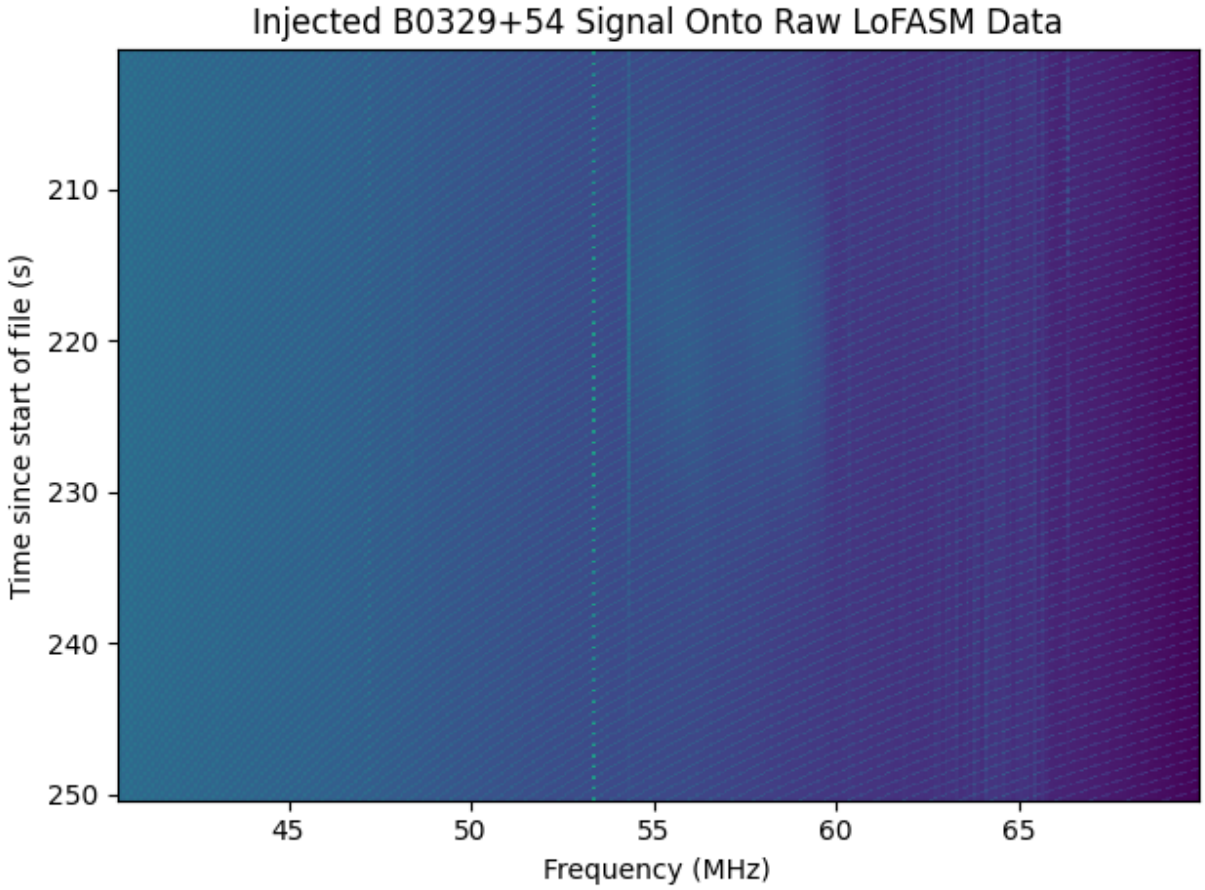

Figure 3.26: B0329+54 simulation injected onto raw LoFASM data shown over a ∼50 s stretch of time. Due to the effects of dispersion, the pulses are smeared more sharply over time at the lower frequencies. This signal is injected into real LoFASM data to test the software pipeline.

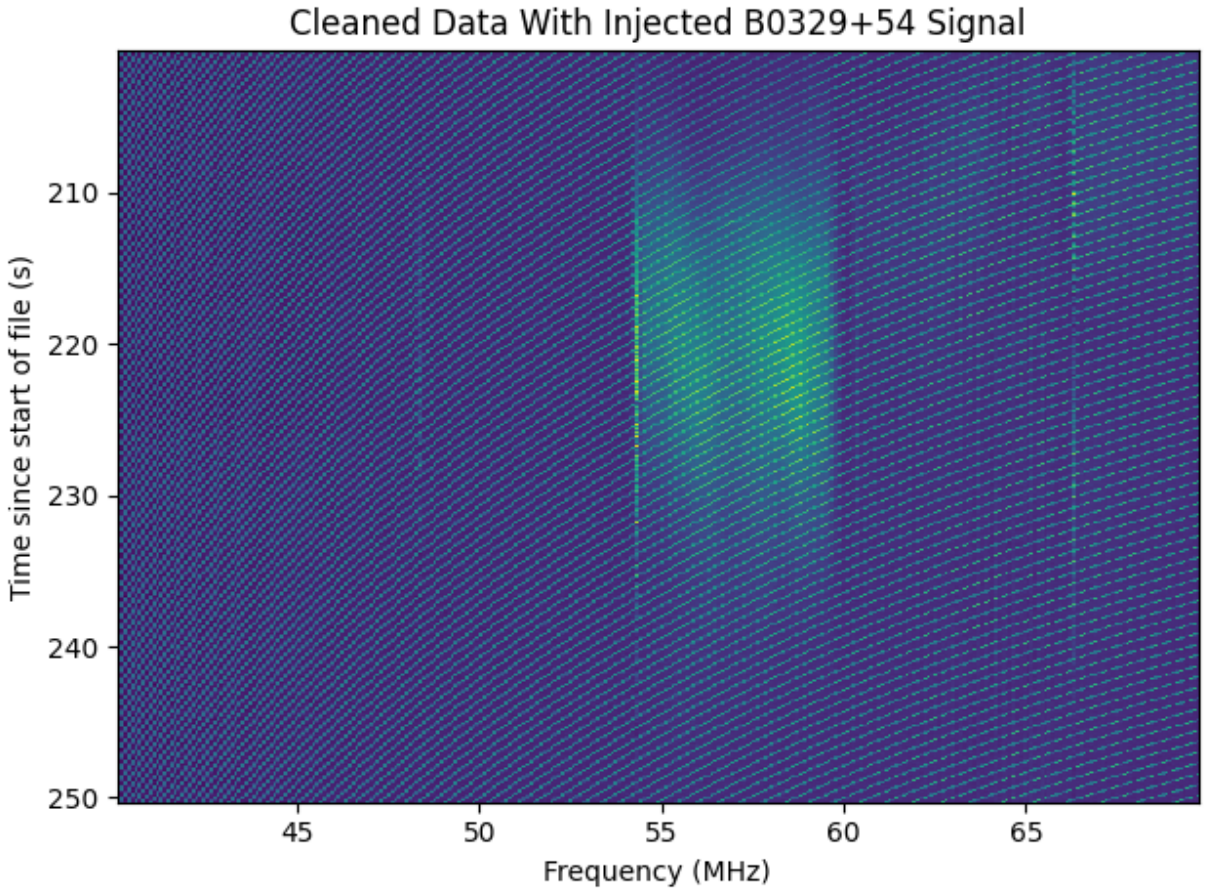

Figure 3.27: *Cleaned* B0329+54 simulation injected onto raw LoFASM data shown over a ∼50 s stretch of time. The cleaning process is seen to preserve the pulsar signal while successfully pulling out underlying features in the spectrogram: evidence of a working pipeline that can be used for pulsar searches.

Finally, as a way of confirming that we have a working pipeline in place, a simulated pulsar signal mimicking B0329+54 was injected into raw LoFASM data. Figure 3.26 shows a zoomed view of the simulated pulsar signal injected onto raw unprocessed LoFASM data. The frequency range of the data and signal injection was restricted to 40-70 MHz to account for the time smearing of the pulses at low frequencies. The same data set after being processed with the LoFASM cleaning pipeline is shown in Figure 3.27. As observed, the pulsar signal can is still clearly present. Additionally, underlying features in the spectrogram have been successfully enhanced. This data set was then searched using a set of pulsar search and

analysis tools, developed by Ransom [2011], called PRESTO.

Figure 3.28 shows the PRESTO output of this exercise. The plot in the top left corner depicts two periods of the pulse phase corresponding to the best pulsar candidate selected by PRESTO's algorithm. The prominence of the two peaks indicates that the injected pulsar signal is detected. The successful detection demonstrates that we have a working end-to-end pipeline and that, in principle, it is possible to detect a radio pulsar in LoFASM data.

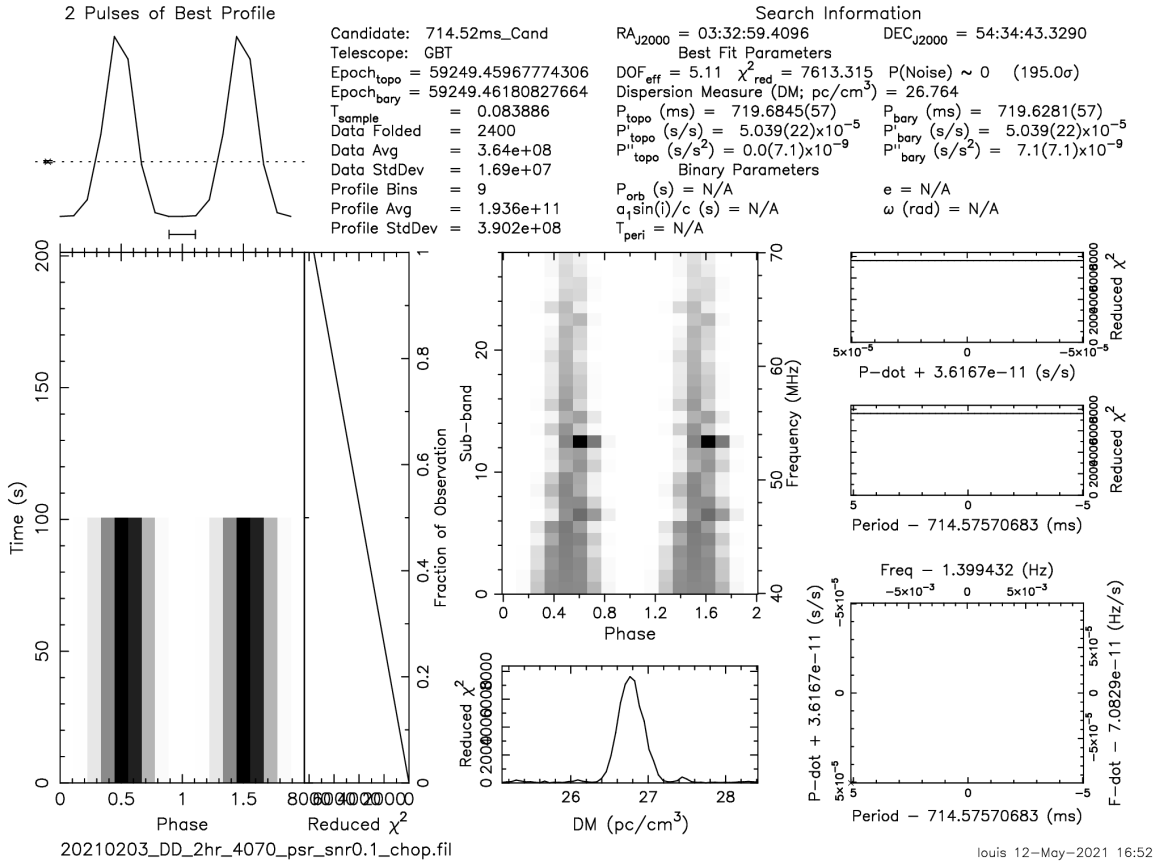

Figure 3.28: PRESTO output showing that the simulated pulsar signal that was injected into the LoFASM data set and subsequently processed by the software pipeline is detectable, demonstrating that we have a working end-to-end pipeline.

CHAPTER 4

TELESCOPE OPERATION

4.1 Recording Spectrometer Data

The backend operating procedure is *practically* identical for all of the LoFASM stations. While the input signals the correlator may differ from station to station, the data recording process is fundamentally the same. This process can be boiled down to the following steps:

1. Connect to FPGA board and load spectrometer firmware
2. Initialize spectrometer firmware; starting streaming data
3. and Start LoFASM recorder.

The LoFASM recorder does not usually run indefinitely. It must be checked and restarted periodically. Typically, this is on the order of 10 days, but can be changed as needed by the operator. Details for operating the LoFASM Data Recorder and the LoFASM spectrometer are included in Appendix C.

4.2 Data Channel Configuration

All LoFASM stations currently run on the same four-input digital backend architecture. However, since all of the active stations also have an outrigger antenna there are more analog RF signals (6) than there are available inputs for digital processing (4). This requires careful selection of which signals to record. Furthermore, it is sometimes useful to periodically change the signal set being recorded at a particular station, meaning that one or more RF signals need to be unplugged from the ROACH board to make way for a channel that was previously sitting idle.

4.2.1 LoFASM I

At LoFASM I, this signal swapping happens manually. Someone from the LoFASM team must drive out to the site, pause the spectrometer, reconfigure the RF cabling in the electronics shelter, then update the new trunk line mapping, and finally restart the data-taking routine. Table B.6 shows the most recent RF signal mapping installed at LoFASM I. The physical wiring diagram at these stations closely resembles that of Figure 2.15. The tables in this section, along with additional details, have been placed in Appendix B.5 for quick access.

Polarization	Trunk Line	Channel ID	ARX Channel	Current (A)
INS	3	D	1	1.21
ONS	1	B	2	1.46
ORNS	-	C	3	0.23

Table 4.1: Cable mapping as of October 1, 2019 at LoFASM I. The trunk line column denotes the cable labeling inside the control room in Port Mansfield, the Channel ID is the resulting channel code assigned to the data products once they've been pre-processed by the digital backend, the ARX Channel denotes the input that was used on the four-channel ARX module, and the current draw for each channel is logged for long term health monitoring purposes. One channel was left open due to pending repairs on site.

4.2.2 LoFASM III

LoFASM III has had RF switches implemented to facilitate the *remote* switching of RF signals into the digital processing units. In these cases, the antenna FEEs are powered indefinitely and are never idle, even if they're not plugged into the ROACH board. Figure 4.1 shows a high-level view of the current channel mapping installed at LoFASM III.

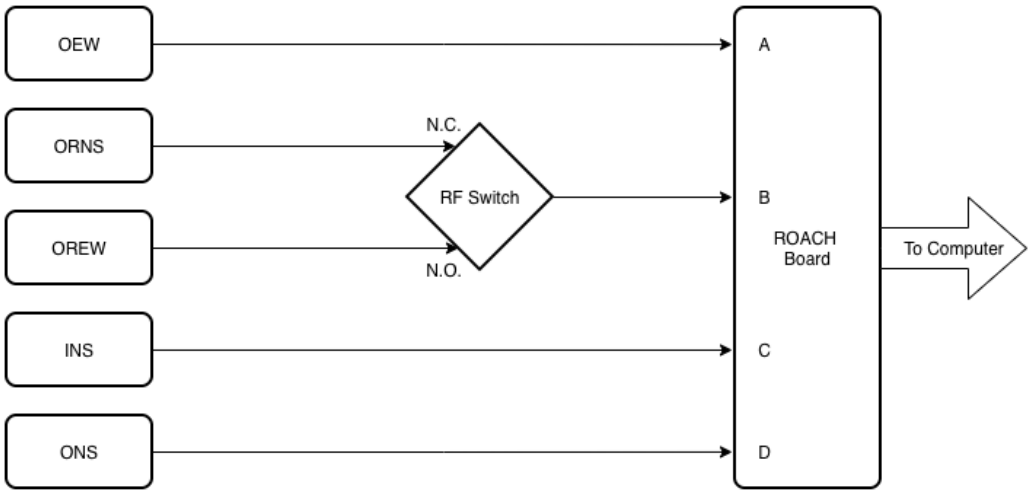

Figure 4.1: High level flowchart of the channel mapping at the LoFASM III.

The RF switch can be remotely controlled to change observing modes between recording with the NS or the EW outrigger polarization. The RF switch port mapping is given in Table 4.2. In fact, there is a second RF switch at LoFASM III that is currently not connected. Channel IEW is currently inactive due to FEE failures that are currently pending repairs. With both RF switches working, it is possible to implement more observation mode choices, including the ability to choose between "full outrigger" and "full LoFASM array" modes. The channel mappings for the two currently available observation modes are given in Tables B.8 and B.9. Furthermore, details on how to toggle the RF switch state at LoFASM III to swap observation modes is provided in Appendix B.5.2.

N.C. Port	N.O. Port
ORNS	OREW

Table 4.2: The RF switch configuration at LoFASM III. The output of the RF switch will either be ORNS or OREW, depending on which port is activated. "N.C." stands for "normally closed" and "N.O." stands for "normally open". The N.C. port is usually connected by default unless the switch is activated to connect to the N.O. port instead.

4.2.3 LoFASM IV

Like at LoFASM III, an RF switch system has been implemented at LoFASM IV. In fact, LoFASM IV was the first LoFASM station to have this upgrade installed. However, unlike its sister station, the switch system at LoFASM IV is not digital. An analog module consisting of dual switches with physical knobs is used to select which RF trunk lines are connected to the ROACH board. As a result of having two individual switches at LoFASM IV, there are four available observation modes that can be selected at this site. Table 4.3 contains a list of the available observation modes and their corresponding knob configurations. A channel mapping for each of the four recorded inputs is included in Table 4.4.

Knob Configuration	Observation Mode
A1,B1	Full LoFASM Array
A2,B2	Full Outrigger Mode
A2,B1	Outrigger N-S
A1,B2	Outrigger E-W

Table 4.3: RF Switch configurations at LoFASM IV. Each row corresponds to a unique observing mode that LoFASM IV is capable of. The knob configuration column lists the setting of each of the two knobs on the analog switch module. Each knob, A & B, has two settings: 1 & 2. This provides LoFASM IV with the four possible signal combinations listed here.

Data Channel	Polarization
A	INS
B	IEW
C	ONS / OREW
D	OEW / ORNS

Table 4.4: Channel mapping for each of the four ROACH board inputs at LoFASM IV. Due to the RF switches installed at this site, channels C & D each have two possible input signals.

4.2.4 LoFASM V

While it is actively taking data, the mapping at LoFASM V currently needs to be verified. LoFASM V is the newest LoFASM station and, as such, is still in the early commissioning stages and undergoing extensive field testing to realize a stable RF signal chain.

CHAPTER 5
FUTURE WORK & POTENTIAL AVENUES OF INVESTIGATION

5.1 Instrument Calibration

5.1.1 Galactic Background

The experiment discussed in Section 3.3.2, in which the radio sky at 408 MHz was used for comparisons in the LoFASM frequency range, successfully demonstrated that the LoFASM array is sensitive to the diurnal fluctuations in power due to the Galaxy passing overhead. However, many questions were left unanswered. The presence of features in the 408 MHz dataset that did not at all appear in the LoFASM data, such as the peak near 5 hr LST at LoFASM III, begs the question: are these discrepancies indicative of poor sensitivity in the LoFASM array or are they merely features that are present in the 408 MHz sky but not below 100 MHz? Another open question was that of the LoFASM noise floor. Though the LoFASM data corroborated the features detected while the Galaxy was overhead, the collected data did not reach the lowest power point as reported by the model at 408 MHz.

These questions, and more, can likely be answered by performing a similar comparison to the radio sky at sub 100 MHz. The most promising candidate for these analyses are the maps produced by the LWA stations. Eastwood et al. [2018] and others have studied the radio sky at LoFASM frequencies. Moreover, the LWA stations are located at similar latitudes and use the same antennas as the LoFASM stations. Comparison between data collected by the LoFASM arrays and the various LWA stations continues to represent a valuable avenue of future work for characterizing the LoFASM response.

5.1.2 Artificial Transmitter

Use of astrophysical sources as calibrators, though common, are not the only way to characterize and calibrate the LoFASM array. Full beam pattern calibration and power sensitivity characterization can be achieved by using a wide band RF transmitter mounted onto a drone. Chang et al. [2015] and Briechle [2017] have used this technique to calibrate a radio dish and an array, respectively.

The biggest technical challenge to keep in mind is that of ensuring that the drone + transmitter system is far enough away from the LoFASM array to guarantee far-field conditions. This is not much of an issue at higher frequencies but at 20 MHz, the recommended distance of $10\lambda \approx 150\,\text{m}$ may be tricky to achieve. While useful throughout the entire 15-88 MHz region, calibration is particularly important for the 20 MHz band. The LoFASM antenna footprint described in Section 2.1.2 is specifically designed to maximize the attenuation of RF from the horizon at 20 MHz. Thus, precise measurement of the full LoFASM beam pattern and its horizon rejection properties at this frequency would be very valuable as the first test to experimentally confirm or characterize the initial LoFASM simulations.

5.1.3 Interferometric Lightcurves

LoFASM's can be used in combination with a drone-mounted transmitter to map out the beam pattern. While this can be done by using the telescope in the traditional array mode, the ability to track the transmitter's geometric delay over time, when operating the station as an interferometer, provides additional value. If data from both LoFASM rings and the transmitter is recorded simultaneously in the same polarization, the synthesized beam pattern can be effectively mapped as well, which will make it possible to study the efficacy of LoFASM's horizon rejection at 20 MHz. If the transmitter is well understood, this method can also be used to fully calibrate the LoFASM array.

Another potential calibration approach is that of using celestial radio sources on the sky

instead of an artificial transmitter mounted on a drone. Sources such as CasA, CygA, VirgoA, and TauA, all of which have been previously observed in LoFASM data, can be tracked via their delay plots over long periods of time (≥ 1 month) and studied glean power calibration information about the telescope. These sources are all relatively well understood, as is the ratios of their power in the LoFASM frequency range. Furthermore, analyses of observations (or lack there of) of the variations in the intensity ratios from the two brightest sources, CasA and CygA, over time may yield quantitative information related to the sensitivity of the instrument.

5.2 Traveling Ionospheric Disturbances

Propagating plasmaspheric irregularities in the ionosphere, also called traveling ionospheric disturbances (TIDs), are known to negatively affect radio observations. This is particularly true at low frequencies. (Obenberger et al. [2019]) As a result, the simulation, observation, and characterization of TIDs is an active area of research. (Loi et al. [2015], Koval et al. [2018], and Koval et al. [2019]) Furthermore, the high-resolution study of TIDs is a supporting consideration in the design of next generation radio instruments. (Taylor et al. [2017])

TID effects can manifest in spectrograms as so-called "Spectral Caustics" in the form of inverted V-like, V-like, X-like, and other morphologies. (Koval et al. [2018]) It is possible that data taken at the LoFASM I and LoFASM V exhibit the hallmark TID effects in archival data. Figure 3.1 shows possible signs of this behavior near the 1 min mark. In addition, Dolch et al. [2020] have seen similar activity in data taken at LoFASM V (see Figure 5.1).

The presence of TIDs in LoFASM data suggests that ionospheric research may be an additional avenue of independent research for which LoFASM may be a valuable instrument. The real-time characterization of ionospheric distortions would improve the localization of sources, particularly when the station is being used as an interferometer. Since the ionosphere is mostly created by the interaction of radiation originating from the sun, ionospheric plasma

has a strong coincident cycle dependence. Furthermore, correlation between potential TIDs in LoFASM data and the planetary K-index (Kp Index) could hold additional clues as to the association between these observed phenomena and the solar cycle.

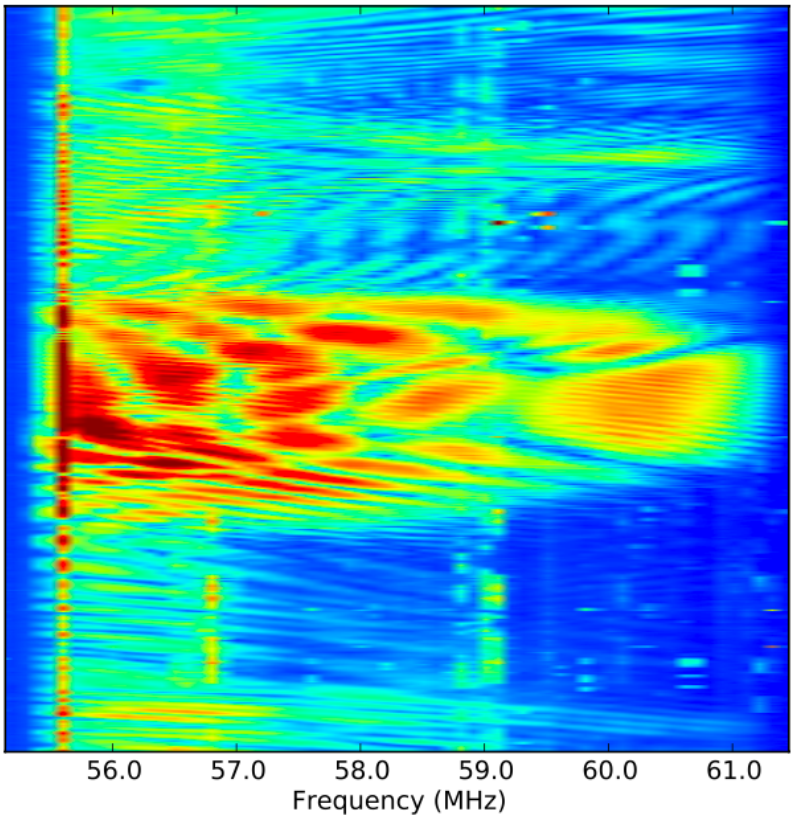

Figure 5.1: Potential evidence of traveling ionospheric disturbances in spectrogram data taken with LoFASM V and identified by Dolch et al. [2020].

5.3 Jovian Activity

The study of Jovian radio emissions, which were first discovered by Burke and Franklin [1955] at 22.2 MHz, is an exciting and active area of research. This is particularly true for low frequency radio astronomers since emissions have been detected all the way down to the lower ionospheric cutoff of 10 MHz. Though Jovian emissions have been studied extensively since their discovery, many open questions remain as to the nature of the underlying emission mechanisms at play. It is known that one of Jupiter's moons, Io, plays a role in amplifying a

subset of Jovian emissions during certain parts of its orbit. However, there are also various emission mechanisms that have been found to not be related to Io.

Clarke et al. [2014] showed that the LWA is able to detect Jovian emissions from Io-related events as well as short millisecond bursts and narrow band events. Other instruments that are used to study Jovian activity in the LoFASM frequency band include LOFAR, UTR-2, and the Nançay Decameter Array. Although the LWA contains an order of magnitude more antenna elements than a LoFASM station, the high intensity of Jovian emissions at low frequencies might yet be detectable. Furthermore, searching for Jovian emissions in interferometer mode with LoFASM has yet to be done.

High intensity Jovian L-bursts, which can last for several seconds, could be detectable to LoFASM stations with the current data-processing configuration if they are bright enough. Additionally, LoFASM's potential for horizon rejection at 20 MHz has the potential to further improve the chances of observing decameter emissions lasting on the order of seconds. On the other hand, shorter milliseconds bursts might still prove to be out of reach for LoFASM operating in the current spectrometer mode due to the long time averaging that takes place. To combat this, the backend would need to be upgraded to support shorter averaging windows or a baseband data mode. Simultaneous observations of Jovian bursts at multiple LoFASM stations would pave the way for developing a pipeline to detect more elusive signatures, such as those from FRBs. The search for Jovian activity presents a interesting challenge to LoFASM and could serve as a stepping stone to exciting new studies.

5.4 Exploring Additional Data-Taking Modes

Currently, all LoFASM data, whether in "Full Array" or Interferometer mode, is recorded using the LoFASM Spectrometer. However, the LoFASM Data Recorder is agnostic to the type of data being received. As such, it is fully capable of supporting additional data-taking modes and backend systems as long as they broadcast over a network cable in the same way

as the ROACH board does.

5.4.1 Narrow Band Spectrometer

The spectrometer's averaging time is data-rate limited. While the digital backend is capable of producing data at shorter integration times, the control computer must be able to keep up with ingress of data for extended period of time. One way to circumvent this issue is to operate the existing spectrometer over a smaller frequency range. This will effectively reduce the amount of data that is being sent from the backend to the control computer for any given set of integrations. Effectively, this will amount to squeezing more data out of the limited bandwidth availability. Initially, I suggest removing the stopbands at the firmware level. RF signals at frequencies outside of 15-75 MHz are purposefully filtered out in analog before they reach the ADCs. As such, no science or meaningful instrumentation is being conducted in the frequency ranges at this time. However, filtering this region of the spectrum at the FGPA firmware level will have multiple consequences. First, LoFASM will not lose any important information and will gain from shorter integration times (by a factor of 2). Secondly, the resulting 60 MHz bandwidth will negatively impact the delay resolution when operating in interferometer mode. To combat this, all that is needed is to zero-pad the stop bands before producing the delay plots. That is, fill the 0-15 MHz and 75-100 MHz regions with zeros, making sure to use the correct frequency step, $\Delta\nu$, and channel width before performing the inverse-FFT. The will likely result in cleaner data than has been seen thus far.

5.4.2 Recording in Baseband Mode

The LoFASM spectrometer is useful because it effectively reduces data by performing a running FFT, cross-power calculation, and time averaging on each channel in real time (refer to Figure 2.18). However the spectrometer implementation is not a lossless process. Specifically,

phase information is lost during the calculation of the autocorrelations, the output of which are real-valued numbers. The loss of this information carries with it significant consequences to the search for astrophysical transient phenomena. Fast radio bursts and pulses from radio pulsars cannot usually be detected outright. Effects imposed through the course of interstellar propagation must be removed before these signals can be successfully detected. The process of removing these effects is called dedispersion (see Section 3.4). Dedispersion that is performed on detected intensities, such as those recorded by the LoFASM spectrometer, is called *incoherent* dedispersion due to the fact that the original signal's phase information is lost during the detection process (e.g. the autocorrelation). Since the phase information is lost, it is not possible to fully correct the dispersive effects in signals produced by the LoFASM spectrometer. Therefore, incoherent dedispersion serves to approximate the effects of the dispersion and remove them. In many cases this is enough to sufficiently resolve pulses from radio pulsars and signatures from FRBs.

In order to fully remove the effect of dispersion, complex voltage data must be used. The voltage is proportional to the electric field received at the antennas. The process of recording the raw voltages as a function of time is called baseband recording. Using baseband data, the dispersive effects can be exactly removed via *coherent* dedispersion. Additionally, with baseband data one has full control over how to implement post-processing steps such the FFT, cross-correlations, the application of various window functions, etc. This, however, comes at the cost of having to deal with larger datasets, more computationally intensive processing implementations, and consequently longer processing times.

The first successful detections of bursts with LoFASM will likely be done using baseband data. A baseband recording mode has been designed for use at LoFASM. The rollout and testing of such a recording mode is yet to be done and its details are outside of the scope of this work. However, the LoFASM Data Recorder was designed with the upcoming baseband mode in mind and is configured to support the new data taking mode. Furthermore, when it

comes online the new baseband mode will benefit operation of LoFASM as an interferometer. High time resolution phase information that is lost during averaging will be retained in the baseband data, therefore increasing the corrective phase control that is critical to phase interferometry. Additionally, there will be no need to compute the delay spectrograms that were used as part of this work. Instead, phase shifts and two-element beamforming principles can be applied directly to the baseband data streams.

The baseband recording mode has the potential to provide LoFASM with a new set of eyes. Ideally, LoFASM would operate in baseband mode indefinitely while storing data in a ring buffer that is continuously fed to a spectrometer. Unfortunately, this capability can not be achieved using the components that currently make up the LoFASM backend system. Limitations due to the amount of logic that can be simultaneously executed on the ROACH's FPGA chip restrict the available observation modes to either baseband or spectrometer recording. Through the use of powerful graphics processing units (GPUs), a real time spectrometer could be implemented on the control computer. In such a scenario, the current ROACH boards could continue to be used in baseband mode to stream data to the GPUs. There are currently no GPUs installed at any of the LoFASM stations. Such an upgrade would likely require completely replacing the control computers. In recent years it has become common to move the entire pre-processing system away from FPGAs and onto GPUs-based systems. In such configurations, the FPGA is used only to digitize, packetize, and stream data to a control computer (or network of control computers) hosting GPUs that implement running FFTs, correlating spectrometers, beamformers and other tools useful for radio astronomy.

Due to the required throughput and given the currently available hardware, it may not be feasible to operate LoFASM in baseband mode for extended periods of time. Therefore, it will likely only be used during targeted windows during which the spectrometer is not sufficient. A promising operating principle for LoFASM to achieve is one in which the spectrometer

serves as the default mode which routinely scans the sky for bursts or interesting signatures. In the event that a burst is detected by one of the stations, an alert can be sent out to all LoFASM stations that triggers them to treat the event as a target of opportunity in which they switch to baseband mode for a predetermined length of time. This procedure will allow for LoFASM to optimize the use of the baseband data it records. Of all the existing and upcoming research endeavors at LoFASM, I believe that the rollout of a stable baseband recording mode should remain among of the highest priorities.

5.5 Time Delay Interferometry

The potential for LoFASM to be used as a two element interferometer opens the doors to a wealth of new potential studies. Data taken in interferometer mode at various LoFASM stations has proved to be more sensitive to point sources than was originally expected. Initially, it was expected that the LoFASM array would be able to resolve the Galaxy and potentially the brightest of bursts. However, the analysis of delay plots such as the one in Figure 3.17 presented more than just the successful detections of CygA and CasA. In that figure alone there are clearly at least six other point sources. Lightcurves of CygA, CasA, and the remaining as of yet unidentified sources can be produced by analyzing the delay plots. Instead of selectively summing across the entire delay track, these tracks can be extracted and independently analyzed for variabilities on short timescales. Flux density ratios between CygA, CasA and other sources such as the Sun, TauA, and VirgoA can be investigated over extended periods of time to further inform the calibration process for LoFASM as noted in Section 5.1.3.

Furthermore, interferometry can be used to aid in the detection of known radio pulsars. Lightcurves of known pulsar positions can be analyzed to search for pulsations. For a pulsar with a relatively small DM value, such as B1919+21, it is possible that the pulsations may appear in the delay track before dedispersion takes place. This search is currently an ongoing

research endeavor at LoFASM. Undispersed radio emissions, such Jovian L-bursts may also be detectable by using LoFASM in interferometer mode. The position of Jupiter is known and can be monitored over long periods of time to search for short and long timescale emissions. The long integration time ($\approx 84\,\mathrm{ms}$) of the LoFASM spectrometer restricts such detections to those of bursts that last on the order of several seconds. Nonetheless, with improvements to the backend system or with additional data-taking modes even the shorter Jovian S-bursts may be detectable.

CHAPTER 6

SUMMARY & CONCLUSIONS

In this thesis we have presented the initial demonstrations of LoFASM as a working instrument. We have reviewed data showing that LoFASM, a student built and operated radio telescope, is capable of detecting radio sources, both anthropogenic and natural, of terrestrial, Galactic, and extra-galactic origins. The execution of the analyses discussed herein, along with their methodologies and the development of their software data processing pipelines, set the stage for future research endeavors to be conducted using the network of LoFASM telescopes, as each category of data analysis carried out and demonstrated in this thesis is a potential line of research moving forward. The detection of a pulsar or some other transient in LoFASM data is imminent. Through the successful detection of injected data, we have shown that the pipeline for taking raw LoFASM data and pushing it through the current standard pulsar searching procedures is sound. Furthermore, the successful demonstration of LoFASM working in interferometer mode using its single baseline to clearly detect emissions from Cygnus A and Cassiopeia A are a testament to the fact that the instrument is in working order. LoFASM stations III, IV, and V have been in full spectrometer mode non-stop since only recently. Even so, the backlog of data to be searched is growing in tandem with the team's understanding of how best to process it. By analyzing and reviewing data taken across various data runs from multiple stations, we have shown that the LoFASM analog and digital designs are the embodiment of a propitious and cost-effective blueprint for educational and scientific research at low frequencies.

With the framework laid out in this work brought to advantage, upcoming research efforts can begin to answer some of the open questions identified in this thesis, such as whether or not an exhaustive search for a pulsar or some other transient emission can be detected through interferometric analysis of LoFASM data. It also remains to be seen if the application of interferometric principles will benefit efforts to fully calibrate the LoFASM

system, using either an artificial transmitter or a celestial source. Bringing these questions, along with others presented here, to bear is left to future research endeavors working with the LoFASM instruments. Conclusion of this work marks the beginning of an exciting new chapter: the commencement of a full duty cycle scientific monitoring program for the Low Frequency All Sky Monitor network of radio telescopes.

APPENDIX A

ARX SCHEMATIC

The LoFASM analog receiver module (ARX) is comprised a combination of RF filters, amplifiers, attenuators, bias-Tees, and supporting components. The latest design revision consists for four identical RF channels that prepare the LoFASM analog signals for digitization and processing. The electrical schematic and parts list for the current design revision of the ARX, created and provided by Brent Cole, is included in this section. For further discussion regarding the ARX and its role within the LoFASM architecture, see Section 2.1.3.

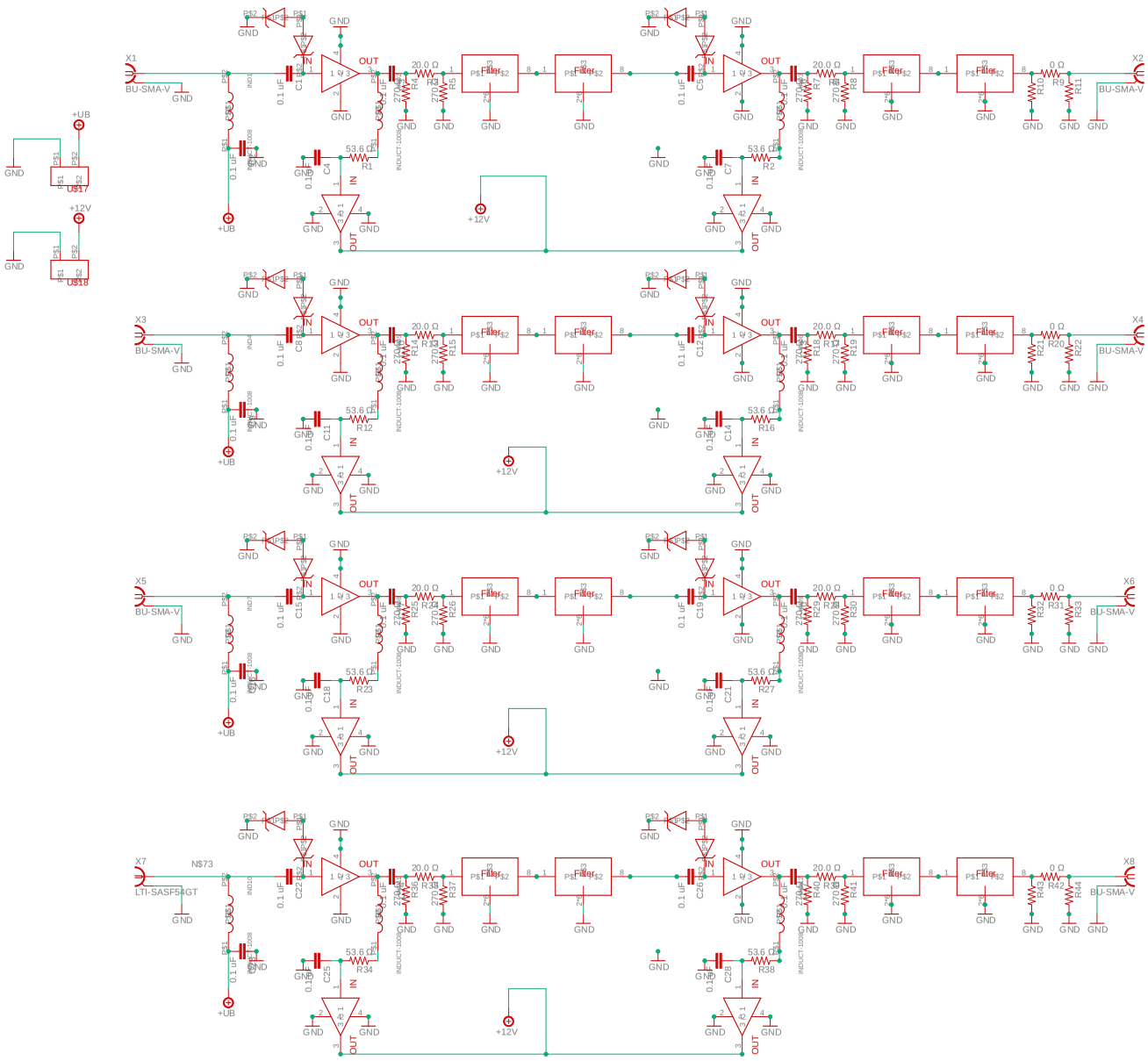

Figure A.1: A full schematic of the LoFASM ARX currently in use. The board consists of four parallel identical RF channels and serves as the last major component in the RF signal chain before leading to the digital backend system. Image Credit: Brent Cole

Description	Category	Package	Manufacturer	Manufacturer P/N	Supplier	Supplier P/N	Quantity	Comments
0 Ohm	Resistor	0805	Vishay	CRCW08050000Z0EA	Mouser	71-CRCW0805-0-E3	4	
20 Ohm	Resistor	0805	Vishay	CRCW080520R0FKEA	Mouser	71-CRCW0805-20-E3	8	
53.6 Ohm	Resistor	0805	Panasonic	ERJ-6ENF53R6V	Mouser	667-ERJ-6ENF53R6V	8	
270 Ohm	Resistor	0805	Vishay	CRCW0805270RFKEA	Mouser	71-CRCW0805-270-E3	16	
4.7 uH (F/E)	Inductor	4030	Coilcraft	XAL4030-472MEB	Mouser	994-XAL4030-472MEC	4	
4.7 uH	Inductor	0805	Coilcraft	0805PS-472KLB	Mouser	994-0805PS-472KLB	8	
0.1 uF	Capacitor	0603	Murata Electronics	GRM188R71C104KA01D	Mouser	81-GRM39X104K16	20	
GALI-74+	Amplifier	SOT-89	Mini-Circuits	GALI-74+	Mini-Circuits	GALI-74+	8	
9V Regulator	Voltage Regulator	SOT-89-3	Texas Instruments	UA78L09ACPKG3	Mouser	595-UA78L09ACPKG3	8	
75V Zener Diodes	Diode	SOD-123	Vishay	BZT52C75-V-GS08	Mouser	625-BZT52C75-V	16	Obsolete
SCLF-65+	Filter, Low Pass	YY161	Mini-Circuits	SCLF-65+	Mini-Circuits	SCLF-65+	8	
SCHF-17+	Filter, High Pass	YY161	Mini-Circuits	SCHF-17+	Mini-Circuits	SCHF-17+	8	
SMA Jack (Ext.)	Connector	N/A	Amphenol RF	132291	Mouser	523-132291	8	
Enclosure	Enclosure	N/A	McMaster-Carr	7593K28	McMaster-Carr	7593K28	1	
BNC Connector	Connector	N/A	Amphenol RF	031-10-RFX	Mouser	523-31-10-RFX	2	
Board	Board	N/A	Osh Park	N/A	Osh Park	N/A	1	
Fan	Fan	N/A	CUI	CFM-4020V-180-275	Mouser	490-CFM-4020V-180275	1	
0.1 uF (Front-End)	Capacitor	0603	Murata Electronics	GRJ188R71H104KE11D	Mouser	81-GRJ188R71H104KE1D	8	

Figure A.2: The list of components used in the current ARX design revision. These components are surface mount packages that are installed as per the ARX schematic provided in Figure A.2. Provided by: Brent Cole

APPENDIX B

LOFASM SYSTEM PARAMETERS

LoFASM system operating parameters are listed here for ease of reference. With the exception of the physical antenna locations, it is expected that some of the information in this section may soon be rendered out of date by new developments at the individual LoFASM sites. All of the information in this section will be kept updated at https://github.com/ldartez/lofasm/wiki.

B.1 Notation Conventions

The notation listed in the following table for the various LoFASM data channels is used heavily when working with LoFASM systems. This naming convention is used by low level recording routines at each station to identify the channels being recorded at any given time.

Channel ID	Array Channel & Polarization
INS	Inner Ring North-South
IEW	Inner Ring East-West
ONS	Outer Ring North-South
OEW	Outer Ring East-West
ORNS	Outrigger North-South
OREW	Outrigger East-West
AxB	A & B cross power

Table B.1: Polarization naming notation conventions used for convenience. In short, the suffix "NS" or "EW" is used to denote the polarization being used. The prefix indicates the array component. "I" for signals from the inner ring, "O" for the outer ring, and "OR" for the outrigger. Additionally, all of the cross power pairs use the same notation. To indicate a cross power channel, the letter "x" is placed in between the two parent channel IDs. For example, the cross power channel between INS and ONS is denoted by INSxONS.

Parameter Name	Parameter Value
Frequency Range	0-100 MHz
Frequency Step	97.6 kHz
No. Frequency Points	1024
Sample Time	0.83 s

Table B.2: LoFASM Spectrometer parameters. All data taken as part of this work was recorded using the LoFASM spectrometer using the above characteristics. The sample time is sometimes also called the integration time.

B.2 Spectrometer Parameters

B.3 Array and Outrigger Antenna Locations

Station	Array Lat.	Array Lon.	Bearing	Status
LoFASM I	26°33'19.57"N	-97°26'31.14"E	-15.28°	Active
LoFASM II	34°14'47.83"N	-107°38'24.27"E	14.66°	Inactive
LoFASM III	38°25'44.56"N	-79°50'46.45"E	-18.43°	Active
LoFASM IV	35°14'50.01"N	-116°47'35.77"E	-9.45°	Active
LoFASM V	41°56'15.56"N	-84°36'50.33"E	-15°	Active

Table B.3: Locations of each of the LoFASM stations and their current status. The bearing for each station is measured as depicted in Figure B.1.

Station	Outrigger Lat.	Outrigger Lon.	Baseline	Heading
LoFASM I	26°33'21.69"N	97°26'25.76"W	162.83 m	66.04°
LoFASM III	38°25'48.50"N	-79°50'32.83"E	351.6 m	69.73°
LoFASM IV	35°14'51.42"N	-116°47'27.90"E	203 m	77.4°
LoFASM V	41°56'15.20"N	-84°36'57.12"E	156.4 m	85.86°

Table B.4: Locations of each station's outrigger antenna and accompanying baseline information. Omitted here is LoFASM II there is no outrigger antenna installed at that site. Also omitted is the short baseline outrigger located at LoFASM III.

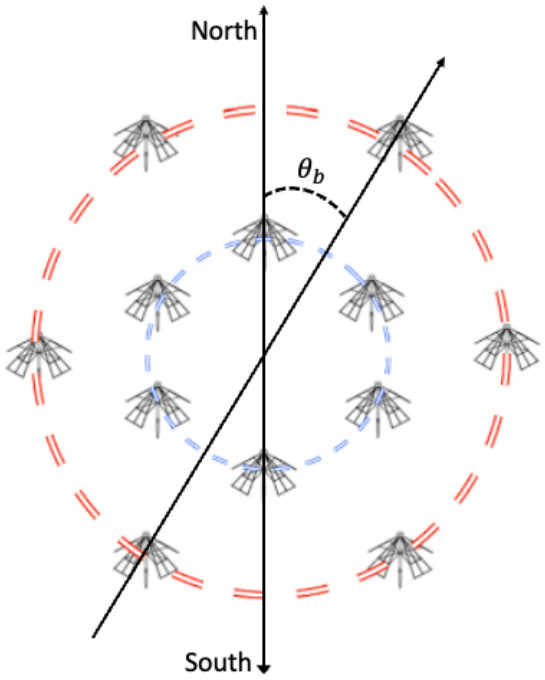

Figure B.1: LoFASM antenna placement. The angle θ_b denotes the array bearing off of North. Due to the hexagonal antenna configuration in each ring, the LoFASM array design has a 30° symmetry.

B.4 Antenna Spacing

LoFASM Ring	Radius (cm)	Definition
Inner Ring	441	R_{inner}
Outer Ring	763.83	$\sqrt{3}R_{inner}$

Table B.5: Antenna spacing in LoFASM array configuration. The radii of the two rings are chosen such that the attenuation of RF signals originating from the horizon (horizon rejection) is maximized at 20 MHz.

B.5 Overview of Observing Modes

The LoFASM channel mapping is site-specific. Furthermore, the status of each site's channel mapping is fluid and subject to change due to the types of observations being conducted or repairs and site reconfigurations that may take place. The channel mappings for LoFASM

I, III, & IV at the time of this writing are provided here for quick reference. However, the most up-to-date information will be found at https://github.com/ldartez/lofasm/wiki.

B.5.1 LoFASM I

Polarization	Trunk Line	Channel ID	ARX Channel	Current (A)
INS	3	D	1	1.21
ONS	1	B	2	1.46
ORNS	-	C	3	0.23

Table B.6: Cable mapping as of October 1, 2019 at LoFASM I. The trunk line column denotes the cable labeling inside the control room in Port Mansfield, the Channel ID is the resulting channel code assigned to the data products once they've been pre-processed by the digital backend, the ARX Channel is the denotes the input that was used on the four-channel ARX module, and the current draw for each channel is logged for long term health monitoring purposes. One channel was left open due to pending repairs on site.

B.5.2 LoFASM III

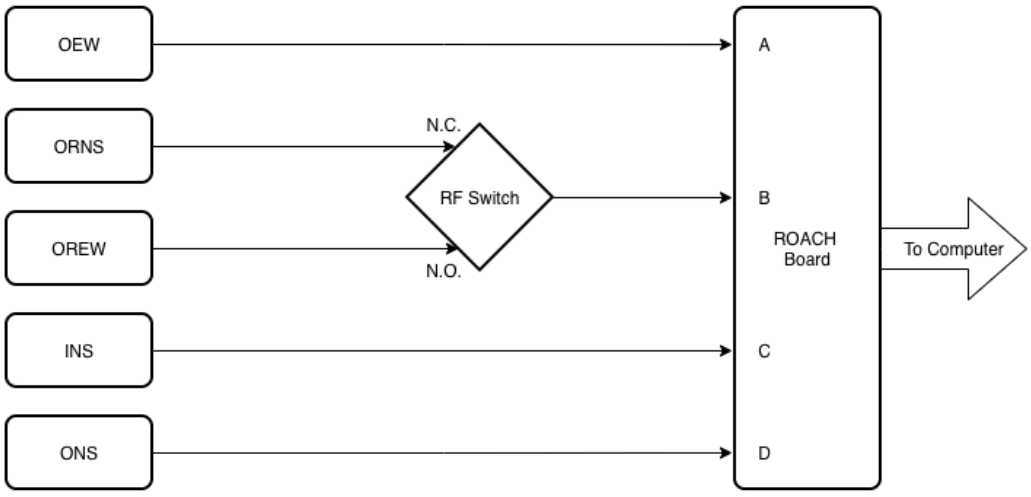

Figure B.2: High level flowchart of the channel mapping at the LoFASM III.

N.C. Port	N.O. Port
ORNS	OREW

Table B.7: The RF switch configuration at LoFASM III. The output of the RF switch will either be ORNS or OREW, depending on which port is activated.

Channel Identifier	Channel Input
A	OEW
B	ORNS
C	INS
D	ONS

Table B.8: LoFASM III Observation Mode 1: N.C. Port Activated

Toggling Observation Modes

Toggling the RF switch at LoFASM III to change observation modes is very painless. All that needs to be done is to run the *rf_toggle.py* script:

`/home/controller/bin/rf_toggle.py 1`.

As mentioned in earlier, there are two RF switches installed at LoFASM III, but only *RF switch 1* is connected to the RF system. Switch 0 is connected to the control computer but is not connected to any RF signal cables. The argument `1` above tells the script to toggle the state of RF switch 1. The status of both RF switches can be queried by executing the same command without any arguments.

B.5.3 LoFASM IV

Channel Identifier	Channel Input
A	OEW
B	OREW
C	INS
D	ONS

Table B.9: LoFASM III Observation Mode 2: N.O. Port Activated

Knob Configuration	Observation Mode
A1,B1	Full LoFASM Array
A2,B2	Full Outrigger Mode
A2,B1	Outrigger N-S
A1,B2	Outrigger E-W

Table B.10: RF Switch configurations at LoFASM IV. Each row corresponds to a unique observing mode that LoFASM IV is capable of. The knob configuration column lists the setting of each of the two knobs on the analog switch module. Each knob, A & B, has two settings: 1 & 2. This provides LoFASM IV with the four possible signal combinations listed here.

Data Channel	Polarization
A	INS
B	IEW
C	ONS / OREW
D	OEW / ORNS

Table B.11: Channel mapping for each of the four ROACH board inputs at LoFASM IV.

APPENDIX C

PROCEDURES FOR RECORDING DATA

This section describes the sequence for starting the LoFASM spectrometer and storing data to disk.

C.1 ROACH Board Boot Up

The LoFASM Control Computer (LCC) houses the ROACH board's operating system (OS). During boot up, the LCC prepares itself to "serve" a ROACH board OS image over the network to the ROACH board when requested. This was initially configured according to CASPER's wiki instructions: https://casper.ssl.berkeley.edu/wiki/ROACH_NFS_guide. Normally, the operator should not need to do anything manually to ensure that the ROACH board boots up properly. However, every so often an issue will inexorably pop up and prevent the ROACH board from booting. This is usually due to the network file system (NFS) daemon failing during startup. In such cases, simply rebooting the LCC tends to fix the issue.

There are two ways to ascertain the status of the ROACH board. The first is quick but unhelpful if troubleshooting is required. The second is more cumbersome, but provides much more useful information that allows for lower-level debugging of the ROACH system.

C.1.1 Quick Ping

The fastest way to determine if the ROACH board has booted up properly is simply to ping the device using internet control message protocol (ICMP) packets. If the ROACH board successfully responds to the ICMP pings then the ROACH board is working nominally. The presence of a network response indicates that the ROACH board successfully received and booted the Linux kernel it was served by the control computer. The default IP address

configured on the LoFASM ROACH boards is `192.168.4.21`. If this is the first time a system is being used or network configuration changes have occurred, it is a good idea to confirm that the ROACH IP address matches that of the `roach_ip` field in the LCC's LoFASM configuration file, which is usually located at `/home/controller/.lofasm/lofasm.cfg`.

C.1.2 Monitoring the Serial Port

The second method often used to monitor the ROACH board for debugging purposes is that of using a low-level serial port to monitor the ROACH board's serial output for signs of potential issues. The ROACH board's serial connection is usually mapped to `/dev/ttyS0` (or `/dev/ttyUSB0` if the serial port is connected via a USB FTDI adapter). To connect to the serial port a program called *minicom*, which is installed on all the LoFASM machines, can be used:

`sudo minicom -D /dev/ttyS0`.

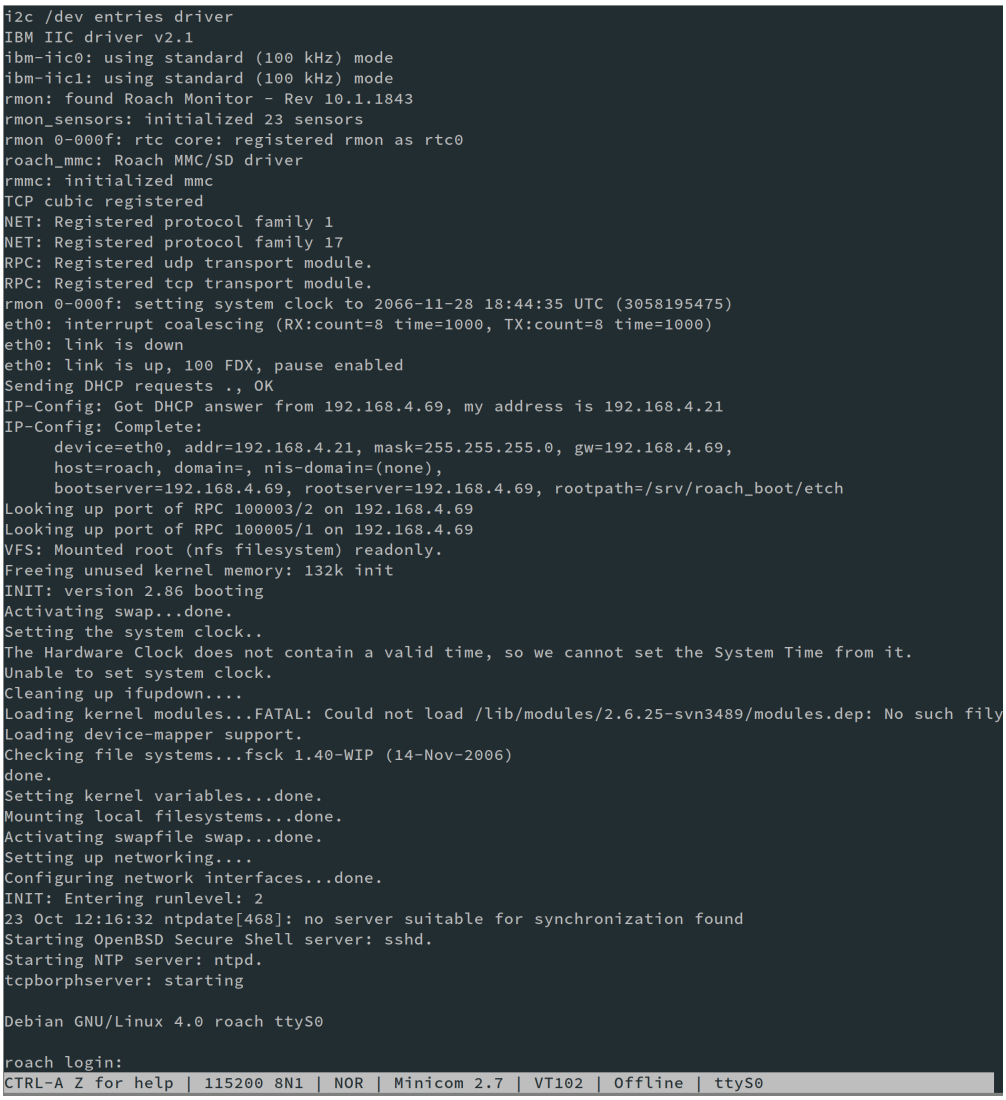

Figure C.1: *Minicom* showing a successful ROACH boot sequence.

C.1.3 Using the ROACH Monitor Script

The ROACH Monitor is a very useful and modified version of a script originally developed by Jason Manley as part of the CASPER collaboration. The script allows for the remote power control of a ROACH board, by communicating with the ROACH board's Actel chip. Using this script, the operator can easily control the power state of the ROACH board, reboot, as well as fetch useful diagnostic information from the ROACH board. This is great for many reasons, not the least of which is the fact that the ROACH board can be reset if it

ever freezes or becomes unresponsive. Unfortunately, the ethernet ports used to provide this functionality are known to be unstable on ROACH-1 boards. In fact, the board at LoFASM 1 often fails in this regard and tends to require a physical push of a button to be reset when it has fallen into a failure mode.

The ROACH Monitor can be called by simply issuing the command `roach_monitor` while using the `lofasm` Python virtual environment. On some LoFASM machines, such as LoFASM IV, the full path must instead be used: `/home/controller/bin/roach_monitor`. Figure C.2 shows the output that an operator can expect to see if the program is working correctly.

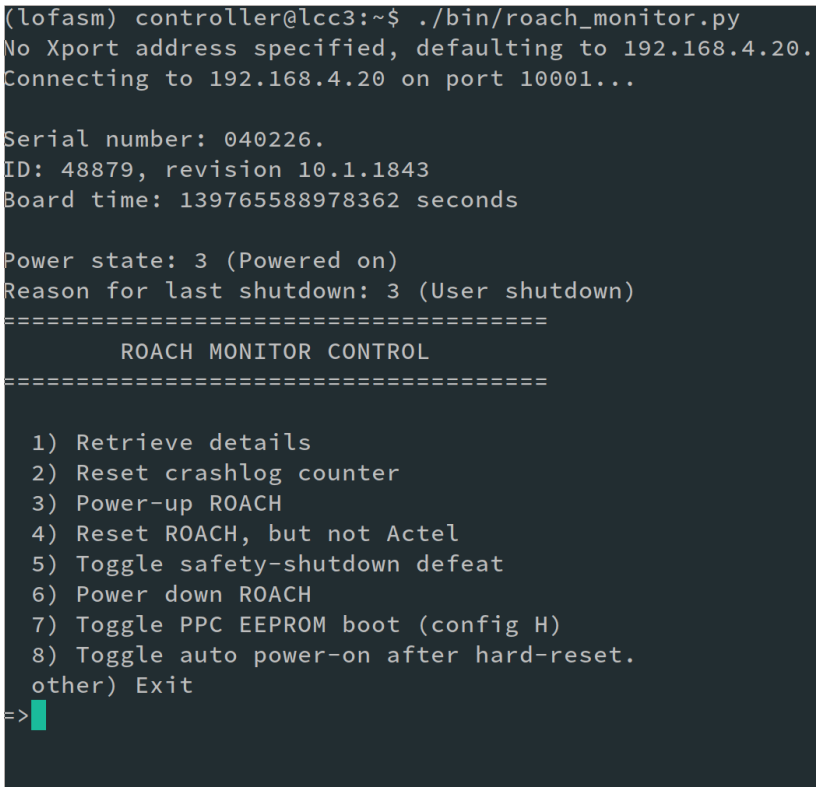

Figure C.2: Output of the ROACH monitor script that can be used to remotely control the power state of the LoFASM ROACH boards. Note that since this script communicates with the ROACH board using a dedicated physical connection, the apparent IP address shown is different than what should be used for ICMP pings and general SSH connections.

C.1.4 Initializing the LoFASM Spectrometer

Starting the LoFASM spectrometer entails simply running a single initialization script from within the `lofasm` Python virtual environment. The virtual environment can be activated with `workon lofasm`. With the virtual environment activated, the spectrometer firmware can be initialized with `/home/controller/bin/init_roach.sh`. Figure C.3 shows the expected output of the spectrometer initialization script in the case that everything is working properly.

```
controller@lcc3:~/bin$ ./init_roach.sh
Connecting to server 192.168.4.21 on port 7147...  ok

------------------------
Programming FPGA: poco_14b_no10gsnap_2014_Jun_03_1705.bof... done
Configuring fft_shift... done
Configuring accumulation period... done
Resetting board, software triggering and resetting error counters... done
Setting gains of all channels on all inputs to 1... done
FPGA Registers:  ['tx_overflow', 'tx_dest_port', 'tx_dest_ip', 'tx_cnt', 'quant3_gain', 'quant3_addr
', 'quant2_gain', 'quant2_addr', 'quant1_gain', 'quant1_addr', 'quant0_gain', 'quant0_addr', 'gbe_re
set', 'gbe0_linkup', 'gbe0', 'fmt_diagnostic', 'fft_shift', 'dir_x1_dd_real', 'dir_x1_cd_real', 'dir
_x1_cd_imag', 'dir_x1_cc_real', 'dir_x1_bd_real', 'dir_x1_bd_imag', 'dir_x1_bc_real', 'dir_x1_bc_ima
g', 'dir_x1_bb_real', 'dir_x1_ad_real', 'dir_x1_ad_imag', 'dir_x1_ac_real', 'dir_x1_ac_imag', 'dir_x
1_ab_real', 'dir_x1_ab_imag', 'dir_x1_aa_real', 'dir_x0_dd_real', 'dir_x0_cd_real', 'dir_x0_cd_imag'
, 'dir_x0_cc_real', 'dir_x0_bd_real', 'dir_x0_bd_imag', 'dir_x0_bc_real', 'dir_x0_bc_imag', 'dir_x0_
bb_real', 'dir_x0_ad_real', 'dir_x0_ad_imag', 'dir_x0_ac_real', 'dir_x0_ac_imag', 'dir_x0_ab_real',
'dir_x0_ab_imag', 'dir_x0_aa_real', 'ctrl', 'acc_num', 'acc_len', 'sys_clkcounter', 'sys_scratchpad'
, 'sys_rev_rcs', 'sys_rev', 'sys_board_id']
Configuring 10GbE Packet Transmitter...
Starting 10GbE core...
Cable verified connected to port 0.
core_name gbe0
mac_base: 2207613190144
fabric_ip: 3232236577
mac_base+fabric_ip: 2210845426721
fabric_port: 60000
ok, all set up. Try plotting using poco_plot_autos.py or poco_plot_cross.py
controller@lcc3:~/bin$
```

Figure C.3: Output of the `init_roach.sh` script.

This script will flash the FPGA chip on the ROACH board with the spectrometer's firmware and initialize it so that data begins streaming data packets to the LCC via a network cable. It is typically a good idea to confirm that the LCC is actually properly receiving the data packets that the ROACH board is pumping out. This can be done by using a network traffic monitoring tool such as *iftop* and pointing it to the local network device that the ROACH board is sending packets to. The specific network device can vary from one LoFASM station to another, so it is best to first identify the device name by checking the LoFASM configuration file (see Figure C.4). Once the device name is known

then a tool such as *iftop* can be used to monitor the incoming network traffic to confirm that data packets are being received by the LCC network cards. In the case shown in Figure C.4, the device name is `eth5`. Figure C.5 shows that data is being received at IP address `192.168.4.5` at a reported rate of 12.8 Megabits per second, indicating that the LoFASM spectrometer is running nominally.

```
controller@lcc3:~$ cat .lofasm/lofasm.cfg
[lofasmrec]
pidfile = /var/run/lofasm.pid
dataroot = /data1/test/
blocktime = 300
station_id = 3
roach_ip = 192.168.4.21
roach_ip_10gbe = 192.168.4.10
roach_port = 7147
roach_port_10gbe = 10000
incoming_ip_10gbe = 192.168.4.5
incoming_port_10gbe = 60001
tsamp = 0.083
samp_len = 139264
hdr_on = 1
hdr_version = 5
rec_mode = 2
blocksize = 81920
trunkA = IEW
trunkB = INS
trunkC = OREW
trunkD = OEW
dev = eth5
proto = raw
controller@lcc3:~$
```

Figure C.4: The LoFASM configuration file for LoFASM III. This file is used by all LCCs and includes important spectrometer configuration parameters.

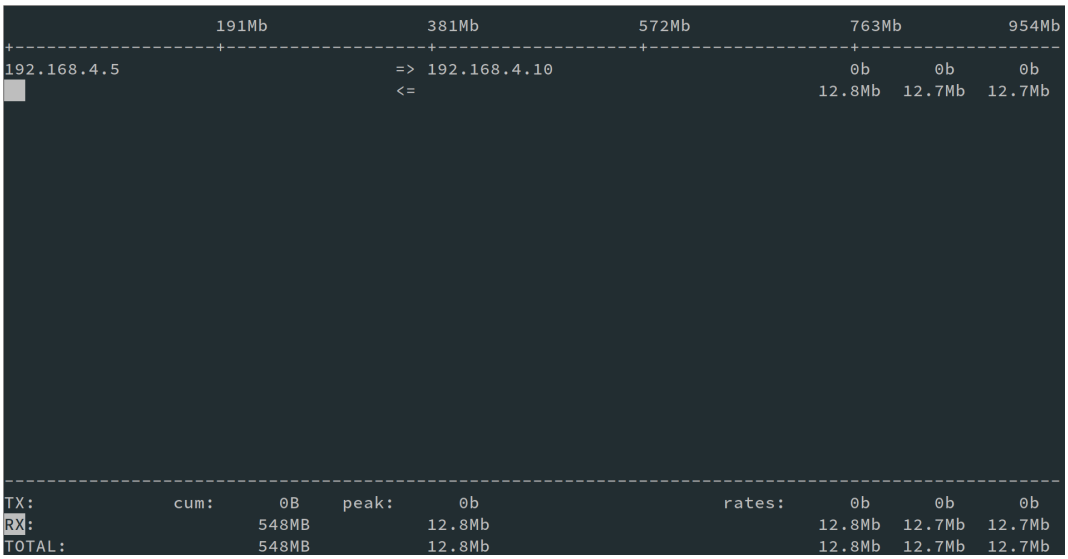

Figure C.5: Output of the `init_roach.sh` script.

C.2 Starting the LoFASM Data Recorder

Once the LoFASM Spectrometer is up and running, all that is left to do is to begin recording data and writing it to disk. It is a good idea to make sure that data is recorded onto a disk that has plenty of free space. A tool such as *df* can be used to check space availability on the LCCs. The `dataroot` field should be changed to the root path pointing to where new data should be stored. The LoFASM Data Recorder can by started by navigating to the *lofasmrec* repository and executing the recording program with elevated privileges:

```
sudo /home/controller/repos/lofasmrec/build/src/lofasmrec 864000
```
.

The `lofasmrec` program typically takes a single argument representing the total number of seconds for which to continuously take data. The data is split up into five-minute segments unless the `blocktime` parameter is changed in the LoFASM configuration file. A description of each of the configuration parameters used by the LoFASM systems is given in Table C.1. Additional details regarding the various parameters to `lofasmrec` and how it is implemented can be found at https://github.com/ldartez/lofasmrec.

Configuration Parameter	Description
pidfile	Path to file to use for storing daemon process id.
dataroot	Path to root directory where new data stored.
blocktime	Length of each data file in seconds. / OREW
station_id	LoFASM Station identifier.
roach_ip	ROACH board IP address. Used for firmware initialization.
roach_ip_10gbe	IP address used by the 10 gigabit ethernet port.
roach_port	KATCP port for firmware initialization and debugging.
roach_port_10gbe	Outgoing 10 gigabit ethernet port.
incoming_ip_10gbe	Local address to listen to for incoming data.
incoming_port_10gbe	Local port to listen on for incoming data.
tsamp	Spectrometer sampling time.
samp_len	Number of bytes in each time sample.
hdr_on	Flag to toggle the storage of header information.
hdr_version	Header version to use when recording data.
rec_mode	Recording mode. 1 for baseband, 2 for spectrometer mode.
blocksize	Maximum size of each file in bytes.
trunkA	Channel ID for ADC input A.
trunkB	Channel ID for ADC input B.
trunkC	Channel ID for ADC input C.
trunkD	Channel ID for ADC input D.
dev	Local device name to listen on for incoming data.
proto	Socket layer protocol to use for receiving data.

Table C.1: Short description of the LoFASM configuration parameters.

GLOSSARY

ADC Analog to Digital Converter.

ARX Analog Receiver.

BH Black Hole.

CASPER The Collaboration for Astronomy Signal Processing and Electronics Research.

FFT Fast Fourier Transform.

FPGA Field Programmable Gate Array.

FRB Fast Radio Burst.

FTDI Future Technology Devices International Chip.

GPU Graphics Processing Unit.

ICMP Internet Control Message Protocol.

IEW Inner Ring East-West Polarization.

IEWxOEW Cross-Power between the IEW and OEW polarizations.

IEWxOREW Cross-Power between the IEW and OREW polarizations.

INS Inner Ring North-South Polarization.

INSxONS Cross-Power between the INS and ONS polarizations.

INSxORNS Cross-Power between the INS and ORNS polarizations.

IP Internet Protocol.

LCC LoFASM Control Computer.

LoFASM The Low Frequency All Sky Monitor.

LST Local Sidereal Time.

N.C. Normally Closed.

N.O. Normally Open.

NFS Network File System.

NS Neutron Star.

OEW Outer Ring East-West Polarization.

OEWxOREW Cross-Power between the OEW and OREW polarizations.

ONS Outer Ring North-South Polarization.

OREW Outrigger East-West Polarization.

ORNS Outrigger North-South Polarization.

PCB Printed Circuit Board.

PFB Polyphase Filterbank.

RF Radio Frequency.

ROACH Reconfigurable Open Architecture Computing Hardware.

SSH Secure SHell.

USB Universal Serial Bus.

UTRGV University of Texas at Rio Grande Valley.

REFERENCES

AbsoluteCosmos. Five-hundred-meter aperture spherical radio telescope (fast telescope). https://www.youtube.com/watch?v=YnCTsOXO_ZY, 2020.

M. Amiri, K. Bandura, P. Berger, M. Bhardwaj, M. M. Boyce, P. J. Boyle, C. Brar, M. Burhanpurkar, P. Chawla, and et al. The chime fast radio burst project: System overview. *The Astrophysical Journal*, 863(1):48, Aug 2018. ISSN 1538-4357. doi: 10.3847/1538-4357/aad188. URL http://dx.doi.org/10.3847/1538-4357/aad188.

P. Andrews, C. Ramette, S. Niedbalski, N. Birzer, T. Dolch, T. Creighton, L. Dartez, B. Cole, A. Dulemba, and C.J. Rose. Mitigation of radio frequency interference and beam location for low frequency all sky monitor telescope, 2019. Poster Presentation at Hillsdale College Laureates Research Symposium.

Kevin Bandura, Graeme E. Addison, Mandana Amiri, J. Richard Bond, Duncan Campbell-Wilson, Liam Connor, Jean-François Cliche, Greg Davis, Meiling Deng, Nolan Denman, and et al. Canadian hydrogen intensity mapping experiment (chime) pathfinder. *Ground-based and Airborne Telescopes V*, Jul 2014. doi: 10.1117/12.2054950. URL http://dx.doi.org/10.1117/12.2054950.

Maxim V Barkov, Maxim Lyutikov, and Dmitry Khangulyan. Fast-moving pulsars as probes of interstellar medium. *Monthly Notices of the Royal Astronomical Society*, 497(3):2605–2615, Jun 2020. ISSN 1365-2966. doi: 10.1093/mnras/staa1601. URL http://dx.doi.org/10.1093/mnras/staa1601.

S. D. Bates, D. R. Lorimer, and J. P. W. Verbiest. The pulsar spectral index distribution. *Monthly Notices of the Royal Astronomical Society*, 431(2):1352–1358, 03 2013. ISSN 0035-8711. doi: 10.1093/mnras/stt257. URL https://doi.org/10.1093/mnras/stt257.

Florian Briechle. In-situ absolute calibration of electric-field amplitude measurements with the lpda radio detector stations of the pierre auger observatory. *EPJ Web of Conferences*, 135:01014, 2017. ISSN 2100-014X. doi: 10.1051/epjconf/201713501014. URL http://dx.doi.org/10.1051/epjconf/201713501014.

B. F. Burke and K. L. Franklin. Observations of a variable radio source associated with the planet jupiter. *Journal of Geophysical Research (1896-1977)*, 60(2):213–217, 1955. doi: https://doi.org/10.1029/JZ060i002p00213. URL https://agupubs.onlinelibrary.wiley.com/doi/abs/10.1029/JZ060i002p00213.

C. L. Carilli, J. N. Hewitt, and A. Loeb. Low frequency radio astronomy from the moon: cosmic reionization and more. *arXiv e-prints*, art. astro-ph/0702070, February 2007.

Baptiste Cecconi. Polarization in low frequency radio astronomy, 2019.

Chihway Chang, Christian Monstein, Alexandre Refregier, Adam Amara, Adrian Glauser, and Sarah Casura. Beam calibration of radio telescopes with drones. *Publications of the Astronomical Society of the Pacific*, 127(957):1131–1143, Nov 2015. ISSN 1538-3873. doi: 10.1086/683467. URL http://dx.doi.org/10.1086/683467.

T. E. Clarke, C. A. Higgins, Jinhie Skarda, Kazumasa Imai, Masafumi Imai, Francisco Reyes, Jim Thieman, Ted Jaeger, Henrique Schmitt, Nagini Paravastu Dalal, Jayce Dowell, S. W. Ellingson, Brian Hicks, Frank Schinzel, and G. B. Taylor. Probing jovian decametric emission with the long wavelength array station 1. *Journal of Geophysical Research: Space Physics*, 119(12):9508–9526, 2014. doi: https://doi.org/10.1002/2014JA020289. URL https://agupubs.onlinelibrary.wiley.com/doi/abs/10.1002/2014JA020289.

B. Cole. Lofasm updates - a white noise generator for calibration purposes, 2019. Seminar talk presented at a weekly meeting for the Center for Advanced Radio Astronomy at the University of Texas Rio Grande Valley.

T. W. Cole and J. D. H. Pilkington. Search for Pulsating Radio Sources in the Declination Range + 44° ¡ δ ¡ + 90°. *Nature*, 219(5154):574–576, August 1968. doi: 10.1038/219574a0.

James J. Condon and Scott M. Ransom. *Essential Radio Astronomy*. 2016.

James M. Cordes. Pulsar Observations I. – Propagation Effects, Searching Distance Estimates, Scintillations and VLBI. In Snezana Stanimirovic, Daniel Altschuler, Paul Goldsmith, and Chris Salter, editors, *Single-Dish Radio Astronomy: Techniques and Applications*, volume 278 of *Astronomical Society of the Pacific Conference Series*, pages 227–250, December 2002.

Thibault Damour. 1974: the discovery of the first binary pulsar. *Classical and Quantum Gravity*, 32(12):124009, Jun 2015. ISSN 1361-6382. doi: 10.1088/0264-9381/32/12/124009. URL http://dx.doi.org/10.1088/0264-9381/32/12/124009.

L.P. Dartez. A digital backend for the low frequency all sky monitor. Master's thesis, University of Texas at Brownsville, Brownsville, Texas, May 2014.

F. de Gasperin, M. Mevius, D. A. Rafferty, H. T. Intema, and R. A. Fallows. The effect of the ionosphere on ultra-low-frequency radio-interferometric observations. *aap*, 615:A179, August 2018. doi: 10.1051/0004-6361/201833012.

A. T. Deller, W. M. Goss, W. F. Brisken, S. Chatterjee, J. M. Cordes, G. H. Janssen, Y. Y. Kovalev, T. J. W. Lazio, L. Petrov, B. W. Stappers, and A. Lyne. Microarcsecond VLBI Pulsar Astrometry with PSRπ II. Parallax Distances for 57 Pulsars. *ApJ*, 875(2):100, April 2019. doi: 10.3847/1538-4357/ab11c7.

Nolan Denman, Mandana Amiri, Kevin Bandura, Liam Connor, Matt Dobbs, Mateus Fandino, Mark Halpern, Adam Hincks, Gary Hinshaw, Carolin Hofer, and et al. A gpu-based correlator x-engine implemented on the chime pathfinder. *2015 IEEE 26th International Conference on Application-specific Systems, Architectures and Processors (ASAP)*,

Jul 2015. doi: 10.1109/asap.2015.7245702. URL http://dx.doi.org/10.1109/ASAP.2015.7245702.

T. Dolch, P. Andrews, B. Cole, T. Creighton, L.P. Dartez, Alexander Dulemba, F.A. Jenet, S. Niedbalski, C. Ramette, and S. Smith. First light for station v of the low frequency all-sky monitor radio telescope. In *Proceedings of IEEE International Symposium on Antennas and Propagation and North American Radio Science Meetings*, Radio Transients Instruments, 2020. URL https://www.usnc-ursi-archive.org/aps-ursi/2020/pdfs/0000171.pdf.

J. Dowell. Parametric model for the lwa-1 dipole response as a function of frequency, 2011. Long Wavelength Array Memo (178).

Michael W. Eastwood, Marin M. Anderson, Ryan M. Monroe, Gregg Hallinan, Benjamin R. Barsdell, Stephen A. Bourke, M. A. Clark, Steven W. Ellingson, Jayce Dowell, Hugh Garsden, and et al. The radio sky at meter wavelengths: m-mode analysis imaging with the ovro-lwa. *The Astronomical Journal*, 156(1):32, Jun 2018. ISSN 1538-3881. doi: 10.3847/1538-3881/aac721. URL http://dx.doi.org/10.3847/1538-3881/aac721.

S. Ellingson. A parametric model for the normalized power pattern of a dipole antenna over ground, 2010. Long Wavelength Array Memo (175).

Yan Fa-bao, Y. Liu, K. Xu, Shang Ziqian, Su Yanrui, G. Lu, Y. Chen, and Z. Wu. A broadband digital receiving system with large dynamic range for solar radio observation. *Research in Astronomy and Astrophysics*, 20:156, 2020.

E. Fonseca, B. C. Andersen, M. Bhardwaj, P. Chawla, D. C. Good, A. Josephy, V. M. Kaspi, K. W. Masui, R. Mckinven, D. Michilli, Z. Pleunis, K. Shin, S. P. Tendulkar, K. M. Bandura, P. J. Boyle, C. Brar, T. Cassanelli, D. Cubranic, M. Dobbs, F. Q. Dong, B. M. Gaensler, G. Hinshaw, T. L. Landecker, C. Leung, D. Z. Li, H.-H. Lin, J. Mena-Parra, M. Merryfield, A. Naidu, C. Ng, C. Patel, U. Pen, M. Rafiei-Ravandi, M. Rahman, S. M. Ransom, P. Scholz, K. M. Smith, I. H. Stairs, K. Vanderlinde, P. Yadav, and A. V. Zwaniga. Nine new repeating fast radio burst sources from CHIME/FRB. *The Astrophysical Journal*, 891(1):L6, feb 2020. doi: 10.3847/2041-8213/ab7208. URL https://doi.org/10.3847/2041-8213/ab7208.

H. T. Friis and C. B. Feldman. A multiple unit steerable antenna for short-wave reception. *The Bell System Technical Journal*, 16(3):337–419, 1937. doi: 10.1002/j.1538-7305.1937.tb00425.x.

M.A. Garrett. Radio astronomy transformed: Aperture arrays - past, present & future. In *Proceedings of the meeting 'From Antikythera to the Square Kilometre Array: Lessons from the Ancients'*, Antikythera & SKA, 2012. URL http://pos.sissa.it/cgi-bin/reader/conf.cgi?confid=170.

A. E. Guzmán, J. May, H. Alvarez, and K. Maeda. All-sky galactic radiation at 45 mhz and spectral index between 45 and 408 mhz. *Astronomy & Astrophysics*, 525:A138, Dec

2010. ISSN 1432-0746. doi: 10.1051/0004-6361/200913628. URL http://dx.doi.org/10.1051/0004-6361/200913628.

R. Hanbury Brown. Adam Hilger, 1991.

Alice K Harding and Dong Lai. Physics of strongly magnetized neutron stars. *Reports on Progress in Physics*, 69(9):2631–2708, Aug 2006. ISSN 1361-6633. doi: 10.1088/0034-4885/69/9/r03. URL http://dx.doi.org/10.1088/0034-4885/69/9/R03.

C. G. T. Haslam, U. Klein, C. J. Salter, H. Stoffel, W. E. Wilson, M. N. Cleary, D. J. Cooke, and P. Thomasson. A 408 MHz all-sky continuum survey. I - Observations at southern declinations and for the North Polar region. *aap*, 100:209–219, July 1981.

T. E. Hassall, B. W. Stappers, J. W. T. Hessels, M. Kramer, A. Alexov, K. Anderson, T. Coenen, A. Karastergiou, E. F. Keane, V. I. Kondratiev, K. Lazaridis, J. van Leeuwen, A. Noutsos, M. Serylak, C. Sobey, J. P. W. Verbiest, P. Weltevrede, K. Zagkouris, R. Fender, R. A. M. J. Wijers, L. Bähren, M. E. Bell, J. W. Broderick, S. Corbel, E. J. Daw, V. S. Dhillon, J. Eislöffel, H. Falcke, J. M. Grießmeier, P. Jonker, C. Law, S. Markoff, J. C. A. Miller-Jones, R. Osten, E. Rol, A. M. M. Scaife, B. Scheers, P. Schellart, H. Spreeuw, J. Swinbank, S. ter Veen, M. W. Wise, R. Wijnands, O. Wucknitz, P. Zarka, A. Asgekar, M. R. Bell, M. J. Bentum, G. Bernardi, P. Best, A. Bonafede, A. J. Boonstra, M. Brentjens, W. N. Brouw, M. Brüggen, H. R. Butcher, B. Ciardi, M. A. Garrett, M. Gerbers, A. W. Gunst, M. P. van Haarlem, G. Heald, M. Hoeft, H. Holties, A. de Jong, L. V. E. Koopmans, M. Kuniyoshi, G. Kuper, G. M. Loose, P. Maat, J. Masters, J. P. McKean, H. Meulman, M. Mevius, H. Munk, J. E. Noordam, E. Orrú, H. Paas, M. Pandey-Pommier, V. N. Pandey, R. Pizzo, A. Polatidis, W. Reich, H. Röttgering, J. Sluman, M. Steinmetz, C. G. M. Sterks, M. Tagger, Y. Tang, C. Tasse, R. Vermeulen, R. J. van Weeren, S. J. Wijnholds, and S. Yatawatta. Wide-band simultaneous observations of pulsars: disentangling dispersion measure and profile variations. *AAP*, 543:A66, July 2012. doi: 10.1051/0004-6361/201218970.

J. F. Helmboldt and N. E. Kassim. The evolution of cassiopeia a at low radio frequencies. *The Astronomical Journal*, 138(3):838–844, Jul 2009. ISSN 1538-3881. doi: 10.1088/0004-6256/138/3/838. URL http://dx.doi.org/10.1088/0004-6256/138/3/838.

A. Hewish, S.J. Bell, J. Pilkington, and et al. Observation of a rapidly pulsating radio source. *Nature*, (217):709–713, 1968.

Jack Hickish, Zuhra Abdurashidova, Zaki Ali, Kaushal D. Buch, Sandeep C. Chaudhari, Hong Chen, Matthew Dexter, Rachel Simone Domagalski, John Ford, Griffin Foster, David George, Joe Greenberg, Lincoln Greenhill, Adam Isaacson, Homin Jiang, Glenn Jones, Francois Kapp, Henno Kriel, Rich Lacasse, Andrew Lutomirski, David MacMahon, Jason Manley, Andrew Martens, Randy McCullough, Mekhala V. Muley, Wesley New, Aaron Parsons, Daniel C. Price, Rurik A. Primiani, Jason Ray, Andrew Siemion, Verees'e Van Tonder, Laura Vertatschitsch, Mark Wagner, Jonathan Weintroub, and Dan

Werthimer. A decade of developing radio-astronomy instrumentation using casper open-source technology, 2016.

Brian C. Hicks, Nagini Paravastu-Dalal, Kenneth P. Stewart, William C. Erickson, Paul S. Ray, Namir E. Kassim, Steve Burns, Tracy Clarke, Henrique Schmitt, Joe Craig, Jake Hartman, and Kurt W. Weiler. A wide-band, active antenna system for long wavelength radio astronomy. *Publications of the Astronomical Society of the Pacific*, 124(920):1090–1104, oct 2012. doi: 10.1086/668121. URL https://doi.org/10.1086/668121.

J. A. Högbom. Aperture Synthesis with a Non-Regular Distribution of Interferometer Baselines. *aaps*, 15:417, June 1974.

R. A. Hulse and J. H. Taylor. Discovery of a pulsar in a binary system. *apjl*, 195:L51–L53, January 1975. doi: 10.1086/181708.

Russell A. Hulse. The discovery of the binary pulsar. *Rev. Mod. Phys.*, 66:699–710, Jul 1994. doi: 10.1103/RevModPhys.66.699. URL https://link.aps.org/doi/10.1103/RevModPhys.66.699.

K.G. Jansky. Electrical disturbances apparently of extraterrestrial origin. *Proceedings of the Institute of Radio Engineers*, 21(10):1387–1398, 1933. doi: 10.1109/JRPROC.1933.227458.

Fredrick Jenet, S. Cohen, L. P. Dartez, A. Ford, A. Garcia, J. Hinojosa, C. Longoria, G. Lunsford, A. Mata, R. B. Miller, J. Reser, J. Rivera, K. Stovall, T. D. Creighton, B. Hicks, R. H. Price, and G. B. Taylor. The Design of the Low Frequency All Sky Monitor (LoFASM) for the Study of Radio Transients and Student Training. In *American Astronomical Society Meeting Abstracts #221*, volume 221 of *American Astronomical Society Meeting Abstracts*, page 328.06, January 2013.

G. Jones. Instrumentation for wide bandwidth radio astronomy. 2010.

Victoria M. Kaspi and Michael Kramer. Radio pulsars: The neutron star population & fundamental physics, 2016.

Kenneth I. Kellermann, Ellen N. Bouton, and Sierra S. Brandt. *A New Window on the Universe*, pages 1–34. Springer International Publishing, Cham, 2020. ISBN 978-3-030-32345-5. doi: 10.1007/978-3-030-32345-5_1. URL https://doi.org/10.1007/978-3-030-32345-5_1.

James Kent, Jayce Dowell, Adam Beardsley, Nithyanandan Thyagarajan, Greg Taylor, and Judd Bowman. A real-time, all-sky, high time resolution, direct imager for the long wavelength array. *Monthly Notices of the Royal Astronomical Society*, 486(4):5052–5060, May 2019. ISSN 1365-2966. doi: 10.1093/mnras/stz1206. URL http://dx.doi.org/10.1093/mnras/stz1206.

Artem Koval, Yao Chen, Aleksander Stanislavsky, Anton Kashcheyev, and Qing-He Zhang. Simulation of focusing effect of traveling ionospheric disturbances on meter-decameter

solar dynamic spectra. *Journal of Geophysical Research: Space Physics*, 123(11):8940–8950, 2018. doi: https://doi.org/10.1029/2018JA025584. URL https://agupubs.onlinelibrary.wiley.com/doi/abs/10.1029/2018JA025584.

Artem Koval, Yao Chen, Takuya Tsugawa, Yuichi Otsuka, Atsuki Shinbori, Michi Nishioka, Anatoliy Brazhenko, Aleksander Stanislavsky, Aleksander Konovalenko, Qing-He Zhang, Christian Monstein, and Roman Gorgutsa. Direct observations of traveling ionospheric disturbances as focusers of solar radiation: Spectral caustics. *The Astrophysical Journal*, 877(2):98, may 2019. doi: 10.3847/1538-4357/ab1b52. URL https://doi.org/10.3847/1538-4357/ab1b52.

J.D. Kraus. Grote reber, founder of radio astronomy. *Journal of the Royal Astronomical Society of Canada*, 82(3):107–114, 1988.

J. M. Lattimer. The physics of neutron stars. *Science*, 304(5670):536–542, Apr 2004. ISSN 1095-9203. doi: 10.1126/science.1090720. URL http://dx.doi.org/10.1126/science.1090720.

Shyeh Tjing Loi, Tara Murphy, Martin E. Bell, David L. Kaplan, Emil Lenc, André R. Offringa, Natasha Hurley-Walker, G. Bernardi, J. D. Bowman, F. Briggs, and et al. Quantifying ionospheric effects on time-domain astrophysics with the murchison wide-field array. *Monthly Notices of the Royal Astronomical Society*, 453(3):2732–2747, Sep 2015. ISSN 1365-2966. doi: 10.1093/mnras/stv1808. URL http://dx.doi.org/10.1093/mnras/stv1808.

D. R. Lorimer and M. Kramer. *Handbook of Pulsar Astronomy*, volume 4. 2004.

D. R. Lorimer, M. Bailes, M. A. McLaughlin, D. J. Narkevic, and F. Crawford. A bright millisecond radio burst of extragalactic origin. *Science*, 318(5851):777–780, Nov 2007. ISSN 1095-9203. doi: 10.1126/science.1147532. URL http://dx.doi.org/10.1126/science.1147532.

D.R. Lorimer. Binary and millisecond pulsars at the new millennium. *Living Reviews in Relativity*, 2001.

Duncan R. Lorimer and Maura A. McLaughlin. Probing fundamental physics with pulsars. *Highlights of Astronomy*, 15:131–136, November 2010. doi: 10.1017/S1743921310008513.

R. N. Manchester, G. B. Hobbs, A. Teoh, and M. Hobbs. The australia telescope national facility pulsar catalogue. *The Astronomical Journal*, 129(4):1993–2006, Apr 2005. ISSN 1538-3881. doi: 10.1086/428488. URL http://dx.doi.org/10.1086/428488.

R. Miller. The low frequency all sky monitor for the study of radio transients: Array configuration and sensitivity, 2012. Undergraduate Thesis.

E.Y. Muhammet, M. Torlak, L. Dartez, T. Creighton, and F.A. Jenet. Sky imaging using lofasm: Signal processing, calibration, and rfi suppression. 2019.

J. Murray. Lofasm antenna pattern, 2017. In an Email to the LoFASM Team.

J.I. Murray. An analog receiver for the low frequency all sky monitor, 2015. Undergraduate Thesis.

S. Niedbalski, P. Andrews, N. Birzer, B. Cole, T. Creighton, L. Dartez, T. Dolch, A. Dulemba, C. Ramette, and C.J. Rose. The construction, testing, and implementation of coaxial cable at the low frequency all sky monitor, 2019. Poster Presentation at Hillsdale College Laureates Research Symposium.

K. S. Obenberger, E. Dao, and J.D. Dowell. Experimenting with frequency-and-angular sounding to characterize traveling ionospheric disturbances using the lwa-sv radio telescope and a dps4d. *Radio Science*, 54(2):181–193, 2019. doi: https://doi.org/10.1029/2018RS006690. URL `https://agupubs.onlinelibrary.wiley.com/doi/abs/10.1029/2018RS006690`.

Aaron R. Parsons, Donald C. Backer, Griffin S. Foster, Melvyn C. H. Wright, Richard F. Bradley, Nicole E. Gugliucci, Chaitali R. Parashare, Erin E. Benoit, James E. Aguirre, Daniel C. Jacobs, and et al. The precision array for probing the epoch of re-ionization: Eight station results. *The Astronomical Journal*, 139(4):1468–1480, Mar 2010. ISSN 1538-3881. doi: 10.1088/0004-6256/139/4/1468. URL `http://dx.doi.org/10.1088/0004-6256/139/4/1468`.

Danny C. Price. Spectrometers and polyphase filterbanks in radio astronomy, 2018.

C. Rammete, P. Andrews, N. Birzer, T. Creighton, B. Cole, L. Dartez, T. Dolch, A. Dulemba, S. Niedbalski, and C.J. Rose. Design and construction of the low-frequency all-sky monitor v, 2019. Poster Presentation at Hillsdale College Laureates Research Symposium.

Scott Ransom. PRESTO: PulsaR Exploration and Search TOolkit, July 2011.

P. L. Read. Measurements of the flux density of Cas A and confirmation of an anomaly at 38 MHz. *mnras*, 178:259–264, January 1977. doi: 10.1093/mnras/178.2.259.

G. Reber. *Cosmic Static*, volume 10, pages 61–69. Springer, Dordrecht, 1944. doi: 10.1007/978-94-009-7752-5_6. URL `https://doi.org/10.1007/978-94-009-7752-5_6`.

J. Rivera. Power distribution in the lofasm radio telescope array, 2012. Undergraduate Thesis.

L. G. Spitler, J. M. Cordes, J. W. T. Hessels, D. R. Lorimer, M. A. McLaughlin, S. Chatterjee, F. Crawford, J. S. Deneva, V. M. Kaspi, R. S. Wharton, and et al. Fast radio burst discovered in the arecibo pulsar alfa survey. *The Astrophysical Journal*, 790(2):101, Jul 2014. ISSN 1538-4357. doi: 10.1088/0004-637x/790/2/101. URL `http://dx.doi.org/10.1088/0004-637X/790/2/101`.

D. R. Stinebring, M. A. McLaughlin, J. M. Cordes, K. M. Becker, J. E. Espinoza Goodman, M. A. Kramer, J. L. Sheckard, and C. T. Smith. Faint scattering around pulsars: Probing the interstellar medium on solar system size scales. *The Astrophysical Journal*, 549(1): L97–L100, Mar 2001. ISSN 0004-637X. doi: 10.1086/319133. URL http://dx.doi.org/10.1086/319133.

K. Stovall, P. S. Ray, J. Blythe, J. Dowell, T. Eftekhari, A. Garcia, T. J. W. Lazio, M. McCrackan, F. K. Schinzel, and G. B. Taylor. PULSAR OBSERVATIONS USING THE FIRST STATION OF THE LONG WAVELENGTH ARRAY AND THE LWA PULSAR DATA ARCHIVE. *The Astrophysical Journal*, 808(2):156, jul 2015. doi: 10.1088/0004-637x/808/2/156. URL https://doi.org/10.1088/0004-637x/808/2/156.

G.B. Taylor, J. Dowell, Y. Pihlström, F. Schinzel, G. Hallinan, I.M. Hoffman, D. Besson, S. Prohira, A.M. Gretarsson, R.D. Fobes, T.J. Maccarone, T. Dolch, J.D. Bowman, D.C. Jacobs, F.A. Jenet, S. Kurtz, N. Thyagarajan, A.P. Beardsley, J.O. Burns, T. Bullett, M. Kavic, and P. Driessen. The swarm development concept for the lwa. *Bulletin of the American Astronomical Society*, 51(2):379–423, 2019.

Greg Taylor, Jayce Dowell, Joe Malins, Tracy Clarke, Namir Kassim, Simona Giacintucci, Brian Hicks, Jason Kooi, Wendy Peters, Emil Polisensky, Frank Schinzel, and Kevin Stovall. A next generation low band observatory: A community study exploring low frequency options for ngvla, 2017.

Joseph H. Taylor. Binary pulsars and relativistic gravity. *Rev. Mod. Phys.*, 66:711–719, 1994. doi: 10.1103/RevModPhys.66.711.

A. Richard Thompson, James M. Moran, and Jr. Swenson, George W. *Interferometry and Synthesis in Radio Astronomy, 3rd Edition*. 2017. doi: 10.1007/978-3-319-44431-4.

M. Torlak, E.Y. Muhammet, L. Dartez, T. Creighton, and F.A. Jenet. A low complexity rfi mitigation method for affordable interferometric radio telescopes. 2020.

Wikipedia contributors. Psr b1919+21 — Wikipedia, the free encyclopedia, 2021. URL https://en.wikipedia.org/w/index.php?title=PSR_B1919%2B21&oldid=1015300319. [Online; accessed 25-April-2021].

T.L. Wilson, K. Rohlfs, and S. Hüttemeister. *Fundamentals of Antenna Theory*, pages 121–142. Springer-Verlag Berlin Heidelberg, 2004.

Philippe Zarka. Plasma interactions of exoplanets with their parent star and associated radio emissions. *planss*, 55(5):598–617, April 2007. doi: 10.1016/j.pss.2006.05.045.

Saleem Zaroubi. The epoch of reionization. *Astrophysics and Space Science Library*, page 45–101, Sep 2012. ISSN 0067-0057. doi: 10.1007/978-3-642-32362-1_2. URL http://dx.doi.org/10.1007/978-3-642-32362-1_2.